Title
Endolysosomal inhibition induces the autophagy-dependent secretion of autophagosomal cargo

Author
Solvik, Tina Ann

Publication Date
2020

Peer reviewed|Thesis/dissertation

Endolysosomal inhibition induces the autophagy-dependent secretion of autophagosomal cargo

by
Tina Ann Solvik

DISSERTATION
Submitted in partial satisfaction of the requirements for degree of
DOCTOR OF PHILOSOPHY

in

Biomedical Sciences

in the

GRADUATE DIVISION
of the
UNIVERSITY OF CALIFORNIA, SAN FRANCISCO

Approved:

DocuSigned by:
Robert Blelloch
91DFF4C4A2FF4FC...

Robert Blelloch
Chair

DocuSigned by:
Jayanta Debnath
[illegible]

Jayanta Debnath

DocuSigned by:
Rushika Perera
[illegible]

Rushika Perera

DocuSigned by:
Aimee Kao
745CF57D40DB494...

Aimee Kao

Committee Members

ACKNOWLEDGEMENTS

Completion of this dissertation would not have been possible without the support I have received from my lab, colleagues at UCSF, my friends, and my family. Firstly, I am very grateful to my advisor, Jay Debnath, for offering me a place in his lab after a stressful first year of graduate school during which I was uncertain if I would successfully complete a PhD. It was in his lab that I found an environment that allowed me to flourish both professionally and personally. Jay was immensely supportive of my independent growth and gave me the time and space to develop a research project over which I felt ownership. The genuine interest and belief in my project allowed me to maintain perseverance throughout difficult experiments, long nights, and frustrating results. My dissertation committee of Robert Blelloch, Rushika Perera, and Aimee Kao were instrumental in the development of this story. I appreciate their scientific questions and constructive criticism that helped me grow as a scientist and solidify my research.

I must also recognize the critical role my colleagues in the lab played in my project and my development as a scientist. Drew Leidal was my rotation mentor, but continued to serve as a second advisor and sounding board for my dissertation throughout my degree. He taught me how to patiently isolate a nearly imperceptible pellet of small extracellular vesicles from billions of cells – a feat in itself – as well as perform various experimental techniques characterizing this incredibly delicate and precious material. Other members of the lab, including Tan Nguyen, Jordan Ye, Tim Marsh, Alex Tankka, Jen Liu, and Juliet Goldsmith either taught me new techniques or assisted me in experiments. Yu-Hsiu "Tony" Lin in Arun Wiita's lab performed the proteomic analysis. I have to give special acknowledgment to Ari Vlahakis and Teresa Monkkonen, who were not only my lab mates, but also my closest friends, who helped me

maintain perspective and motivation to complete my PhD. Their unwavering support and friendship as I navigated the high highs and low lows of graduate school were invaluable.

I would not have recognized the broader purpose of my degree without UCSF's Office of Career and Professional Development, and the wonderful members of that office. It was through the Motivating Informed Decisions program that I realized that graduate career education was a perfect use of my skills and experience as a graduate student that would allow me to make meaningful change in people's lives every day. Mike Matrone, Laurence Clement, Bill Lindstaedt, Gabi Monsalve, and Naledi Saul became my colleagues and professional role models as I completed a year-long internship with the OCPD, solidifying my confidence that this was a professional community I would be lucky to join. I am incredibly thankful that I had Jay's support to explore and pursue this career path while still working on my dissertation – a privilege that not all graduate students have, and that I hope to address in my career moving forward.

Lastly, I am grateful for the support of my family: my mom, Pat; my dad, Pete; my brother, Eric; and my sister-in-law, Veronica. While they may not have always understood the content of my research, they were always proud of me for becoming a scientist and would ask for laymen's summaries of my work to share with their friends. I am especially indebted to my partner, Brian, whom I met in my second year of graduate school and who has been my rock throughout this process. Thank you for waiting for me on that first date, when I was running late from finishing experiments in the lab. I am so lucky to have found you and excited about our future together.

CONTRIBUTIONS

The work described in this dissertation was done under the direct supervision and guidance of Dr. Jayanta Debnath.

Content in Chapter 1 is modified from the following publication:
Solvik, T. & Debnath, J. At the crossroads of autophagy and infection: Noncanonical roles for ATG proteins in viral replication. *J Cell Biol* **214**, 503–505 (2016).

Ariadne Vlahakis performed the microscopy experiments described in Chapter 2, Figures 1a and 7a. Andrew Leidal performed the nanoparticle tracking analysis experiment described in Chapter 2, Figures 1c and 1d. Tan Nguyen assisted with sample preparation for mass spectrometry in Chapter 2, Figure 2a. Yu-Hsiu "Tony" Lin in the Wiita Lab assisted with sample preparation and performed the mass spectrometry and data analysis in Chapter 2, Figure 2a. Timothy Marsh performed the mouse intraperitoneal injections and whole blood collections for the experiment in Chapter 2, Figure 4g. Tina Solvik performed all other experiments.

Endolysosomal inhibition induces the autophagy-dependent secretion of autophagosomal cargo

By Tina Ann Solvik

ABSTRACT

Autophagy is traditionally viewed as a degradative pathway in which cytoplasmic material is sequestered in double-membrane organelles called autophagosomes and delivered to the lysosome for breakdown. However, autophagy-related proteins (ATGs) have also been implicated in promoting unconventional secretion of proteins. We uncovered a role for the ATG conjugation system in the loading and secretion of proteins in small extracellular vesicles (EVs) separate from the canonical degradative autophagy pathway. To determine the interrelationships between degradative and secretory autophagy, I utilized a proteomic strategy to evaluate the secretome in response to pharmacologically inhibiting endolysosomal acidification, thereby blocking autophagic degradation. In contrast to secretion from cells with baseline autophagic activity, the secretome in response to endolysosomal inhibition is significantly enriched with autophagy-related proteins and autophagic cargoes. This suggests that impaired autophagic degradation in cells results in the redirection of degradative cargo to be secreted outside of the cell. To further investigate this pathway, I characterized the secretion of the autophagy regulator LC3 and its interacting cargo receptors (p62, NBR1, OPTN, NDP52), which selectively deliver cargo to the growing autophagosome but have not previously been implicated in secretory autophagy. These autophagy cargo receptors are secreted as unprotected EV-associated protein in an autophagosome formation-dependent manner, indicating a distinct mechanism requiring classical autophagosome formation for the secretion of these proteins. Furthermore, genetic knockdown of two separate SNARE proteins mediating autophagosome-lysosome fusion

increases secretion of LC3 and autophagy cargo receptors. Overall, these findings establish a new relationship between degradative autophagy and secretory autophagy, in which the impaired degradation of autophagic cargo due to the lack of autophagosome-lysosome fusion results in a concomitant increase in EV-associated secretion of cargo receptors.

TABLE OF CONTENTS

Chapter 1: Introduction **1**

Chapter 2: Endolysosomal inhibition induces the autophagy-dependent secretion of autophagosomal cargo **9**

Chapter 3: Implications of autophagy and secretion in neurodegenerative disease **49**

References **57**

Appendix A: At the crossroads of autophagy and infection: noncanonical roles for ATG proteins in viral replication **68**

Appendix B: The LC3-conjugation machinery specifies the loading of RNA-binding proteins into extracellular vesicles **73**

LIST OF FIGURES

Figure 2.1. BafA1 prevents autophagosome degradation and modulates EV secretion 17

Figure 2.2. Autophagy-dependent secretome under inhibition of endolysosomal acidification is enriched in autophagy-related proteins 19

Figure 2.3. Overlap of autophagy-dependent secretome under inhibition of endolysosomal acidification with baseline autophagy-dependent secretome and autophagosome proteomes. 28

Figure 2.4. Inhibition of endolysosomal acidification promotes secretion of autophagy cargo receptors. 29

Figure 2.5. Secreted autophagy cargo receptors are EV-associated but not membrane-protected. 32

Figure 2.6. ATGs encompassing autophagosome initiation, elongation, and closure and Rab27a are required for secretion of autophagy cargo receptors. 34

Figure 2.7. Genetic inhibition of autophagosome-lysosome fusion promotes secretion of autophagy cargo receptors. 36

Figure 2.8. Model of secretion 38

LIST OF TABLES

Table 2.1. Proteins enriched in autophagy-dependent secretome under inhibition of endolysosomal acidification 21

CHAPTER 1: Introduction

AUTOPHAGY

Autophagy is traditionally viewed as a catabolic pathway in which cytoplasmic material is sequestered in double-membrane organelles called autophagosomes (APs) that are delivered to lysosomes for degradation[1]. Studies in yeast have identified more than 30 autophagy-related proteins (ATGs), many of which have identified mammalian orthologues. The canonical process of autophagy begins with initiation at the phagophore assembly site, mediated by the UNC51-like kinase (ULK) complex – composed of the ATG proteins ULK1/2, ATG13, FIP200, and ATG101. The ULK complex phosphorylates components of a class III phosphatidylinositol 3-kinase (PI3K) complex, consisting of Beclin 1 (ATG6), ATG14 and VPS34 to produce phosphatidylinositol triphosphate (PI3P), which serves as the initial membrane marker recognized by early autophagic effector proteins[2]. Phagophore membrane expansion is mediated by the two ubiquitin-like conjugation systems involving multiple ATGs (ATG3, ATG5, ATG7, ATG10, ATG12) that ultimately lead to the lipidation of microtubule-associated protein light chain 3 (LC3), the mammalian orthologue of ATG8[3]. LC3 is recognized by autophagy cargo receptors that promote the selective capture and engulfment of ubiquitinated proteins, organelles, or microbes[4]. The autophagy cargo receptors p62[5], NBR1[6], OPTN[7], and NDP52[8] bind to LC3 via their LC3-interacting region (LIR) motifs, ensuring the anchoring of the captured cargo in the growing autophagosome membrane[9]. In addition to LC3-conjugation-mediated membrane expansion, closure of the autophagosome requires ATG2A and ATG2B[10]. Once closed, the autophagosome is then trafficked to and fuses with the lysosome, where the inner membrane is susceptible to lysosomal hydrolases, thereby allowing hydrolase access to the autophagosomal cargo for degradation. Fusion of the autophagosome and lysosome requires soluble *N*-ethylmaleimide-sensitive factor attachment protein receptor (SNARE) proteins, which physically

drive the fusion of opposing lipid bilayers[11]. Autophagosome-lysosome fusion is mediated by either of two sets of SNARE complexes, STX17-SNAP29-VAMP8[12] or YKT6-SNAP29-STX7[13], in which one SNARE is docked in the autophagosomal or lysosomal membrane and SNAP29 bridges the opposing SNAREs, facilitating the membrane fusion.

SECRETORY AUTOPHAGY

Despite the classical view of autophagy as a degradative process, ATGs have been recently implicated in secretion, in a process referred to as "secretory autophagy." Canonically, protein secretion involves the presence of an N-terminal signal, resulting in the transfer of the peptide into the ER for subsequent ER-to-Golgi transport. However in unconventional secretion, leaderless proteins lacking signal peptides can be secreted without going through the ER-to-Golgi pathway. One pathway by which these leaderless proteins can be secreted is through uptake by membrane-bound organelles, proposed to be autophagosomes or endosomes, diverted from their normal trafficking toward lysosomes and instead redirected to the plasma membrane and released extracellularly[14].

The field of secretory autophagy emerged in 2010 when parallel studies revealed that two species of yeast, *Saccharaomyces cervisiae* and *Pichia pastoris*, secrete acyl coenzyme A binding protein (Acb1) in an ATG-dependent manner. *S. cervisiae* secretion of Acb1 requires ATGs responsible for elongation of the phagophore membrane (ATG5, ATG7, ATG8, ATG12) and *P. pastoris* secretion requires ATGs responsible for initiation (ATG1, ATG6, ATG9, ATG17) and elongation (ATG8). Both studies determined that Acb1 release does not require autophagosome fusion with the vacuole (i.e. lysosome), but does require ESCRT machinery (VPS23, VPS4), implicating the endosomal pathway, and SNARE-mediated vesicular fusion

with plasma membrane, suggesting the secretion of Acb1 within an autophagosome/endosome hybrid (amphisome)[15,16].

The first evidence of secretory autophagy in mammalian cells was established in the study of IL-1β. The leaderless cytokine had previously been believed to be released via an endolyososome[17], but the discovery of autophagy-dependent Acb1 secretion initiated interest in autophagy regulation of IL-1β release. Not only is IL-1β secretion modulated by induction or inhibition of autophagy, but the autophagosome itself has been implicated in its secretion[18,19]. The first study into secretory autophagy of IL-1β revealed the requirement of ATG5, GRASP55, and Rab8a[18]. IL-1B is incorporated into an autophagosome via translocation across the phagophore membrane in an HSP-90-dependent manner reminiscent of chaperone-mediated autophagy[19]. The most recent study of IL-1β secretion investigated how despite its incorporation into an autophagosome, it evades degradation within the lysosome and is instead directed to secretion. They revealed that a specialized cargo receptor regulator, TRIM16, interacts with IL-1β and delivers it to LC3B+ phagophore in response to lysosomal damage. SNAREs Sec22b, SNAP23 or SNAP29, and STX3 or STX4 mediate AP fusion with plasma membrane, and STX17, required for fusion with lysosome, is not involved[20]. Beyond IL-1β, several other inflammatory mediators without signal peptides are released in an autophagy-dependent manner. HMGB1[18,21] and IL-6[22–24].

ATGs have also been implicated in the secretion of exosomes, small extracellular vesicles with a diameter of 50-200 nm. Small extracellular vesicles are derived from inward budding of the intermediate endocytic compartment, the MVB, to form intraluminal vesicles (ILVs) that, upon fusion of the MVB with the plasma membrane, are liberated into the extracellular space[25].Our lab first identified this connection when we recognized that cells

lacking the ATG12-ATG3 complex have accumulated late endosomes and impaired endolysosomal trafficking. We demonstrated that ATG12-ATG3 interacts with and activates ALIX, thereby promoting exosome release[26]. A later study recognized the role of ATGs in exosome release independent of canonical autophagy, specifically ATG5. ATG5 disassociates the negative regulatory protein ATP6V1E1 from V-ATPase, the proton pump that controls endolysosomal acidification. With ATP6V1E1 detached, V-ATPase is more active, resulting in increased acidification of the MVB and released exosomes. Intriguingly, this study found ATG5 and LC3 enclosed in exosomes, potentially a result of ATG5 recruiting ATP6V1E1 into ILVs in the MVB[27].

Prior to our lab's determination of the LC3-dependent secretion pathway, only one study had established an ATG-dependent secretome. Loss of ATG5 in macrophages revealed increased secretion of 74 proteins relative to WT cells under inflammation-inducing conditions. The majority of these proteins were leaderless and cytosolic. However, they only further analyzed one protein, ferritin heavy chain, but did not analyze the role of other ATGs, making it unclear if the ATG5-dependent release is a canonical or unconventional function of ATG5[20].

Ultimately, studies on secretory autophagy have focused on a limited and heterogeneous list of protein targets and have not elucidated clear cause-effect relationships between ATGs, autophagic vesicular trafficking, and the secretome. Attributing a secretory phenotype to canonical autophagy based on the genetic analysis of a single ATG is no longer viable. Future secretory autophagy studies need to functionally test multiple ATGs when characterizing a phenotype in order to ascertain a general role for autophagy as opposed to a distinct function mediated by individual ATG proteins.

DEFINING THE AUTOPHAGY-DEPENDENT SECRETOME

Our lab addressed these gaps by producing a rigorously defined autophagy-dependent secretome and implicating the ATG conjugation machinery as critical regulators of this pathway. Using a proximity-specific biotinylation proteomics approach, we identified approximately 200 targets of secretion dependent on the critical ATG, LC3. The secretome had high overlap with previously identified LC3 and cumulative ATG8 interactomes[28], and furthermore, revealed a novel interaction between LC3 and proteins released within small extracellular vesicles, or exosomes. Intriguingly, the major targets of secretion were RNA-binding proteins that are not targets of canonical degradative autophagy. Further analysis of LC3 and its directed targets of secretion confirmed that they were released via extracellular vesicles – a pathway we refer to as LC3-dependent extracellular vesicle loading and secretion (LDELS). A separate proteomic approach identifying the extracellular vesicle proteins secreted in an ATG7 or ATG12-dependent manner confirmed a broad LC3-conjugation-dependent secretome[29]. While our proteomics screen established a role for LC3 in secretion, it remains unclear how targets are chosen for secretion rather than degradation and the purpose that secretion serves in various cellular states. The screen was performed in wild-type cells under serum starvation, a condition that induces autophagy and downregulates secretion[30–32]. In addition, the screen was not enriched in LC3-interacting cargo receptors that have previously been found in multiple exosome screens[33,34].

Prior to our discovery of LC3-dependent secretion, we and other groups demonstrated the molecular crosstalk between extracellular vesicle release and autophagy, implicating them as coordinated processes to maintain cellular homeostasis[26,35–38]. This coordination is likely due to connection between the endosomal and autophagy pathways. Both organelles fuse with lysosomes for degradation of their cargo and autophagosomes can fuse with the intermediate

endocytic compartment, the MVB, to form an amphisome prior to delivery to the lysosome[39,40]. As a result, modulating the autophagy pathway effects the quantity of secreted vesicles. Induction of autophagy pharmacologically or by starvation inhibits exosome release, due to the increased fusion of MVBs with autophagosomes and their degradation via the autophagy pathway[40,41]. In addition, inhibiting autophagic degradation pharmacologically or by knockdown of a protein critical for AP-lysosome fusion[42,43] causes an increase in ILV formation in MVBs and subsequent secretion of exosomes[34,41,44]. Exosome release and degradative autophagy are negatively correlated, but how these two pathways coordinate targets of secretion versus degradation remains unclear.

It is well documented that the composition of extracellular vesicles is modified by changes in the cell's physiological state or culture conditions, and that secretion can be induced as a response to stress[33,45–48], suggesting that the level of autophagy in the cell may also impact the content of secreted vesicles. There is already some supporting evidence. In addition to decreasing the release of EVs overall, the induction of autophagy decreases the secretion of LC3 and its cargo[40]. MVBs colocalize with ATG cargo receptors and exosomes contain these receptors in addition to autophagic cargo[34,41]. Furthermore, impaired AP-lysosome fusion results in upregulated exosome release and enhanced secretion of ATG cargo receptors[34,44], suggesting that AP cargo can be diverted into exosomes when they fail to be degraded. A block in degradative autophagy is a biologically relevant condition in neurodegenerative diseases [49–52] and may provide interesting targets of secretion that will further elucidate the mechanism and significance of the LC3-dependent secretory pathway.

In this dissertation, I explore the link between degradative autophagy and secretory autophagy. In Chapter 2, I utilize two distinct mechanisms of impairing degradative autophagy to

demonstrate that impaired autophagosome-lysosome fusion increases the secretion of LC3 as well as autophagy cargo receptors (p62, NBR1, OPTN, NDP52). The secretion of these proteins requires ATGs spanning autophagosome initiation, elongation, and closure, implicating the autophagosome itself in secretion. Furthermore, these proteins are released in a Rab27a-dependent manner and are not membrane-protected, suggesting that in the absence of lysosomal degradation, autophagosome fuses with the MVB to form amphisomes which are subsequently secreted. In Chapter 3, I discuss the biomedical implications for the secretion of undegraded autophagic material, focusing on neurodegenerative disease.

CHAPTER 2: Endolysosomal inhibition induces the autophagy-dependent secretion of autophagosomal cargo

RESULTS

Inhibition of endolysosomal acidification alters the cargo of autophagy-dependent secretion

To determine the effects on autophagy-dependent secretion when flux through the endosomal-autophagy-lysosomal pathway is impaired, we inhibited the acidification of the lysosome, which impairs the fusion and degradation of autophagosomes and their cargo. HEK-293T cells were subject to serum starvation to induce autophagy and treatment with bafilomycin A1 (bafA1), a specific inhibitor of V-ATPase with IC_{50} value of ~1 nM[53], at 20 nM for 16 h, to inhibit lysosomal acidification. To assess the effects of bafA1 on autophagic flux, we used mCherry-GFP-LC3, which reports trafficking of LC3-labeled APs to the lysosome, where the acidic pH quenches the GFP signal but not mCherry. Consistent with previous results, bafA1 treatment blocked GFP quenching in wild-type cells relative to serum starvation alone, resulting in accumulated mCherry+ GFP+ puncta, indicative of reduced autophagic flux. *Atg7-/-* cells, due to their failure to conjugate LC3 to the autophagosome membrane, accumulated cytosolic mCherry-GFP-LC3 (**Figure 2.1a**). Measurement of cell viability by trypan blue exclusion[54] revealed no significant cell death relative to control over the first 8 h of bafA1 treatment; thereafter we observed a gradual increase in death compared to controls at 12 h and 16 h or treatment (**Figure 2.1b**), although levels of death observed were significantly lower than cells treated with digitonin as a positive control. In parallel, we asked whether inhibition of endolysosomal acidification modulated EV secretion. Using nanoparticle tracking analysis (NTA), we revealed that bafA1 does not significantly increase EV production relative to control (**Figure 2.1c**), inconsistent with previous findings[44]. The EVs were 123.3 +/- 2.6 nm in diameter, which corresponded to the size of exosomes (40-150 nm)[55], indicating that bafA1 treatment does not significantly impact the size of small EVs in comparison to those released from control cells (**Figure 2.1d**). To scrutinize

the effect of bafA1 on EV secretion in this study, we subject conditioned media from cells treated for 16 h to differential ultracentrifugation to enrich for large EVs (at 10,000 g) and small EVs (at 100,000 g) (**Figure 2.1e**). To assess the purity of the isolated EVs from these 100,000 g fractions, we measured the secretion of intracellular proteins normally absent or underrepresented in EVs (i.e. associated with the golgi, mitochondria, and nucleus) as well as proteins associated with the endosomal-autophagy-lysosomal pathway that have been previously identified in EVs. We observed high secretion of ATG14, LAMP1, Rab7a, and Rab5a, but minimal secretion of golgi, mitochondria, and nuclear markers. Furthermore, extracellular release of endosomal-autophagy-lysosomal pathway proteins was functionally dependent on ATG7, suggesting a requirement for this autophagy regulator on EV secretion (**Figure 2.1f**). Overall, these results indicate that inhibition of endolysosomal acidification upon bafA1 treatment prevents AP degradation and directs endosomal-autophagy-lysosomal proteins towards secretion in small EVs in an ATG7-dependent manner.

To define the broader ATG7-dependent secretome under endolysosomal inhibition, we performed tandem-mass tag-based quantitative proteomics comparing 100,000 g fractions from bafA1-treated wild-type and *Atg7-/-* cells. We identified 182 proteins with statistically significant enrichment in 100,000 g fractions from wild-type relative to *Atg7-/-* cells ((WT:*Atg7-/-*)>1.5; $p<0.05$). The ATG7-dependent secretome under endolysosomal inhibition included LC3/ATG8 isoforms (LC3B, GABARAP, GABARAPL2), autophagy cargo receptors (p62/SQSTM1, NBR1, OPTN, NDP52/CALCOCO2, etc.), and autophagosome machinery (FIP200, ULK1, Beclin-1, etc.). In contrast, none of the RNA-binding proteins recently identified as targets of LDELS (HNRNPK, SAFB, LARP1, G3BP1, and SF3A1)[29] were significantly enriched in these 100,000 g fractions (**Figure 2.2a, Table 2.1**). Five of the six LC3/ATG8 isoforms were amongst

the top proteins connected to the secretome, and we identified multiple proteins in common with the ATG8 interactome[28] (**Figures 2.2b-c**). Direct comparison of the ATG7-dependent secretome under endolysosomal inhibition and under baseline autophagic conditions[29] reveals only partial overlap, indicating the protein content of the 100,000 g fractions is altered based on the state of autophagic flux in the cell (**Figure 2.2d**). Gene ontology (GO) analyses of this secretome highlighted enrichment in proteins related to autophagy and demonstrated that proteins found in diverse intracellular and organelle compartments were significantly enriched in these fractions, rather than RNA binding proteins, proteins associated with classical secretion, or proteins found in the extracellular space (**Figures 2.2e-f**). Furthermore, 12 proteins in this secretome overlapped with previously identified targets of LDELS (**Figures 2.3a-b**). Remarkably, 27 and 18 proteins in the ATG7-dependent secretome overlapped with targets previously identified in the proteomes of classifical degradative autophagosomes following chloroquine (CQ) and bafA1 treatment, respectively (**Figures 2.3c-f**) [29,56,57]. These results suggest that while at baseline levels of autophagy, the autophagy-dependent secretome is enriched in RNA-binding proteins[29], blocking the degradation of autophagosomes results in the enhanced ATG7-dependent secretion of autophagy-related proteins and known autophagic cargoes. In total, these findings indicate that proteins normally degraded in the lysosome via autophagy can be secreted extracellularly upon endolyososomal inhibition.

Inhibition of endolysosomal acidification induces secretion of autophagic cargo in small extracellular vesicles

To further define the secretion of autophagic cargo under endolysosomal inhibition, we measured secreted protein levels relative to untreated cells. BafA1 treatment led to a striking

increase in the secretion of LC3 and ATG cargo receptors (p62, NBR1, OPTN, NDP52) in the 100,000 g fraction, while canonical exosome markers (TSG101, ALIX, CD9) underwent little change in secreted levels, indicating that this pathway is regulated separately from exosomes (**Figure 2.4a-b**). A time course analysis of secretion of LC3 and the ATG cargo receptors revealed that this release in 100,000 g occurs within several hours of initial intracellular accumulation (**Figure 2.4c**). Notably, the robust EV secretion of these targets was observed as early as 4 h, timepoints prior to any significant cell death associated with bafA1 treatment (**Figure 2.1b**). We then used an independent method of blocking lysosome acidification, CQ, a lysosomotropic agent that acts as a proton trap in the lysosomal lumen, thereby raising the pH. Similar to bafA1, cells treated with 25 μM CQ under serum starvation for 24 h had minimal effects on cell death (**Figure 2.4d**), and secreted increased levels of LC3 and autophagy cargo receptors, but not exosome markers, relative to control treated cells (**Figure 2.4e-f**). Therefore two distinct methods of inhibiting endolysosomal acidification increase secretion of autophagic cargo relative to untreated cells. To confirm this effect is not unique to HEK293Ts, we repeated this experiment *in vivo* in homozygous transgenic GFP-LC3 mice. We treated mice with 60 mg/kg CQ for 3 days, before collecting whole blood and isolating the 100,000 g fraction from plasma by ultracentrifugation. Again, GFP-LC3 and the cargo receptor p62 was secreted at significantly higher levels in CQ-treated mice compared to untreated controls (**Figure 2.4g-h**). We also observed increased levels of EV-associated secretion of NBR1 in the plasma of CQ-treated mice, although this difference was not significantly different. We conclude that blocking autophagosome degradation by inhibiting endolysosomal acidification results in extracellular release of autophagy cargo receptors *in vitro* and *in vivo*.

To further characterize the nature of secretion of LC3 and autophagy cargo receptors, we assessed the size, density, and membrane protection of the secreted material. We first compared ultracentrifugation fractions of 10,000 g to detect large EVs (150-1,000 nm), 100,000 g to detect small EVs (40-150 nm), and TCA-precipitated 100,000 g supernatant to detect soluble protein. LC3 and the cargo receptors were significantly enriched in the 100,000 g fraction relative to the 10,000 g and TCA fractions, indicating they cofractionate with small EVs, consistent with the exosome marker CD9 (**Figure 2.5a-b**). To determine if cargo receptors are secreted within the lumen of small EVs or cofractionate with these vesicles, we measured their protection from protease in the presence and absence of detergent. In contrast to TSG101, we found that p62, NBR1, and OPTN were not membrane-protected from proteases, indicating they do not reside within the lumen of small EVs (**Figure 2.5c-d**). To confirm that the cargo receptors co-fractionate with EVs, despite their lack of membrane protection, we further purified small EVs via linear sucrose density gradient. We demonstrated LC3 and the autophagy cargo receptors fractionate in 100,000 g fractions overlapping in density with CD9, a canonical exosome marker (**Figure 2.5e-f**). Overall, we demonstrated that autophagic cargo secreted under endolysosomal inhibition are small EV-associated, but not within membrane-protected vesicular compartments.

Autophagosome formation and Rab27a are required for secretion of autophagic cargo during endolysosomal inhibition

To determine the mechanism of packaging of autophagic cargo in vesicles destined for secretion, we investigated the requirement for autophagosome formation machinery and nSMase2-dependent ILV budding. First, we assessed the requirement of autophagy beyond ATG7 using an array of *Atg* CRISPR knock-out cells unable to form mature autophagosomes. We specifically

interrogated the autophagosome formation steps of initiation of the phagophore membrane by FIP200[58] and ATG14[59–61], elongation by the LC3 conjugation machinery ATG7 and ATG12[3], and closure by ATG2A/ATG2B[10]. Since it was previously identified that *Atg* knockouts exhibit differences in EV production[29], we normalized EV lysates by protein concentration in our assays. We demonstrated that secretion of autophagic cargo requires ATG7 and ATG12, similar to LDELS[29], as well as all other autophagosome machinery probed: FIP200, ATG14, and ATG2A/ATG2B (**Figure 2.6a-b**). This indicates that steps from initiation through closure of the phagophore, thereby the formation of mature autophagosomes, is essential for the release of autophagic cargo. While previous studies have implicated individual ATGs in secretory autophagy[62], this is the first demonstration of the functional requirement of multiple key steps in autophagosome formation (initiation, elongation, and closure) for autophagy-dependent secretion, suggesting the mature autophagosome itself is upstream of the secretory event.

To determine the mechanism of release of packaged autophagic cargo, we interrogated the role of Rab27a, which has been identified as necessary for fusion of the MVB[63] or autophagosome-MVB fusion organelle, the amphisome[64], with the plasma membrane to release their contents into the extracellular space (**Figure 2.6c-d**). Depletion of Rab27a resulted in a significant, but not complete, decrease in secretion of LC3 and the cargo receptors, suggesting the utilization additional factors in plasma membrane fusion. Ultimately, secretion of autophagy cargo receptors requires the formation of an autophagosome, as well as Rab27a for fusion of the autophagosome, or other downstream organelles, such as an amphisome or autolysosome, with the plasma membrane.

Genetic inhibition of autophagosome-lysosome fusion promotes secretion of autophagic cargo

While bafA1 is widely used to block autophagosome-lysosome fusion, it has been noted that this is secondary to its direct effect, deacidification of the lysosome[65]. To determine whether secreted autophagic cargo are derived from autophagosomes that have not yet fused with lysosomes or from de-acidified autolysosomes, we examined secretion by cells genetically impaired in autophagosome-lysosome fusion. Specifically, we depleted cells of SNAP29 and VAMP8, two N-ethylmaleimide-sensitive factor attachment protein receptor (SNARE) proteins which interact to mediate autophagosome and lysosome membrane fusion[12]. First, we confirmed that SNAP29 and VAMP8 loss would have a similar effect on autophagic flux as bafA1, using mCherry-GFP-LC3. Consistent with previous studies, knockdown of the genes alone resulted in accumulated GFP+ mCherry+ LC3 puncta, indicative of reduced autophagic flux similar to non-targeting cells treated with bafA1 (**Figure 2.7a**). Depletion of SNAP29 and VAMP8 led to a significant increase in secreted LC3 and the autophagy cargo receptors (**Figures 2.7b-e**), similar to the effect of bafA1 on wild-type cells. However, knock-down of STX17, another protein in the SNARE complex, had a non-significant effect on secretion (data not shown), presumably due to its role in autophagosome initiation in addition to autophagosome-lysosome fusion[66,67].

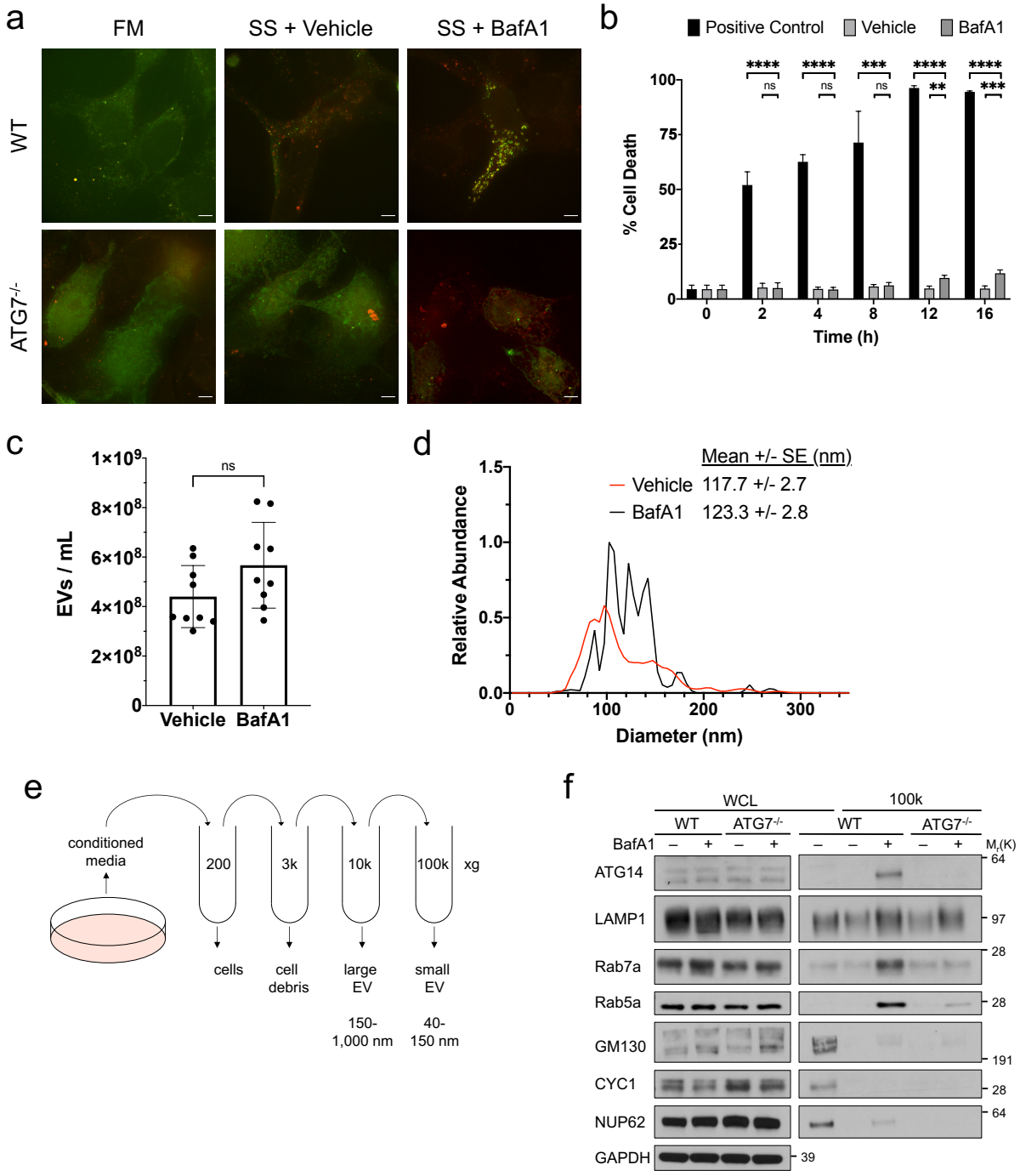

Figure 2.1. BafA1 prevents autophagosome degradation and modulates EV secretion
(a) Wild-type (WT) and ATG7-/- HEK293Ts transfected with mCherry-GFP-LC3 were grown in full media (FM), treated with vehicle in serum-free media (SS), or treated with 20 nM bafilomycin A1 (bafA1) in serum-free media (BafA1) for 16 h. Scale bar, 5 µm. (b) Cell death in WT cells treated with 48 µM digitonin in full media (Positive Control), treated with vehicle in serum-free media (Vehicle), or treated with 20 nM bafA1 in serum-free media (20 nM BafA1)

for indicated time periods quantified using trypan blue staining (mean ± s.e.; n=3). Statistical significance calculated by ordinary one-way analysis of variance followed by Sidak multiple comparisons test for comparison between pairs (n.s. = not significant, ** = p-value < 0.01, *** = p-value < 0.001, **** = p-value < 0.0001). (c) Nanoparticle tracking analysis of CM from equal numbers of WT cells treated with vehicle in serum-free media (DMSO) or 20 nm bafA1 in serum-free media (BafA1) to determine EV number (mean ± s.e.m.; n=3). Statistical significance calculated by unpaired two-tailed t-test (n.s.=not significant). (d) EV size distribution from indicated cell treatments in Panel c (mean ± s.e.; n=3). (e) Schematic of 100,000 g EV isolation by differential ultracentrifugation. (f) Whole cell lysate (WCL) and 100,000 g EV (100k) fractions harvested from WT and ATG7-/- cells treated with vehicle or 20 nM bafA1 in serum-free media for 16 h were collected, normalized for protein concentration, and immunoblotted to detect indicated organelle markers.

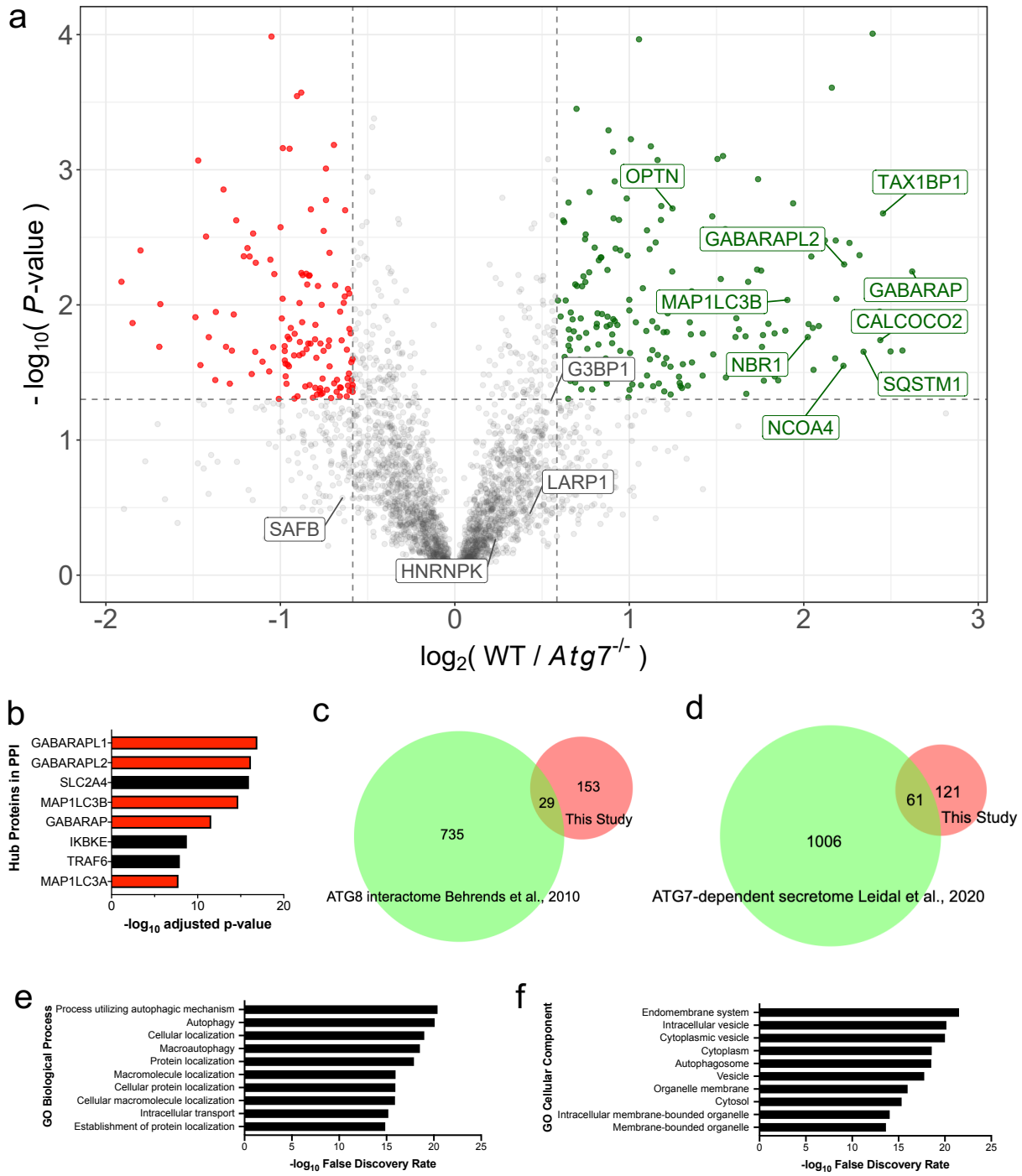

Figure 2.2. Autophagy-dependent secretome under inhibition of endolysosomal acidification is enriched in autophagy-related proteins

(a) Volcano plot of proteins identified in 100,000 g EV (100k) fractions harvested from wild-type (WT) and ATG7-/- HEK293T cells treated with 20 nM bafA1 in serum-free media for 16h and quantified by tandem mass tag (TMT) mass spectrometry. TMT labeled proteins from 3 biological replicates were plotted according to their -$\log_{10}$ p-values as determined by two-sample t-test and their $\log_2$ fold enrichment (WT/ATG7-/-). Red dots: proteins identified that have a p-

value < 0.05 and fold-change < -1.5 and thus are relatively enriched in 100k from ATG7-/- cells treated with bafA1. Grey dots: proteins identified that have a p-value > 0.05 and/or fold-change between -1.5 and 1.5 and thus are not relatively enriched in 100k from WT or ATG7-/- cells treated with bafA1. Green dots: proteins identified that have a p-value < 0.05 and fold change > 1.5 and thus are relatively enriched in 100k from WT cells treated with bafA1. (b) Ranked list by $-\log_{10}$ adjusted p-value of proteins with the greatest connectivity to the 182 proteins enriched in 100k from WT cells treated with bafA1 relative to ATG7-/- cells treated with bafA1 as determined by the protein-protein interaction (PPI) hub protein tool in the Enrichr gene set enrichment analysis web server. LC3/ATG8 family members are highlighted in red. (c) Venn diagram showing the overlap of proteins enriched in 100k from WT cells treated with bafA1 relative to 100k from ATG7-/- cells treated with bafA1 with the ATG8 intracellular interactome defined in Behrends *et al*. 2010. List of enriched proteins is provided in Table 1. (d) Venn diagram showing the overlap of proteins enriched in 100k from WT cells treated with bafA1 relative to 100k from ATG7-/- cells treated with bafA1 with the ATG7-dependent secretome defined in Leidal *et al.* 2020. List of enriched proteins is provided in Table 1. (e) Gene ontology (GO) enrichment analysis of the 182 proteins enriched in 100k from WT cells treated with bafA1 relative to 100k from ATG7-/- cells treated with bafA1 with the top ten terms for biological process plotted according to $-\log_{10}$ false discovery rate. (f) GO enrichment analysis of the 182 proteins enriched in 100k from WT cells treated with bafA1 relative to 100k from ATG7-/- cells treated with bafA1 with the top ten terms for cellular component plotted according to $-\log_{10}$ false discovery rate.

Table 2.1. Proteins enriched in autophagy-dependent secretome under inhibition of endolysosomal acidification

182 proteins enriched in 100,000 g EV (100k) fractions harvested from wild-type (WT) HEK293T cells treated with 20 nM bafA1 relative to 100k fraction harvested from ATG7-/- cells treated with 20 nM bafA1. Proteins identified by name, uniprot ID, gene name, p-value, and log_2 fold enrichment (WT/ATG7-/-).

Uniprot ID	Gene	Protein	P-value	Log_2(Fold-Change)
O95166	GABARAP	Gamma-aminobutyric acid receptor-associated protein	0.005661556	2.62129678
P02792	FTL	Ferritin light chain	0.021773366	2.565518083
P02794	FTH1	Ferritin heavy chain	0.022109262	2.497207754
Q86VP1	TAX1BP1	Tax1-binding protein 1	0.00210311	2.454087101
Q13137	CALCOCO2	Calcium-binding and coiled-coil domain-containing protein 2	0.018230688	2.438417275
P17612	PRKACA	cAMP-dependent protein kinase catalytic subunit alpha	0.011205547	2.434870993
A3KN83	SBNO1	Protein strawberry notch homolog 1	9.84E-05	2.394471646
Q13501	SQSTM1	Sequestosome-1	0.022196023	2.342407645
Q9NQC7	CYLD	Ubiquitin carboxyl-terminal hydrolase CYLD	0.004287523	2.319304451
Q9NR28	DIABLO	Diablo homolog, mitochondrial	0.003478699	2.261795153
P60520	GABARAPL2	Gamma-aminobutyric acid receptor-associated protein-like 2	0.005013484	2.231014392
Q13772	NCOA4	Nuclear receptor coactivator 4	0.028232656	2.227108801
P10644	PRKAR1A	cAMP-dependent protein kinase type I-alpha regulatory subunit	0.009020855	2.186913661
P60709	ACTB	Actin, cytoplasmic 1	0.003340117	2.182985917
Q9ULG6	CCPG1	Cell cycle progression protein 1	0.02487707	2.179908892
Q9P1Z2	CALCOCO1	Calcium-binding and coiled-coil domain-containing protein 1	0.000246982	2.160650872
A6NKT7	RGPD3	RanBP2-like and GRIP domain-containing protein 3	0.00333469	2.1210456
P21796	VDAC1	Voltage-dependent anion-selective channel protein 1	0.014336043	2.086194684
P31321	PRKAR1B	cAMP-dependent protein kinase type I-beta regulatory subunit	0.030251917	2.055828903
Q9NQG6	MIEF1	Mitochondrial dynamics protein MID51	0.014814491	2.051987162
Q9NYA4	MTMR4	Myotubularin-related protein 4	0.004386739	2.042971197
Q9BWH2	FUNDC2	FUN14 domain-containing protein 2	0.013872062	2.027525856
Q14596	NBR1	Next to BRCA1 gene 1 protein	0.017299505	2.022793787

Uniprot ID	Gene	Protein	P-value	Log_2(Fold-Change)
P63165	SUMO1	Small ubiquitin-related modifier 1	0.00177225	1.938929413
Q9GZQ8	MAP1LC3B	Microtubule-associated proteins 1A/1B light chain 3B	0.009191918	1.90610193
Q9UKA4	AKAP11	A-kinase anchor protein 11	0.015513757	1.893865481
O00429	DNM1L	Dynamin-1-like protein	0.030588659	1.868900651
Q14145	KEAP1	Kelch-like ECH-associated protein 1	0.036203168	1.853448843
P45880	VDAC2	Voltage-dependent anion-selective channel protein 2	0.033886228	1.833601867
Q969H8	MYDGF	Myeloid-derived growth factor	0.016250688	1.832601583
P17152	TMEM11	Transmembrane protein 11, mitochondrial	0.013811064	1.79723727
Q9BT25	HAUS8	HAUS augmin-like complex subunit 8	0.036396168	1.771108141
Q9Y6C9	MTCH2	Mitochondrial carrier homolog 2	0.016731908	1.766235931
Q5T0D9	TPRG1L	Tumor protein p63-regulated gene 1-like protein	0.02044599	1.760395846
P49792	RANBP2	E3 SUMO-protein ligase RanBP2	0.005578968	1.7554435
Q9H6S1	AZI2	5-azacytidine-induced protein 2	0.001174157	1.738084008
Q15154	PCM1	Pericentriolar material 1 protein	0.005476891	1.732445559
Q8TDY2	RB1CC1	RB1-inducible coiled-coil protein 1	0.006752136	1.681121642
Q15025	TNIP1	TNFAIP3-interacting protein 1	0.045503522	1.670538151
P54819	AK2	Adenylate kinase 2, mitochondrial	0.017082454	1.666080091
O75385	ULK1	Serine/threonine-protein kinase ULK1	0.010083791	1.635712774
Q96NB1	FOPNL	LisH domain-containing protein FOPNL	0.015150176	1.62824819
Q9NPJ6	MED4	Mediator of RNA polymerase II transcription subunit 4	0.012554917	1.613328095
O95873	C6orf47	Uncharacterized protein C6orf47	0.017292853	1.608468753
P27797	CALR	Calreticulin	0.034446121	1.55364167
Q96M27	PRRC1	Protein PRRC1	0.002751053	1.550304861
Q8TC07	TBC1D15	TBC1 domain family member 15	0.000791322	1.536976035
O75665	OFD1	Oral-facial-digital syndrome 1 protein	0.006433891	1.524189492
Q9UKG1	APPL1	DCC-interacting protein 13-alpha	0.000831964	1.505145125
Q9NS69	TOMM22	Mitochondrial import receptor subunit TOM22 homolog	0.023246768	1.480947144
Q9BV40	VAMP8	Vesicle-associated membrane protein 8	0.002211841	1.475266717
O95399	UTS2	Urotensin-2	0.016272289	1.420921727
Q6ICB0	DESI1	Desumoylating isopeptidase 1	0.033382219	1.420144268
Q9BSY9	DESI2	Desumoylating isopeptidase 2	0.026646766	1.359091852
O94830	DDHD2	Phospholipase DDHD2	0.007925354	1.357562741
O43399	TPD52L2	Tumor protein D54	0.016528018	1.352630477

Uniprot ID	Gene	Protein	P-value	Log_2(Fold-Change)
P10155	TROVE2	60 kDa SS-A/Ro ribonucleoprotein	0.013456403	1.346581062
Q9Y6I9	TEX264	Testis-expressed sequence 264 protein	0.039637208	1.33544437
P22694	PRKACB	cAMP-dependent protein kinase catalytic subunit beta	0.027477997	1.306785409
Q12899	TRIM26	Tripartite motif-containing protein 26	0.041241136	1.301948257
P63279	UBE2I	SUMO-conjugating enzyme UBC9	0.039873512	1.293408119
P67870	CSNK2B	Casein kinase II subunit beta	0.037850784	1.288669564
Q15084	PDIA6	Protein disulfide-isomerase A6	0.034021405	1.284813804
Q96CV9	OPTN	Optineurin	0.001933402	1.247421152
P16615	ATP2A2	Sarcoplasmic/endoplasmic reticulum calcium ATPase 2	0.00566552	1.245952066
Q9Y277	VDAC3	Voltage-dependent anion-selective channel protein 3	0.045992892	1.236705167
Q15293	RCN1	Reticulocalbin-1	0.028667905	1.235797623
P07237	P4HB	Protein disulfide-isomerase	0.011549926	1.219981871
Q658Y4	FAM91A1	Protein FAM91A1	0.015879417	1.215013125
P11021	HSPA5	78 kDa glucose-regulated protein	0.024740822	1.211591938
Q15041	ARL6IP1	ADP-ribosylation factor-like protein 6-interacting protein 1	0.043679625	1.200338639
Q9HA65	TBC1D17	TBC1 domain family member 17	0.027312508	1.199378372
P30040	ERP29	Endoplasmic reticulum resident protein 29	0.015926314	1.196722969
P07197	NEFM	Neurofilament medium polypeptide	0.00185507	1.183152983
Q9BSB4	ATG101	Autophagy-related protein 101	0.002352739	1.181346413
O60313	OPA1	Dynamin-like 120 kDa protein, mitochondrial	0.038133005	1.169224916
P07199	CENPB	Major centromere autoantigen B	0.023473555	1.163129628
Q9BWD3	FAM127B	Protein FAM127B	0.000847684	1.161839136
Q9UPN4	CEP131	Centrosomal protein of 131 kDa	0.014742813	1.159572115
Q9UHD2	TBK1	Serine/threonine-protein kinase TBK1	0.003450459	1.151030935
Q9UMX0	UBQLN1	Ubiquilin-1	0.039992662	1.136614529
Q9UM82	SPATA2	Spermatogenesis-associated protein 2	0.021618881	1.132401505
Q8TD19	NEK9	Serine/threonine-protein kinase Nek9	0.013203895	1.131817607
P46060	RANGAP1	Ran GTPase-activating protein 1	0.000670819	1.12326431
Q9NP72	RAB18	Ras-related protein Rab-18	0.02527698	1.118135089
Q8NC44	FAM134A	Protein FAM134A	0.003871366	1.116394943
Q96HR8	NAF1	H/ACA ribonucleoprotein complex non-core subunit NAF1	0.033317026	1.101697773
Q6PIU2	NCEH1	Neutral cholesterol ester hydrolase 1	0.002808146	1.101250499

Uniprot ID	Gene	Protein	P-value	Log_2(Fold-Change)
P36941	LTBR	Tumor necrosis factor receptor superfamily member 3	0.015596447	1.097394965
Q12981	BNIP1	Vesicle transport protein SEC20	0.007531027	1.077471196
P36551	CPOX	Oxygen-dependent coproporphyrinogen-III oxidase, mitochondrial	0.039310893	1.067473976
P04792	HSPB1	Heat shock protein beta-1	0.000108323	1.055509541
Q99442	SEC62	Translocation protein SEC62	0.013447552	1.037230192
Q8WXW3	PIBF1	Progesterone-induced-blocking factor 1	0.03881136	1.017493942
O75143	ATG13	Autophagy-related protein 13	0.000594066	1.008862267
P24534	EEF1B2	Elongation factor 1-beta	0.022696291	1.003779209
P26374	CHML	Rab proteins geranylgeranyltransferase component A 2	0.042508733	1.000946567
Q9H4A6	GOLPH3	Golgi phosphoprotein 3	0.010979159	0.999828084
Q9Y371	SH3GLB1	Endophilin-B1	0.009168595	0.99964662
P30101	PDIA3	Protein disulfide-isomerase A3	0.048394592	0.995289323
P23284	PPIB	Peptidyl-prolyl cis-trans isomerase B	0.030006021	0.993730016
Q8NI08	NCOA7	Nuclear receptor coactivator 7	0.004309707	0.989894255
Q14974	KPNB1	Importin subunit beta-1	0.001631935	0.985065425
Q96KG9	SCYL1	N-terminal kinase-like protein	0.029720666	0.959263434
Q12834	CDC20	Cell division cycle protein 20 homolog	0.003944309	0.948474758
Q96AG4	LRRC59	Leucine-rich repeat-containing protein 59	0.021875965	0.948253255
Q9NWV8	BABAM1	BRISC and BRCA1-A complex member 1	0.002351318	0.940832491
Q8WUX9	CHMP7	Charged multivesicular body protein 7	0.014088699	0.931640388
P14625	HSP90B1	Endoplasmin	0.028082372	0.926122083
P52292	KPNA2	Importin subunit alpha-1	0.003828987	0.92133271
Q9BSJ8	ESYT1	Extended synaptotagmin-1	0.013173842	0.916474677
P51572	BCAP31	B-cell receptor-associated protein 31	0.001218218	0.916256205
Q8NEB9	PIK3C3	Phosphatidylinositol 3-kinase catalytic subunit type 3	0.002286463	0.909534456
O75396	SEC22B	Vesicle-trafficking protein SEC22b	0.012754017	0.907802777
P21964	COMT	Catechol O-methyltransferase	0.000735966	0.906661806
O14974	PPP1R12A	Protein phosphatase 1 regulatory subunit 12A	0.028961844	0.905878125
P13667	PDIA4	Protein disulfide-isomerase A4	0.033287674	0.903517401
Q13162	PRDX4	Peroxiredoxin-4	0.016548828	0.90209015
P62820	RAB1A	Ras-related protein Rab-1A	0.019201511	0.901523988
P63167	DYNLL1	Dynein light chain 1, cytoplasmic	0.026808344	0.900657309

Uniprot ID	Gene	Protein	P-value	Log_2(Fold-Change)
Q9Y394	DHRS7	Dehydrogenase/reductase SDR family member 7	0.014051672	0.889227176
Q96CS3	FAF2	FAS-associated factor 2	0.000510662	0.880638354
Q9Y5B9	SUPT16H	FACT complex subunit SPT16	0.012218089	0.875222857
Q96JJ7	TMX3	Protein disulfide-isomerase TMX3	0.005515443	0.87463842
P12004	PCNA	Proliferating cell nuclear antigen	0.038236395	0.871450352
O15155	BET1	BET1 homolog	0.014423959	0.870285501
Q9Y2D8	SSX2IP	Afadin- and alpha-actinin-binding protein	0.036294793	0.867961676
Q9P0L0	VAPA	Vesicle-associated membrane protein-associated protein A	0.024891607	0.864878055
Q99614	TTC1	Tetratricopeptide repeat protein 1	0.030151961	0.863586029
Q6DD88	ATL3	Atlastin-3	0.011689448	0.84357797
P24386	CHM	Rab proteins geranylgeranyltransferase component A 1	0.004451191	0.839465232
P20645	M6PR	Cation-dependent mannose-6-phosphate receptor	0.03188103	0.837820011
Q96A49	SYAP1	Synapse-associated protein 1	0.004461263	0.835579961
Q9H078	CLPB	Caseinolytic peptidase B protein homolog	0.004675601	0.825270203
Q99942	RNF5	E3 ubiquitin-protein ligase RNF5	0.019653094	0.822913947
O00505	KPNA3	Importin subunit alpha-4	0.011545542	0.817782718
P18031	PTPN1	Tyrosine-protein phosphatase non-receptor type 1	0.013801499	0.814080304
P61026	RAB10	Ras-related protein Rab-10	0.014587058	0.811941407
Q8WZA9	IRGQ	Immunity-related GTPase family Q protein	0.025882851	0.803612394
Q8IZ07	ANKRD13A	Ankyrin repeat domain-containing protein 13A	0.003767815	0.801459178
Q96HY6	DDRGK1	DDRGK domain-containing protein 1	0.028608054	0.794603776
P53396	ACLY	ATP-citrate synthase	0.042171192	0.787022678
Q01469	FABP5	Fatty acid-binding protein, epidermal	0.001461956	0.771785806
O75694	NUP155	Nuclear pore complex protein Nup155	0.005740588	0.769866377
P12814	ACTN1	Alpha-actinin-1	0.03338147	0.76371946
Q7Z3C6	ATG9A	Autophagy-related protein 9A	0.021141022	0.759308247
P19367	HK1	Hexokinase-1	0.016133949	0.752556221
Q9H0U4	RAB1B	Ras-related protein Rab-1B	0.003011718	0.749935306
O95292	VAPB	Vesicle-associated membrane protein-associated protein B/C	0.006776302	0.747893511

Uniprot ID	Gene	Protein	P-value	Log_2(Fold-Change)
P42566	EPS15	Epidermal growth factor receptor substrate 15	0.003265947	0.74633098
P29373	CRABP2	Cellular retinoic acid-binding protein 2	0.006146825	0.736959574
P13861	PRKAR2A	cAMP-dependent protein kinase type II-alpha regulatory subunit	0.007279451	0.729136385
Q14457	BECN1	Beclin-1	0.042119462	0.724493333
Q8WVD5	RNF141	RING finger protein 141	0.012599962	0.721635005
P61006	RAB8A	Ras-related protein Rab-8A	0.026260301	0.715515926
Q14677	CLINT1	Clathrin interactor 1	0.025464528	0.714451261
O75410	TACC1	Transforming acidic coiled-coil-containing protein 1	0.017413251	0.712036216
Q99729	HNRNPAB	Heterogeneous nuclear ribonucleoprotein A/B	0.032713619	0.709610641
P48066	SLC6A11	Sodium- and chloride-dependent GABA transporter 3	0.007241431	0.700204296
O14966	RAB29	Ras-related protein Rab-7L1	0.000354102	0.697312744
Q96F24	NRBF2	Nuclear receptor-binding factor 2	0.007047901	0.690222804
Q13185	CBX3	Chromobox protein homolog 3	0.037503479	0.689747053
Q9NT62	ATG3	Ubiquitin-like-conjugating enzyme ATG3	0.032227222	0.688439757
Q96A57	TMEM230	Transmembrane protein 230	0.01569375	0.681524356
P62745	RHOB	Rho-related GTP-binding protein RhoB	0.012800724	0.674884907
O95857	TSPAN13	Tetraspanin-13	0.011383802	0.664246561
Q9NTJ5	SACM1L	Phosphatidylinositide phosphatase SAC1	0.036551796	0.66241358
O75368	SH3BGRL	SH3 domain-binding glutamic acid-rich-like protein	0.017853602	0.660693908
Q8NBJ5	COLGALT1	Procollagen galactosyltransferase 1	0.028998303	0.660316737
Q9NZ52	GGA3	ADP-ribosylation factor-binding protein GGA3	0.021670631	0.659879048
P54727	RAD23B	UV excision repair protein RAD23 homolog B	0.031857283	0.657514813
Q6RW13	AGTRAP	Type-1 angiotensin II receptor-associated protein	0.015229189	0.653056178
P43003	SLC1A3	Excitatory amino acid transporter 1	0.001748001	0.651693103
Q13505	MTX1	Metaxin-1	0.020058118	0.651232821
P08238	HSP90AB1	Heat shock protein HSP 90-beta	0.049509084	0.649860437
O94826	TOMM70A	Mitochondrial import receptor subunit TOM70	0.034088388	0.640038638
P78318	IGBP1	Immunoglobulin-binding protein 1	0.009268242	0.635295593

Uniprot ID	**Gene**	**Protein**	**P-value**	**Log_2(Fold-Change)**
Q12893	TMEM115	Transmembrane protein 115	0.024276707	0.629252594
P08183	ABCB1	Multidrug resistance protein 1	0.002438499	0.626933227
P30153	PPP2R1A	Serine/threonine-protein phosphatase 2A 65 kDa regulatory subunit A alpha isoform	0.002371456	0.620967167
Q99570	PIK3R4	Phosphoinositide 3-kinase regulatory subunit 4	0.012189339	0.606257539
Q8TC12	RDH11	Retinol dehydrogenase 11	0.009278043	0.591211018

a

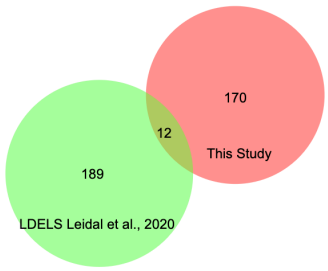

c

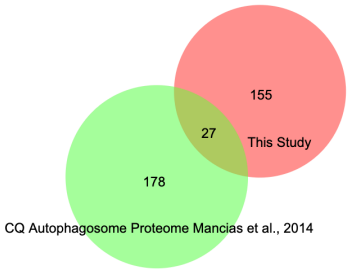

e

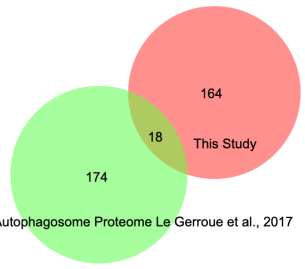

b

Gene	Protein
SQSTM1	Sequestosome-1
MAP1LC3B	Microtubule-associated proteins 1A/1B light chain 3B
RANBP2	E3 SUMO-protein ligase RanBP2
TPD52L2	Tumor protein D54
NEK9	Serine/threonine-protein kinase Nek9
RANGAP1	Ran GTPase-activating protein 1
EEF1B2	Elongation factor 1-beta
SCYL1	N-terminal kinase-like protein
TTC1	Tetratricopeptide repeat protein 1
SYAP1	Synapse-associated protein 1
IRGQ	Immunity-related GTPase family Q protein
ATG3	Ubiquitin-like-conjugating enzyme ATG3

d

Gene	Protein
FTL	Ferritin light chain
FTH1	Ferritin heavy chain
TAX1BP1	Tax1-binding protein 1
CALCOCO2	Calcium-binding and coiled-coil domain-containing protein 2
PRKACA	cAMP-dependent protein kinase catalytic subunit alpha
SQSTM1	Sequestosome-1
GABARAPL2	Gamma-aminobutyric acid receptor-associated protein-like 2
NCOA4	Nuclear receptor coactivator 4
PRKAR1A	cAMP-dependent protein kinase type I-alpha regulatory subunit
CCPG1	Cell cycle progression protein 1
CALCOCO1	Calcium-binding and coiled-coil domain-containing protein 1
PRKAR1B	cAMP-dependent protein kinase type I-beta regulatory subunit
NBR1	Next to BRCA1 gene 1 protein
MAP1LC3B	Microtubule-associated proteins 1A/1B light chain 3B
KEAP1	Kelch-like ECH-associated protein 1
TPRG1L	Tumor protein p63-regulated gene 1-like protein
RB1CC1	RB1-inducible coiled-coil protein 1
TNIP1	TNFAIP3-interacting protein 1
TBC1D15	TBC1 domain family member 15
VAMP8	Vesicle-associated membrane protein 8
PRKACB	cAMP-dependent protein kinase catalytic subunit beta
OPTN	Optineurin
TBK1	Serine/threonine-protein kinase TBK1
SCYL1	N-terminal kinase-like protein
CHM	Rab proteins geranylgeranyltransferase component A 1
ATG9A	Autophagy-related protein 9A
RHOB	Rho-related GTP-binding protein RhoB

f

Gene	Protein
FTH1	Ferritin heavy chain
TAX1BP1	Tax1-binding protein 1
CALCOCO2	Calcium-binding and coiled-coil domain-containing protein 2
SQSTM1	Sequestosome-1
NCOA4	Nuclear receptor coactivator 4
CCPG1	Cell cycle progression protein 1
NBR1	Next to BRCA1 gene 1 protein
VDAC2	Voltage-dependent anion-selective channel protein 2
PCM1	Pericentriolar material 1 protein
TOMM22	Mitochondrial import receptor subunit TOM22 homolog
RAB18	Ras-related protein Rab-18
HSPB1	Heat shock protein beta-1
BCAP31	B-cell receptor-associated protein 31
CLPB	Caseinolytic peptidase B protein homolog
ACLY	ATP-citrate synthase
ACTN1	Alpha-actinin-1
MTX1	Metaxin-1
HSP90AB1	Heat shock protein HSP 90-beta

Figure 2.3. Overlap of autophagy-dependent secretome under inhibition of endolysosomal acidification with baseline autophagy-dependent secretome and autophagosome proteomes
(a) Venn diagram showing the overlap of proteins enriched in 100k from wild-type (WT) cells treated with bafA1 relative to 100k from ATG7-/- cells treated with bafA1 with the LDELS secretome defined in Leidal *et al*. 2020. List of enriched proteins is provided in Table 1. (b) List of overlapping proteins in (a). (c) Venn diagram showing the overlap of proteins enriched in

100k from WT cells treated with bafA1 relative to 100k from ATG7-/- cells treated with bafA1 with the autophagosome proteome under chloroquine (CQ) treatment defined in Mancias *et al*. 2014. List of enriched proteins is provided in Table 1. (d) List of overlapping proteins in (c). (e) Venn diagram showing the overlap of proteins enriched in 100k from WT cells treated with bafA1 relative to 100k from ATG7-/- cells treated with bafA1 with the autophagosome proteome under bafA1 treatment defined in Le Gerroue *et al*. 2017. List of enriched proteins is provided in Table 1. (f) List of overlapping proteins in (e).

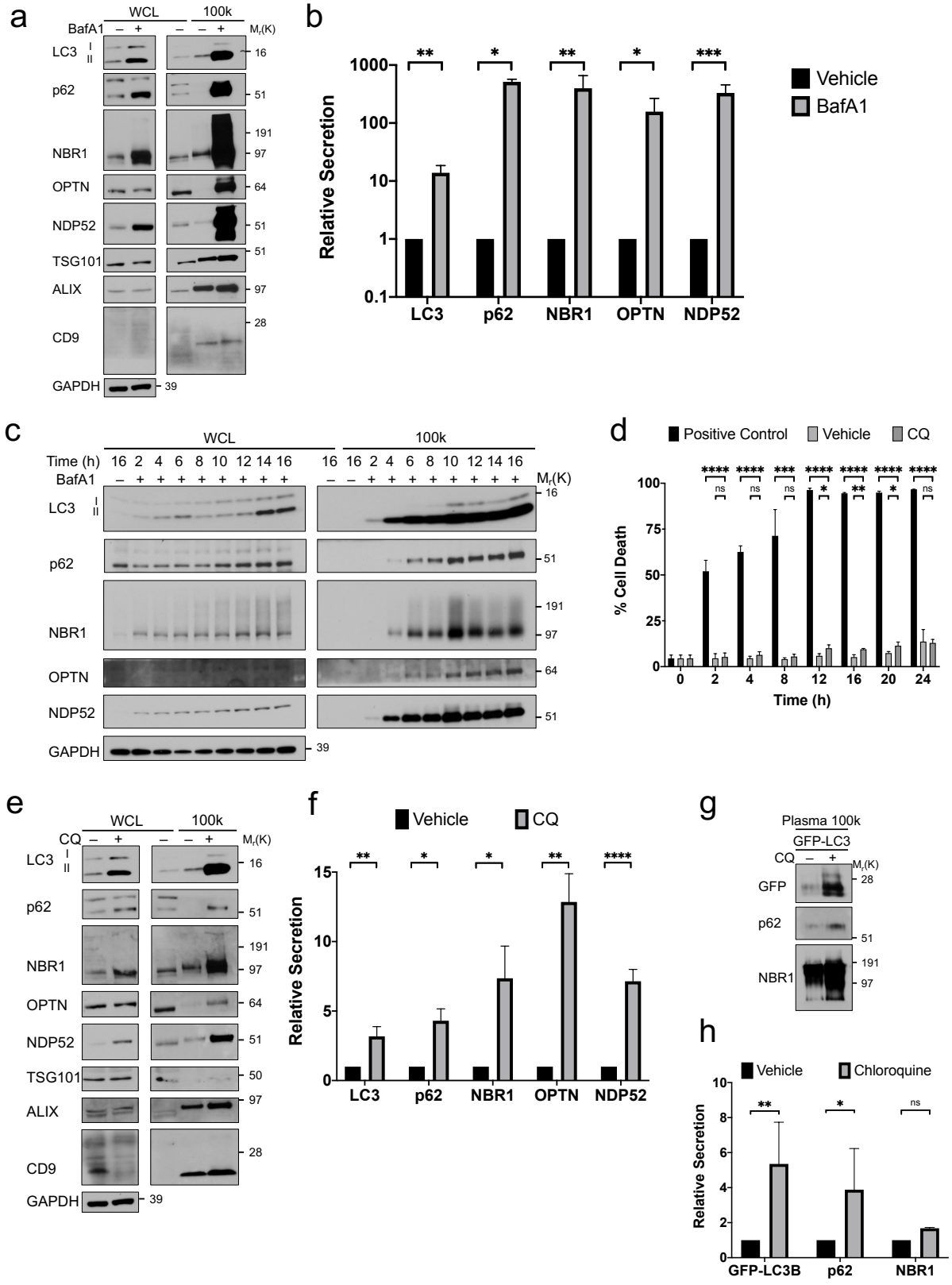

Figure 2.4. Inhibition of endolysosomal acidification promotes secretion of autophagy cargo receptors

(a) Whole cell lysate (WCL) and 100,000 g EV (100k) fractions harvested from wild-type (WT) cells treated with vehicle or 20 nM bafA1 in serum-free media for 16 h were collected, normalized for cell number, and immunoblotted to detect LC3 and indicated autophagy cargo receptors and EV markers. (b) Quantification of autophagy cargo receptor protein levels in 100k from WT bafA1 treated cells relative to vehicle treated (mean ± s.e.; n=3). Statistical significance calculated by unpaired two-tailed t-test (* = p-value < 0.05, ** = p-value < 0.01, *** = p-value < 0.001). (c) WCL and 100k fractions harvested from WT cells treated with vehicle or 20 nM bafA1 in serum-free media for indicated time were collected, normalized for cell number, and immunoblotted to detect LC3 and indicated autophagy cargo receptors. (d) Cell death in WT cells treated with 48 μM digitonin in full media (Positive Control), treated with vehicle in serum-free media (Vehicle), or treated with 25 μM chloroquine (CQ) in serum-free media (25 μM CQ) for indicated time periods quantified using trypan blue staining (mean ± s.e.; n=3). Statistical significance calculated by ordinary one-way analysis of variance followed by Sidak multiple comparisons test for comparison between pairs (n.s. = not significant, * = p-value < 0.05, ** = p-value < 0.01, **** = p-value < 0.0001). (e) WCL and 100k fractions harvested from WT cells treated with vehicle or 25 μM CQ in serum-free media for 24 h were collected, normalized for cell number, and immunoblotted to detect LC3 and indicated autophagy cargo receptors and EV markers. (f) Quantification of LC3 and autophagy cargo receptor protein levels in 100k from WT CQ treated cells relative to vehicle treated (mean ± s.e.; n=3). Statistical significance calculated by unpaired two-tailed t-test (* = p-value < 0.05, ** = p-value < 0.01, **** = p-value < 0.0001). (g) 100k fractions harvested from equivalent volumes of plasma from GFP-LC3 transgenic mice injected with either 60 mg/kg CQ or vehicle for 3 consecutive days were collected and immunoblotted to detect GFP-LC3 and indicated autophagy cargo receptors. (h) Quantification of GFP-LC3 and autophagy cargo receptor protein levels in plasma 100k from CQ treated mice relative to vehicle treated (mean ± s.e.; n=3). Statistical significance calculated by unpaired two-tailed t-test (n.s. = not significant, * = p-value < 0.05, ** = p-value < 0.01).

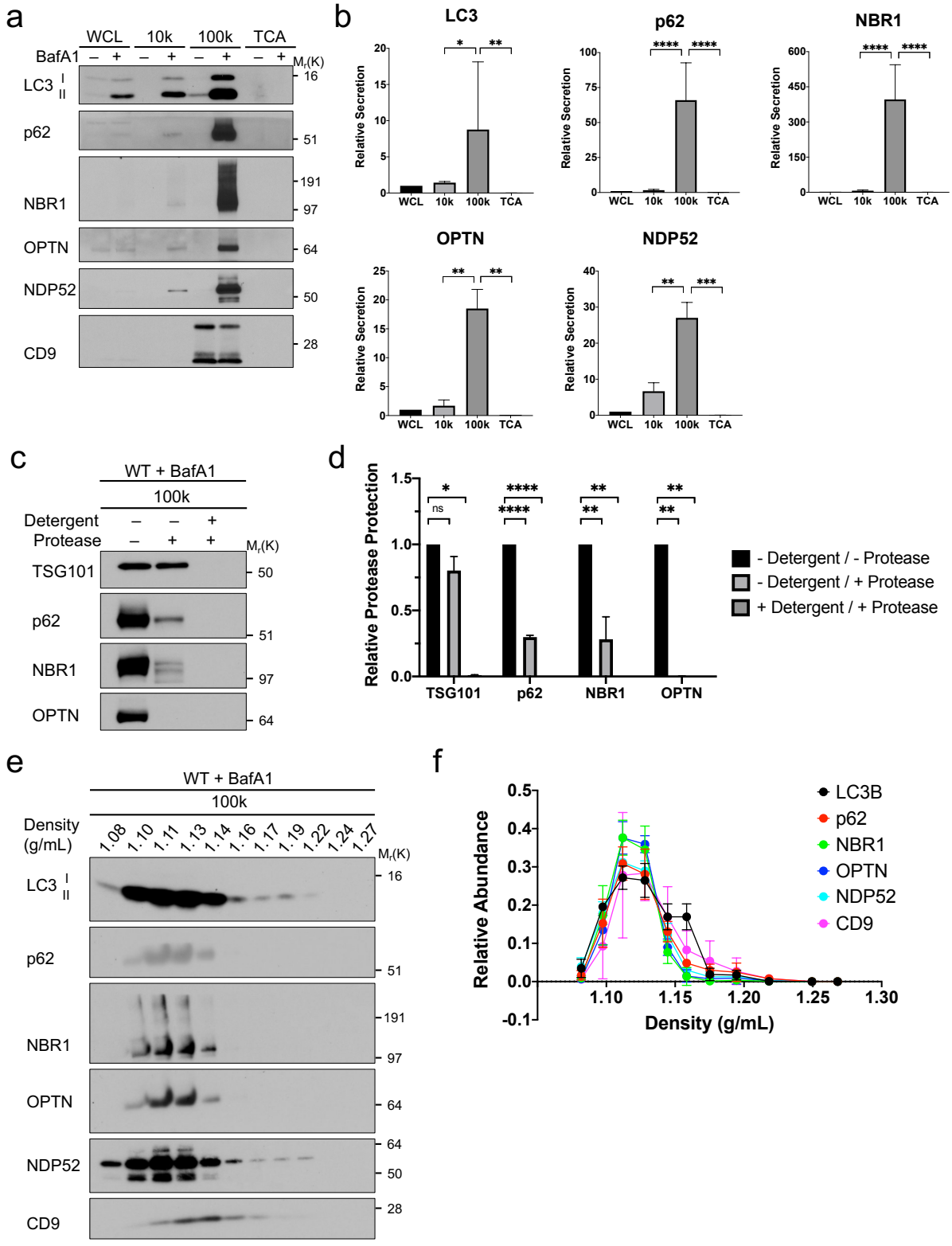

Figure 2.5. Secreted autophagy cargo receptors are EV-associated but not membrane-protected

(a) Whole cell lysate (WCL), 10,000 g EV (10k), 100,000 g EV (100k), and TCA-precipitated soluble protein (TCA) fractions harvested from wild-type (WT) cells treated with vehicle or 20 nM bafA1 in serum-free media for 16 h were collected, normalized for protein concentration, and immunoblotted to detect LC3 and indicated autophagy cargo receptors and EV markers. (b) Quantification of autophagy cargo receptor protein levels in 100k relative to 10k and TCA (mean ± s.e.; n=3). Statistical significance calculated by one-way analysis of variance followed by Sidak multiple comparisons test for comparison between pairs (* = p-value < 0.05, ** = p-value < 0.01, *** = p-value < 0.001, **** = p-value < 0.0001). (c) 100k fractions harvested from WT cells treated with 20 nM bafA1 in serum-free media for 16 h were collected, incubated with 100 ug/mL trypsin (protease) and/or 1% NP-40 (detergent) for 30 min on ice, and immunoblotted to detect TSG101 and indicated autophagy cargo receptors. (d) Quantification of protease protection of TSG101 and autophagy cargo receptors in trypsin and/or protease-treated 100k from WT bafA1 treated cells (mean ± s.e.; n=3). Statistical significance calculated by one-way analysis of variance followed by Dunnett multiple comparisons test for comparison to a control (n.s. = not significant, * = p-value < 0.05, ** = p-value < 0.01, **** = p-value < 0.0001). (e) 100k fractions from WT cells treated with 20 nM bafA1 in serum-free media for 16 h were collected, separated via linear sucrose density gradient ultracentrifugation, fractionated, and immunoblotted to detect LC3, indicated autophagy cargo receptors, and CD9. (f) Quantification of LC3, autophagy cargo receptors, and CD9 protein levels in 100k sucrose density fractions from WT bafA1 treated cells (mean ± s.e.; n=3).

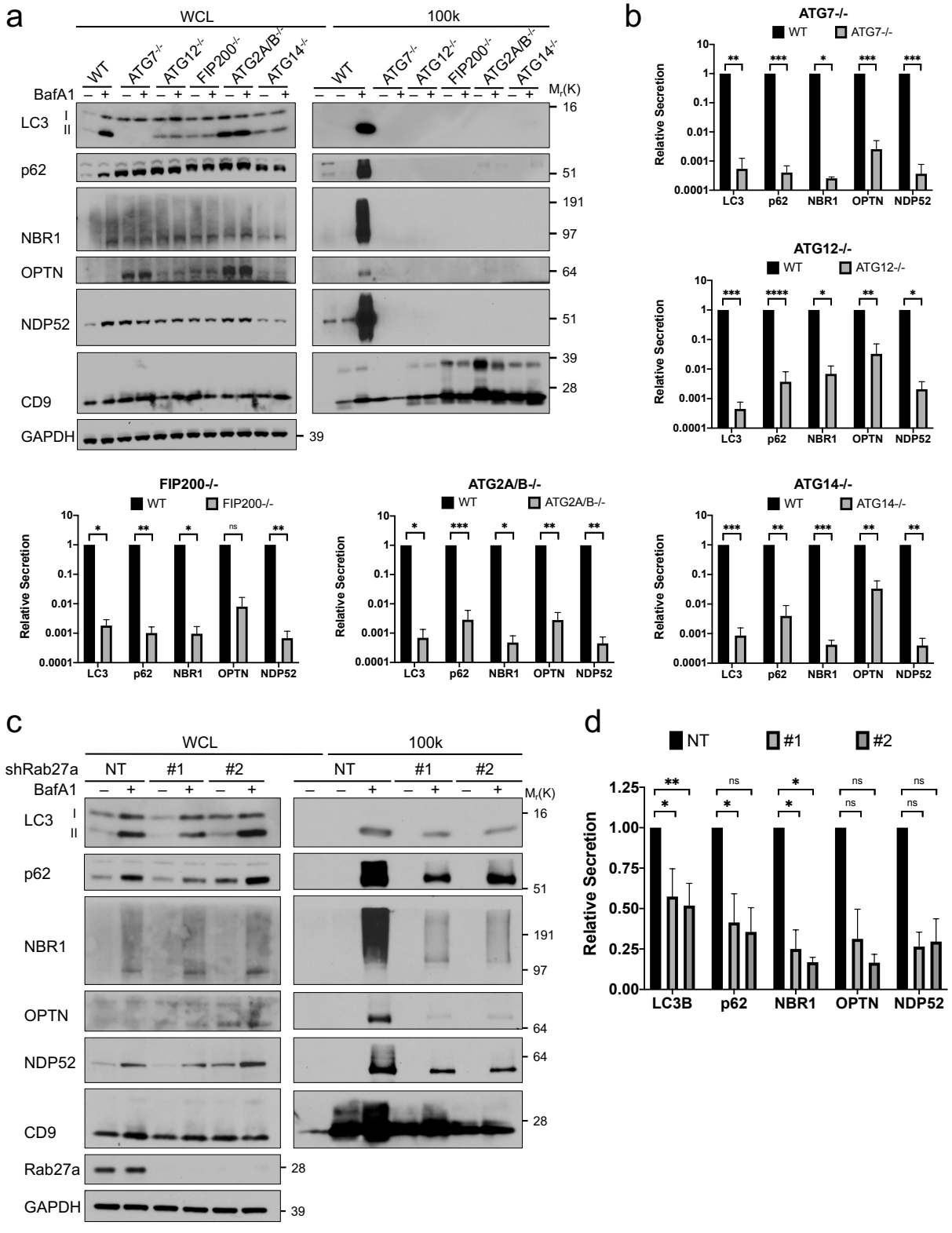

Figure 2.6. ATGs encompassing autophagosome initiation, elongation, and closure and Rab27a are required for secretion of autophagy cargo receptors

(a) Whole cell lysate (WCL) and 100,000 g EV (100k) fractions harvested from wild-type (WT) or indicated ATG -/- cells treated with vehicle or 20 nM bafA1 in serum-free media for 16 h were collected, normalized for protein concentration, and immunoblotted to detect LC3 and indicated autophagy cargo receptors and EV markers. (b) Quantification of autophagy cargo receptor protein levels in 100k from indicated ATG -/- bafA1 treated cells relative to WT bafA1 treated (mean ± s.e.; n=3). Statistical significance calculated by unpaired two-tailed t-test (n.s. = not significant, * = p-value < 0.05, ** = p-value < 0.01, *** = p-value < 0.001, **** = p-value < 0.0001). (c) WCL and 100k fractions harvested from cells stably expressing non-targeting (NT) or Rab27a shRNAs treated with vehicle or 20 nM bafA1 in serum-free media for 16 h were collected, normalized for cell number, and immunoblotted to detect LC3, indicated autophagy cargo receptors, and CD9. (d) Quantification of autophagy cargo receptor protein levels in 100k from Rab27a knockdown cells relative to NT (mean ± s.e.; n=3). Statistical significance calculated by one-way analysis of variance followed by Dunnett multiple comparisons test for comparison to control (n.s. = not significant, * = p-value < 0.05, ** = p-value < 0.01).

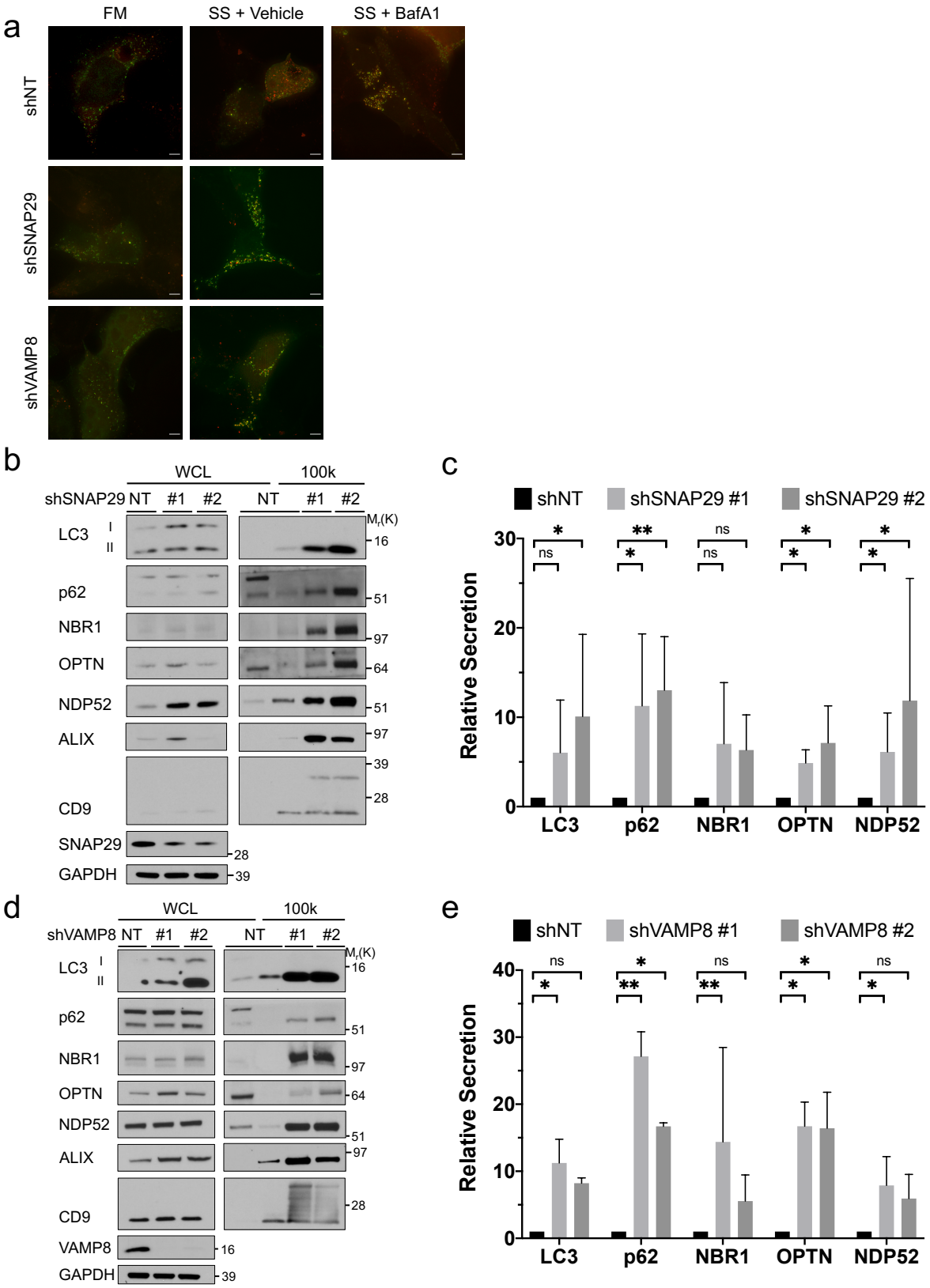

Figure 2.7. Genetic inhibition of autophagosome-lysosome fusion promotes secretion of autophagy cargo receptors

(a) Cells stably expressing non-targeting (NT), SNAP29, or VAMP8 shRNAs transfected with mCherry-GFP-LC3 were grown in full media (FM), treated with vehicle in serum-free media (SS), or treated with 20 nM bafilomycin A1 (bafA1) in serum-free media (BafA1) for 16 h. Scale bar, 5 μm. (b) WCL and 100k fractions harvested from cells stably expressing non-targeting (NT) or SNAP29 shRNAs grown in serum-free media for 24 h were collected, normalized for cell number, and immunoblotted to detect LC3, indicated autophagy cargo receptors, and CD9. (c) Quantification of autophagy cargo receptor protein levels in 100k from SNAP29 knockdown cells relative to NT (mean ± s.e.; n=3). Statistical significance calculated by one-way analysis of variance followed by Dunnett multiple comparisons test for comparison to control (n.s. = not significant, * = p-value < 0.05, ** = p-value < 0.01). (d) WCL and 100k fractions harvested from cells stably expressing non-targeting (NT) or VAMP8 shRNAs grown in serum-free media for 24 h were collected, normalized for cell number, and immunoblotted to detect LC3, indicated autophagy cargo receptors, and CD9. (e) Quantification of autophagy cargo receptor protein levels in 100k from VAMP8 knockdown cells relative to NT (mean ± s.e.; n=3). Statistical significance calculated by one-way analysis of variance followed by Dunnett multiple comparisons test for comparison to control (n.s. = not significant, * = p-value < 0.05, ** = p-value < 0.01).

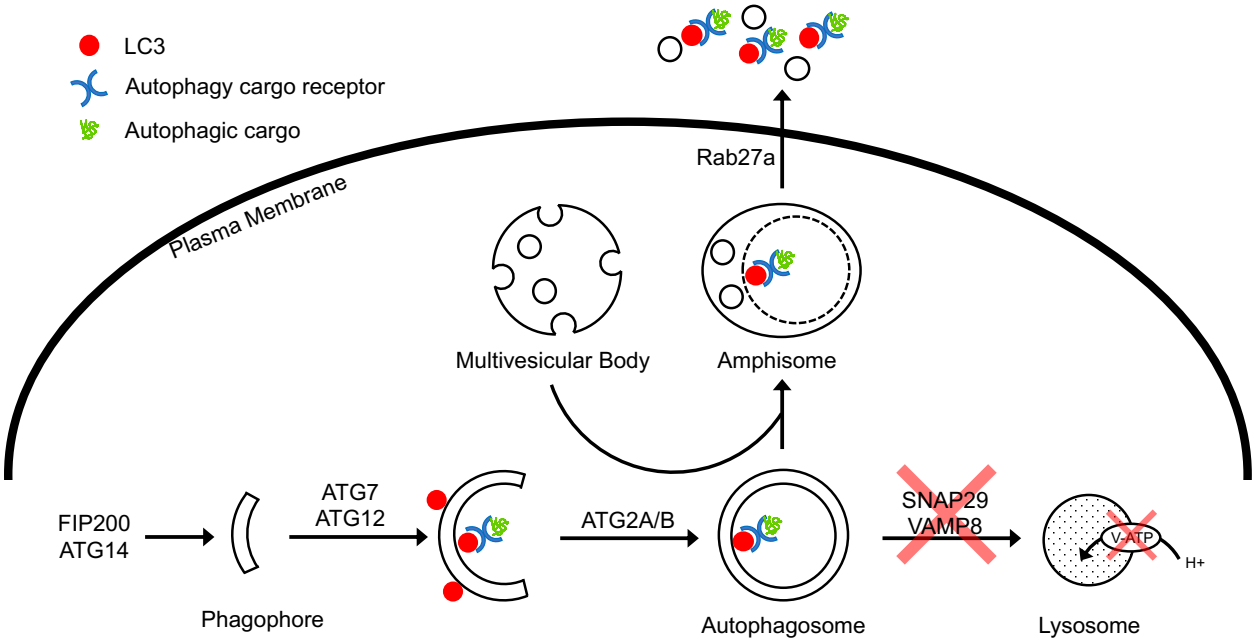

Figure 2.8. Model of secretion
Proposed model for autophagosome formation-dependent and Rab27a-dependent secretion of LC3, autophagy cargo receptors, and autophagic cargo.

METHODS

Cell culture

HEK-293T cells (ATCC, CRL-3216) were cultured in Dulbecco's Modified Eagle Medium (DMEM), high glucose, pyruvate (Gibco 11995040) supplemented with 10% fetal bovine serum (FBS) (Atlas Biologicals F-0500-D), 25 mM HEPES (Teknova H1030), 100 units/mL penicillin and 100 μL/mL streptomycin (Gibco 14140163). All cell lines were tested for mycoplasma contamination (Sigma-Aldrich MP0035).

CRISPR/Cas9 gene-deletion

HEK-293T knockout cell lines were generated by transient transfection of pSpCas9(BB)-2A-Puro (Addgene 48139) encoding U6 driven expression of sgRNAs (Scramble Guide: GCACTACCAGAGCTAACTCA; ATG7 Guide: ACACACTCGAGTCTTTCAAG; ATG12 Guide: CCGTCTTCCGCTGCAGTTTC; ATG14 Guide: CTACTTCGACGGCCGCGACC; FIP200 Guide: AGAGTGTGTACCTACAGTGC). Cells were selected 48-72 hours post-transfection with 1 □g/ml puromycin for 48 h. Polyclonal populations were collected for Surveyor analysis (IDT, 706020) and were sorted into single-cell populations by limiting dilution at 1.5 cells/well per 96-well plate. For DNA analysis, genomic DNA samples were prepared using QuickExtract (Epicentre). The PCR products were column purified and analyzed with Surveyor Mutation Detection Kit (IDT). For genotyping of single-sorted cells, PCR amplified products encompassing the edited region (ATG7 Fwd: TGGGGGACAGTAGAACAGCA, ATG7 Rev: CCTGGATGTCCTCTCCCTGA; ATG12 Fwd: AGCCGGGAACACCAAGTTT, ATG12 Rev: GTGGCAGCCAAGTATCAGGC; ATG14 Fwd: AAAATCCCACGTGACTGGCT, ATG14 Rev: AATGGCAGCAACGGGAAAAC; FIP200

Fwd: ATTCTCTGGCTTGACAGGACAG, FIP200 Rev: AAATACTGAGCGTGCACATTGC) were cloned into pCR™4-TOPO® TA vector using the TOPO-TA cloning kit (Thermo Fisher 450030) and sequence verified. Sequencing is available upon request.

RNA interference

To generate stable knockdowns, cells were transduced with pLKO.1 lentiviral vectors (Sigma-Aldrich) expressing shRNAs targeting SNAP29 (#1 TRCN0000083650; #2 TRCN0000231850), VAMP8 (#1 TRCN0000219911; #2 TRCN0000181123), Rab27a (#1 TRCN0000005296; #2 TRCN0000005297), and non-targeting control (SHC002).

Lentiviral packaging, infection, and selection

Individual lentiviral pLKO.1 expression vectors were packaged by co-transfecting HEK-293T cells with packaging vectors pMDLg/pRRE (Addgene 12251), pMD2.G (Addgene 12259), and pRSV/pRev (Addgene 12253). Virus-containing conditioned media was collected 3 days after transfection and filtered through 0.45 μm. Virus-containing media was then diluted 1:4 in DMEM media supplemented with 8 μg/mL polybrene. The viral transduction mix was incubated with HEK-293T cells for 72 h, then cells were selected with 1 μg/mL puromycin (Sigma-Aldrich P7255) for 2 days.

Antibodies

The following antibodies were used for immunoblotting: rabbit anti-ATG14 (MBL, PD026; 1:1,000), rabbit anti-LAMP1 (Cell Signaling, 9091; 1:1,000), rabbit anti-Rab7a (Cell Signaling, 9367; 1:1,000), rabbit anti-Rab5a (Cell Signaling, 3547; 1:1,000), mouse anti-GM130 (BD

Biosciences, 610823; 1:1,000), rabbit anti-CYC1 (Novus Biologicals, NBP1-86872; 1:1,000), mouse anti-NUP62 (BD Biosciences, 610497; 1:1,000), mouse anti-GAPDH (Millipore, MAB374; 1:10,000), rabbit anti-LC3 (Millipore, ABC232; 1:1,000), guinea pig anti-p62/SQSTM1 (Progen, GP62-C; 1:1,000), rabbit anti-p62/SQSTM1 (Cell Signaling, 5114; 1:1,000), mouse anti-NBR1 (Santa Cruz Biotechnology, sc-130380; 1:500), rabbit anti-OPTN (Abcam, ab23666; 1:1,000), mouse anti-NDP52/CALCOCO2 (Abnova, H00010241-B01P; 1:1,000), mouse anti-TSG101 (BD Biosciences, 612696; 1:1,000), mouse anti-ALIX (Cell Signaling, 2171; 1:1,000), mouse anti-CD9 (Sigma-Aldrich, CBL162; 1:1,000), mouse anti-GFP (Santa Cruz sc-9996), rabbit anti-Rab27a (Cell Signaling, 69295; 1:1,000), rabbit anti-SNAP29 (Abcam, ab138500; 1:1,000), rabbit anti-VAMP8 (Abcam, ab76021; 1:1,000), Peroxidase-AffiniPure Donkey Anti-Rabbit IgG (H+L) (Jackson, 711-035-152; 1:5,000), Peroxidase-AffiniPure Donkey Anti-Guinea Pig IgG (H+L) (Jackson, 706-035-148; 1:5,000), Peroxidase-AffiniPure Donkey Anti-Goat IgG (H+L) (Jackson, 705-035-147; 1:5,000), and Peroxidase-AffiniPure Donkey Anti-Mouse IgG (H+L) (Jackson, 715-035-150; 1:5,000).

Immunoblotting

For whole cell lysate (WCL), cells were lysed in RIPA buffer (25 mM Tris-HCl pH 8.0, 150 mM NaCl, 1% NP-40, 1% sodium deoxycholate, 0.1% SDS) supplemented with 10 mM NaF, 10 mM β-glycerophosphate, 1 mM Na_3VO_4, 10 nM calcyulin A, 0.5 mM phenylmethyl sulphonyl fluoride, 0.1 mM E-64-D, 10 μg/mL pepstatin A, and protease inhibitor cocktail. Lysates were cleared by centrifugation at 15,000 g for 10 min at 4°C. For EV lysate, pelleted EVs were resuspended in urea buffer (50 mM Tris-HCl, pH 8.0, 8 M urea, 2% SDS, 10 mM NaF, 5 mM EDTA). WCL and EV lysates were quantified by BCA assay (Thermo Fisher 23225), mixed

with sample buffer, resolved by SDS-PAGE, and transferred to polyvinylidene fluoride membrane. Membranes were then blocked in 5% milk in PBS with 0.1% Tween 20 (PBST), incubated in primary antibody overnight at 4°C in blocking buffer, washed with PBST, incubated in HRP-conjugated secondary antibodies for 1 h at room temperature in blocking buffer, washed with PBST, and visualized by enhanced chemiluminescence (Thermo Fisher 32106) on film. Immunoblots were quantified by densitometry using Fiji (ImageJ v.2.0.0-rc-69/1.52p).

Fluorescence microscopy

For fluorescence of mCherry-GFP-LC3, cells were transiently transfected with mCherry-GFP-LC3 at 70% confluency using Lipofectamine 2000 (Thermo Fisher 11668019). After 6h, transfected cells were seeded onto coverslips coated with 10 μg/mL fibronectin and incubated for 24 h before treatment with vehicle or 20 nM bafA1 in serum-free DMEM for 16 h. Cells were then fixed with 4% PFA in PBS for 15 min at room temperature, washed with PBS, and mounted onto slides with Prolong Gold Antifade with DAPI (Thermo Fisher P36935). Cells were visualized using a DeltaVision microscope (Applied Precision Ltd.) fitted with a 60Å~, 1.4-NA objective and CoolSnap HQ camera (Photometrics). Images were acquired using softWoRx software (Applied Precision Ltd.) and prepared in Fiji and Adobe Photoshop.

Cell viability assay

To quantify cell viability, cells were seeded in 12-well plates and after 24 h, were treated with 48 μM digitonin (positive control for cell death) in complete DMEM, vehicle (negative control) in serum-free DMEM, or 20 nM bafA1 or 25 μM CQ in serum-free DMEM. Cells were collected at the indicated timepoints and stained with 0.4% trypan blue (Thermo Scientific T10282). Live

and dead cells were then enumerated using the Countess II Automated Cell Counter (Thermo Scientific AMQAX1000).

Extracellular vesicle preparation and characterization

EVs were isolated according to standard differential centrifugation protocol as described previously[68]. Briefly, HEK-239T cells were seeded in 15 cm tissue culture dishes and, when confluent, incubated with serum-free DMEM +/- treatment (20 nM bafA1, 25 μM CQ) for 16 or 24h. Conditioned media was then collected and serially centrifuged: 200 g for 10 min at 4ºC to pellet cells, 2,000 g for 10 min at 4ºC to pellet cellular debris and apoptotic bodies, 10,000 g for 30 min at 4ºC in an ultracentrifuge to pellet large EVs, and 110,000 g for 70 min or 3h at 4ºC in an ultracentrifuge to pellet small EVs. The 110,000 g pellet was then gently resuspended in 1 mL PBS by pipetting, diluted in 12 mL PBS, and ultracentrifuged at 110,000 g for 70 min at 4ºC. The final EV pellets were resuspended in urea lysis buffer for immunoblotting analysis, 10% sucrose for sucrose density gradient analysis, or PBS for protease protection analysis. For analysis of secreted soluble protein, the supernatant from the first 110,000 g spin was collected and precipitated by addition of 15% trichloroacetic acid (TCA), then incubated for 1 h on ice before centrifugation at 180,000 g for 2h at 4ºC. The 180,000 g pellet was then resuspended in 10 mL ice-cold 100% acetone, centrifuged at 180,000 g for 1 h at 4ºC, and finally resuspended in urea lysis buffer. For comparison of EVs between experimental conditions *in vitro*, EV quantification or EV protein quantification were corrected as indicated in figure legends based on total cell number or WCL protein quantification to correct for cell seeding differences between conditions.

Sucrose density gradient separation was used to analyze co-fractionation between LC3, ATG cargo receptors, and canonical EV markers. 10% and 60% sucrose solutions in PBS were used to prepare continuous 10-60% sucrose gradients on a gradient station (Biocomp Instruments 153). EV pellets were generated by differential centrifugation as described previously, then resuspended in 100 μL 10% sucrose solution, gently layered on top of the 10-60% gradient, and ultracentrifuged at 210,000 g for 18 h at 4°C. After ultracentrifugation, 1 mL fractions of the gradient were carefully top-unloaded, weighed, and diluted in 12 mL PBS. The diluted sucrose gradient fractions were ultracentrifuged at 110,000 g for 70 min at 4°C and pellets were resuspended in urea lysis buffer for immunoblotting analysis.

Protease protection analysis was used to determine membrane protection of secreted LC3 and ATG cargo receptors. EV pellets were generated by differential centrifugation as described previously, resuspended in 60 μL PBS, and divided equally into 3 fractions for resuspension in PBS, 100 μg/mL trypsin in PBS, or 1% NP-40 and 100 μg/mL trypsin in PBS. After incubation and occasional mixing for 30 min at 4°C, protease reactions were stopped with the addition of 10 μL protease inhibitor cocktail and 2x sample buffer before immunoblotting analysis.

Nanoparticle tracking analysis (NTA) technology was used to determine EV concentration and size. Conditioned media clarified of cell debris and large EVs by 0.22 μm filter were normalized by cell number, then loaded on a nanoparticle analyzer (Malvern Panalytical NanoSight NS300) and analyzed using NTA software (NTA 3.3 Dev Build 3.3.104). Camera level was set at 15 for all recordings. Camera focus was adjusted to make the particles appear as individual dots with surrounding refractory rings. Three 30 s videos were recorded for each sample with a delay of 5 s between each recording.

Mass spectrometry of extracellular vesicle proteins

WT and *ATG7*-/- HEK293T cells were treated with 20nM BafA1 or vehicle in serum-free media for 16 h. After 16 h, conditioned media was collected and EVs were isolated using the differential centrifugation protocol outlined previously. Pelleted EVs were lysed in 800 μL RIPA buffer (25 mM Tris-HCl pH 8.0, 150 mM NaCl, 1% NP-40, 1% sodium deoxycholate, 0.1% SDS) supplemented with 2% SDS, then sonicated with a probe sonicator at amplitude 8 for 10 pulses of 10 s each. Samples were then diluted in 4 mL ice-cold 100% acetone and incubated at -20°C overnight. Samples were spun in an ultracentrifuge at 200,000 g for 18 h at 4°C, the acetone was decanted, and the samples air dried for 1 h at 25°C before being stored at -80°C until further processing.

Three biological replicates of precipitated EVs from WT and *ATG7*-/- bafA1-treated cells were resuspended in 30 μL 6 M guanidinium-chloride, 100 mM Tris pH 8.0, 10 mM TCEP, 40 mM 2-chloroacetamide. EV proteins were denatured for 1 h at 37°C, then quantified with 660nm Protein Assay Reagent (Thermo Scientific 22660). Samples were then diluted six-fold in 150 μL 100 mM Tris pH 8.0. 125-150 μg of protein for each sample was trypsinized with 15 μg trypsin (Thermo Scientific 90057) in an orbital shaker at 250 rpm, 37°C for 20 h. Trypsin digestion was then stopped by adding 10% trifluoracetic acid (TFA) to a final concentration of 0.5% TFA. Samples were desalted with SOLA solid phase extraction cartridges (Thermo Scientific 60109). Briefly, columns were washed with 500 μL 100% acetonitrile (ACN), then equilibrated with 500 μL 0.1% TFA twice before adding sample. Samples were washed with 500 μL 0.1% TFA three times, then 500 μL 0.1% formic acid (FA), 2% ACN, and eluted with 450 μL 0.1% FA, 50% ACN. Samples were dried by speed-vac, then resuspended in 10 μL 50 mM HEPES pH 8.5 and quantified by Pierce Quantitative Colorimetric Peptide Assay (Thermo Scientific 23275).

For Tandem Mass Tag (TMT) labeling, 800 μg of TMT^{10}-126, 127N, 128C, 129N, 130C, and 131 (Thermo Scientific 90110) was reconstituted with 41 μL 100% anhydrous ACN. 15 μg of peptides from each replicate were individually combined with 7.69 μL (150 μg) of the TMT isobaric tags. Samples were incubated at 25°C for 1 h before quenching the reaction with 8 μL 5% hydroxylamine for 15 min. After labeling, the six individually labeled samples were pooled, dried by speed-vac, and then resuspended in 300 μL 0.1% TFA. The pooled samples were then fractionated into 8 fractions using Pierce High pH Reversed-Phase Peptide Fractionation Kit (Thermo Scientific 84868), then dried by speed-vac. The fractions were then resuspended in 0.1% FA, 2% ACN before LC-MS/MS analysis.

For LC-MS/MS analysis, 1 μg TMT-labeled peptide per fraction was analyzed on a 15 cm C18 analytical column, in-line with a Q-Exactive Plus mass spectrometer. The peptides were separated on a multi-slope, 100 min gradient (6.4% - 27.2% ACN with 0.1% FA for 80 min at 0.2 μL/min, then 27.2% - 40% ACN with 0.09% FA for 15 min at 0.3 μL/min, then 40% - 56% ACN with 0.09% FA for 5 min at 0.3 μL/min, and then washed for 3 min). Data dependent acquisition with MS1 resolution of 70,000, top15 method, and HCD normalized collision energy of 32 was used, with MS2 resolution of 35,000 and an isolation window of 0.7 m/z. Dynamic exclusion was activated for 30 s after initial parent ion selection.

Eight injections of the different fractions of TMT-labeled EV peptides were analyzed together via MaxQuant (v1.6.0.16). Search parameters for peptide search tolerance was 4.5 ppm, centroid match tolerance was 8 ppm, and 2 missed tryptic cleavages were permitted. Constant modification of carbamidomethylation of cysteines and variable modifications of N-terminal acetylation, methionine oxidation, and Ser/Thr/Tyr phosphorylation were allowed. Peptide spectrum match FDR and protein FDR were set at 1%. “Match between runs” was enabled to

increase peptide identification. Type was set to "Reporter ion MS2," and the six labels used in sample preparation were selected. The resulting quantifications were then median normalized for each channel, and statistical analysis (two-sample *t*-test) was applied in R with a statistical significance threshold of $p < 0.05$.

Bioinformatic analyses

For mass spectrometry, the top eight proteins with the highest connectivity to candidates statistically enriched in EVs from wild-type cells treated with bafA1 versus EVs from *ATG7*-/- cells treated with bafA1 (p-value < 0.05; $\log_2$ WT/*ATG7*-/- > 0.585; n=3) were identified using the protein-protein interaction (PPI) hub protein tool in the Enrichr gene set enrichment analysis web server[69,70] and plotted according to their -$\log_{10}$ adjusted p-values. GO analysis (database released 2019-12-09) of the secretome was performed with PANTHER Overrepresentation Test (released 2019-07-11)[71] and the top ten terms for biological process and cellular component were plotted according to their -$\log_{10}$ false discovery rate. The overlaps between the defined secretome and the ATG8 interactome[28], ATG7-dependent secretome[29], LDELS secretome[29], CQ autophagosome proteome[56], and BafA1 autophagosome proteome[57] were performed using Biovenn[72].

In vivo extracellular vesicle isolation from mice

All experimental procedures and treatments were conducted in compliance with UCSF Institutional Animal Care and Use Committee (IACUC) guidelines under an approved animal protocol (#AN170608). C57BL/6JJc1 homozygous transgenic mice expressing GFP-LC3B[73,74] (Riken Bioresource Center No. 00806) received either 60 mg/kg CQ or vehicle via

intraperitoneal injection for 3 consecutive days. 6 h after final CQ injection, whole blood was collected in heparin-coated capillary tubes (Sarstedt CB 300 Lithium Heparin) and centrifuged at 2,000 g for 5 min at room temperature. The plasma phase was collected and 1 mL was pooled (from 3-4 mice per condition), diluted in 10 mL PBS, clarified by 0.22 μm filter, and ultracentrifuged at 110,000 g for 3 h at 4°C. The pellet was resuspended in 10 mL PBS, ultracentrifuged at 110,000 g for 70 min at 4°C, and resuspended in urea buffer for immunoblotting analysis. For comparison of EVs between experimental groups *in vivo*, samples were normalized by collection from equivalent volumes of plasma from experimental groups.

Statistical analyses

Statistical analysis was performed using GraphPad Prism 8 (v.8.3.0). Experimental groups were compared using unpaired Student's t-test for pairwise comparison, one-way analysis of variance followed by Dunnett multiple comparisons test for comparison to a control column, or one-way analysis of variance followed by Sidak multiple comparisons test for comparison between pairs of columns.

CHAPTER 3: Implications of autophagy and secretion in neurodegenerative disease

DISCUSSION

In this study, we identify a new relationship between degradative autophagy and secretory autophagy, in which failure of lysosomal fusion and degradation promotes secretion of autophagic material. Utilizing a proteomic approach, we determined that impaired endolysosomal acidification results in ATG7-dependent secretion of LC3 and autophagy cargo receptors, normally subject to degradation. We characterized the secreted material as EV-associated but not membrane-protected, distinct from the LDELS secreted material. Further analysis revealed this secretory event requires complete autophagosome formation and Rab27a, implicated in MVB fusion with the plasma membrane, suggesting the autophagosome-MVB hybrid organelle, the amphisome, is secreted when intracellular degradation is impaired.

While previous studies have demonstrated the connection between the autophagy and secretory pathways, there has been a lack of convincing evidence that the autophagosome structure itself, rather than just single ATG proteins, can interchange between degradative and secretory pathways. This study demonstrates that in the absence of fusion with the lysosome for degradation, the autophagosome can be redirected for secretion. As autophagosomes mediate the specific degradation of pathogenic or damaged cytoplasmic material, their secretion may both improve cell autonomous homeostasis by removing such material and impair non-cell autonomous homeostasis by spreading it to healthy neighboring cells. This occurrence would be most relevant in the context of neurodegenerative diseases, in which cells exhibit endo-lysosomal dysfunction, failure of autophagosome degradation, and secretion of pathogenic protein aggregates.

AUTOPHAGY AND NEURODEGENERATIVE DISEASE

Many neurodegenerative diseases are defined by the accumulation of misfolded proteins, including Alzheimer's and Parkinson's diseases. Given the role of autophagy in maintain cellular homeostasis by degrading cellular components like protein aggregates, it is logical that autophagy may play a role in maintaining viability and health of neurons. This is even more critical considering that neurons are post-mitotic and cannot reduce their intracellular load of misfolded proteins via cell division[75]. Neural deletion of *Atg5* and *Atg7* results in motor function defects and presence of ubiquitinated protein aggregates in neurons, evidence that loss of autophagy leads to neurodegenerative disease[76,77]. There are likely two causes of autophagy-related neurodegenerative disease: aging and inherited mutations that impact the autophagy-endolysosome pathway. Overexpression of *Atg5* in mice not only activates autophagy, but improves lifespan and promotes anti-aging phenotypes[78]. Meanwhile, mutations that impair various steps of the autophagic pathway result in neurodegenerative disease[51]. The two most common neurodegenerative diseases, Alzheimer's and Parkinson's, both feature impairments in the final step of autophagy: fusion with the lysosome and degradation of autophagic cargo.

Alzheimer's Disease

Alzheimer's is the most common neurodegenerative disease and is characterized by intracellular accumulation of hyperphosphorylated tau in neurofibrillary tangles and extracellular accumulation of beta-amyloid (Aβ) plaques associated with dystrophic neurites[79]. Aβ is generated by cleavage of amyloid protein precrusors (APP) though cleavage by β and γ-secretase. Cleavage can result in multiple peptide products including Aβ-40 and Aβ-42, but Aβ-42 is the most pathogenic, as it is more hydrophobic and forms insoluble aggregates (plaques)[80].

The ratio of Aβ-42/40 is critical for pathogenesis, as it affects the morphology and stability of extracellular plaques[81]. Autophagosomes are enriched in APP and Aβ and induction of autophagy by starvation or rapamycin induces Aβ production, suggesting Aβ is generated inside of autophagosomes[82,83]. These Aβ peptides can be routed to MVBs and subsequently secreted in association with exosomes, and exosomal proteins like Alix have been identified in plaques in Alzheimer's patient brains[84]. In addition, the exogenous addition of Aβ aggregates can induce further Aβ aggregation, suggesting a self-perpetuating prion-like spread of pathological protein that may underlie the pathogenesis of this disease[85]. Alzheimer's patient brains reveal an accumulation of autophagosomes, MVBs, and autolysosomes in dystrophic neurites[86]. Furthermore, inhibition of lysosomal acidification phenocopies Alzheimer's, suggesting a failure of autophagosome-lysosome fusion leads to the disease[87]. Mutations in presenilin-1 (PS1) are the most common cause of early-onset familial Alzheimer's disease; PS1 knockout cells exhibit increased lysosomal pH and accumulated autophagosomes. PS1 is required for delivery of v-ATPase subunit V0a1 from the endoplasmic reticulum to lysosomes, and thereby sufficient v-ATPase activity[88,89]. PS1 mutations that cause early-onset FAD result in reduced protein turnover, high LC3-II/LC3-I ratios, a block in autophagic flux, and impaired acidification of lysosomes[88]. Furthermore, pharmacological inhibition of v-ATPase function induces a similar autophagy phenotype to loss of PS1[89]. In addition to their role in lysosomal function, PS1 mutations augment extracellular secretion of Aβ-42 *in vitro* and *in vivo*[90].

Parkinson's Disease

The second most common neurodegenerative disease, Parkinson's, is caused by the degeneration of dopaminergic neurons in the substantia nigra. Both sporadic and familial cases of the disease

are pathologically characterized by large protein aggregates or inclusions (referred to as Lewy bodies) in neurons. α-synuclein (α-syn) is the predominant protein in Lewy bodies, and two missense mutations (A53T and A30P) result in early-onset Parkinson's disease[91]. Furthermore, overexpression of wild-type *α-syn* results in Lewy body pathology, suggesting the accumulation of α-syn aggregates causes Parkinson's[92]. Similar to Aβ in Alzheimer's disease, exogenous addition of mutant α-syn can speed endogenous α-syn aggregation in recipient brains[93–95]. Intriguingly, α-syn is secreted in association with exosomes, and treatment of neuronal cells with the conditioned media results in cell death, indicating that extracellular release and non-cell autonomous uptake of α-syn would further amplify disease[96]. While soluble α-syn is degraded by autophagy[97], aggregates are not effectively degraded. α-syn aggregates co-localize with autophagosomes, yet those structures fail to fuse with lysosomes[98]. In addition, cells treated with bafA1 to block autophagosome degradation display accumulation of α-syn aggregates[97]. Although whether α-syn affects v-ATPase activity is unclear, its overexpression results in lysosomal de-acidification[99]. Several other mutations are linked to familial Parkinson's disease, including mutations of ATP13A2 and LRRK2, which both cause accumulation of α-syn. While the function of ATP13A2, a lysosomal P-type ATPase, is still unknown, it has been suggested to protect against alpha-synuclein misfolding[100]. Furthermore, mutations in ATP13A2 lead to lysosomal deficiency, including impaired acidification, decreased proteolysis by lysosomal enzymes, reduced degradation of substrates, and clearance of autophagosomes[101]. Mutations in LRRK2 are the most frequent cause of familial Parkinson's disease, and two unique mutations affecting kinase activity, G2019S and R1441C, both result in impaired lysosomal function by reduced pH and impaired autophagosome degradation. While the direct effect of the G2019S mutation is unknown[102], R1441C blocks LRRK2 interaction with v-ATPase subunit a1, resulting

in its mislocalization and the deacidification of the lysosome[103]. Ultimately, these studies indicate that both sporadic and inherited Parkinson's disease feature impaired lysosomal acidification, thereby blocking degradation of autophagosomes and their cargo.

Therefore, two distinct neurodegenerative diseases exhibit several shared features regarding autophagy and pathological protein aggregates. Alzheimer's and Parkinson's diseases are driven by protein aggregates (Aβ and α-syn, respectively), which are subject to both autophagic degradation and extracellular secretion. Intriguingly, Aβ and α-syn are secreted in association with exosomes, but have not been demonstrated to be localized within the exosomal lumen[84,96]. Finally, familial mutations that drive the diseases feature impaired lysosomal acidification and autophagosome-lysosome fusion, resulting in an accumulation of autophagosomes inside of the cell. These cellular events are strikingly similar to the extracellular release of autophagy cargo receptors, and should be further examined to determine if secretory autophagy may be involved.

IMPLICATIONS FOR SECRETORY AUTOPHAGY IN NEURODEGENERATIVE DISEASE

While autophagy has been implicated in many neurodegenerative diseases as a means of degradation of pathogenic protein aggregates, few studies have explored the role of secretory autophagy in these diseases. Since protein aggregates have been demonstrated to transfer from one neuron to another, could there be a mechanism by which neurons overwhelmed with material to be degraded can instead shunt it toward secretion? For example, *C. elegans* neurons can dispose of protein aggregates via large extracellular vesicles (4 μm in diameter) called exophers in response to proteotoxic stress, such as the inhibition of autophagy or the

overexpression of Aβ-42[104]. Secretory autophagy could enable neurons to selectively discard protein aggregates destined for degradation when canonical autophagy is impaired. Several studies have begun to explore the role of ATGs in secretion of Aβ and α-syn.

While autophagy has been implicated in the degradation of APP and Aβ, it is unclear if autophagy is required for routing of Aβ to MVBs prior to its secretion in association with exosomes. APP transgenic mice with conditional neural knockout of *Atg7* have both increased intracellular accumulation of Aβ and decreased extracellular Aβ plaque burden. In *Atg7* knockout neurons, Aβ accumulates in the Golgi, but is not present in MVBs[105]. Furthermore, loss of ATG or pharmacological inhibition of autophagosome formation reduces Aβ extracellular release and impairs memory in mice[106]. Together, this data indicates that ATG7 is critical for Aβ secretion, potentially by incorporation of Aβ into an autophagosome that fuses with the MVB prior to extracellular release. Further research into Aβ secretion is necessary to determine if this event is dependent on other ATGs, indicating a role for the autophagosome itself.

In addition, three studies have investigated the role of autophagy in exosome-associated secretion of α-syn. Overexpression of α-syn in neuroblastoma or neuroglioma cell lines increases the release of α-syn, which co-fractionate with exosomal markers. Secreted α-syn is not protected from protease treatment, indicating it does not reside within the lumen of EVs[107,108]. Furthermore autophagic activity impacts the secretion of α-syn, as secretion is amplified by bafA1 or CQ treatment and reduced by rapamycin treatment[107–109]. Ultrastructural analysis of bafA1-treated cells reveals amphisome-like compartments with nondegraded cytoplasmic cargo as well as small ILVs, suggesting the pathway by which α-syn can be exosome-associated yet not internalized. Intriguingly, cerebral spinal fluid (CSF) from Parkinson's patients contains LC3 and p62 in fractions positive for exosomal markers. Finally,

human α-syn from CSF exosome fractions can be internalized by mouse neurons, as it colocalizes with mouse endosomal markers in the brain and induces endogenous α-syn aggregation[109]. In summary, inhibition of autophagy-lysosome fusion leads to the presence of amphisome structures as well as increased secretion of exosome-associated α-syn, which can be internalized by neighboring cells. Additional questions to address include if α-syn secretion is dependent upon interaction with autophagy cargo receptors, and if these proteins can also be transmitted between cells.

In this work, we identify a novel form of secretory autophagy by which autophagosomes and their protein cargo are redirected to secretion when lysosomal fusion and degradation is blocked. Questions prompted by this finding include what is the fate of this secreted material and how this event impacts non-cell autonomous homeostasis. Is this pathway a mechanism by which diseased cells incapable of autophagic degradation can release harmful material for degradation by competent cells, spread pathogenic protein aggregates to neighboring cells, or both? Furthermore, could medicine utilize this secretory event as a blood biomarker for early diagnosis of diseases in which lysosomal degradation is impaired? Future studies should address these questions in the context of neurodegenerative disease.

REFERENCES

1. Stolz, A., Ernst, A. & Dikic, I. Cargo recognition and trafficking in selective autophagy. *Nat. Cell Biol.* **16**, 495–501 (2014).
2. Russell, R. C. *et al.* ULK1 induces autophagy by phosphorylating Beclin-1 and activating VPS34 lipid kinase. *Nat. Cell Biol.* **15**, 741–750 (2013).
3. Ichimura, Y. *et al.* A ubiquitin-like system mediates protein lipidation. *Nature* **408**, 488–492 (2000).
4. Johansen, T. & Lamark, T. Selective autophagy mediated by autophagic adapter proteins. *Autophagy* **7**, 279–296 (2011).
5. Bjørkøy, G. *et al.* p62/SQSTM1 forms protein aggregates degraded by autophagy and has a protective effect on huntingtin-induced cell death. *J. Cell Biol.* **171**, 603–614 (2005).
6. Kirkin, V. *et al.* A Role for NBR1 in Autophagosomal Degradation of Ubiquitinated Substrates. *Mol. Cell* **33**, 505–516 (2009).
7. Wild, P. *et al.* Phosphorylation of the Autophagy Receptor Optineurin Restricts Salmonella Growth. *Science (80-.).* **333**, 228–233 (2011).
8. Thurston, T. L. M. The tbk1 adaptor and autophagy receptor ndp52 restricts the proliferation of ubiquitin-coated bacteria. *Nat. Immunol.* **10**, 1215–1222 (2009).
9. Birgisdottir, B. Å., Lamark, T. & Johansen, T. The LIR motif – crucial for selective autophagy. *J. Cell Sci.* **126**, 3237–3247 (2013).
10. Velikkakath, A. K., Nishimura, T., Oita, E., Ishihara, N. & Mizushima, N. Mammalian Atg2 proteins are essential for autophagosome formation and important for regulation of size and distribution of lipid droplets. *Mol Biol Cell* **23**, 896–909 (2012).
11. Jahn, R. & Scheller, R. H. SNAREs — engines for membrane fusion. *Nat. Rev. Mol. Cell*

Biol. **7**, 631–643 (2006).

12. Itakura, E., Kishi-Itakura, C. & Mizushima, N. The hairpin-type tail-anchored SNARE syntaxin 17 targets to autophagosomes for fusion with endosomes/lysosomes. *Cell* **151**, 1256–1269 (2012).
13. Matsui, T. *et al.* Autophagosomal YKT6 is required for fusion with lysosomes independently of syntaxin 17. *J. Cell Biol.* **217**, 2633–2645
14. Rabouille, C. Pathways of Unconventional Protein Secretion. *Trends Cell Biol.* **xx**, 1–11 (2016).
15. Duran, J. M., Anjard, C., Stefan, C., Loomis, W. F. & Malhotra, V. Unconventional secretion of Acb1 is mediated by autophagosomes. *J. Cell Biol.* **188**, 527–536 (2010).
16. Manjithaya, R., Anjard, C., Loomis, W. F. & Subramani, S. Unconventional secretion of Pichia pastoris Acb1 is dependent on GRASP protein, peroxisomal functions, and autophagosome formation. *J. Cell Biol.* **188**, 537–546 (2010).
17. Andrei, C. *et al.* The secretory route of the leaderless protein interleukin 1β involves exocytosis of endolysosome-related vesicles. *Mol. Biol. Cell* **10**, 1463–1475 (1999).
18. Dupont, N. *et al.* Autophagy-based unconventional secretory pathway for extracellular delivery of IL-1beta. *Embo J* **30**, 4701–4711 (2011).
19. Zhang, M., Kenny, S. J., Ge, L., Xu, K. & Schekman, R. Translocation of interleukin-1beta into a vesicle intermediate in autophagy-mediated secretion. *Elife* **4**, 1–23 (2015).
20. Kimura, T. *et al.* Dedicated SNAREs and specialized TRIM cargo receptors mediate secretory autophagy. *EMBO J.* **36**, 42–60 (2017).
21. Thorburn, J. *et al.* Autophagy regulates selective HMGB1 release in tumor cells that are destined to die. *Cell Death Differ.* **16**, 175–183 (2009).

22. Young, A. R. J. *et al.* Autophagy mediates the mitotic senescence transition. *Genes Dev.* **23**, 798–803 (2009).

23. Lock, R., Kenific, C. M., Leidal, A. M., Salas, E. & Debnath, J. Autophagy-dependent production of secreted factors facilitates oncogenic RAS-Driven invasion. *Cancer Discov.* **4**, 466–479 (2014).

24. Maycotte, P., Jones, K. L., Goodall, M. L., Thorburn, J. & Thorburn, A. Autophagy supports breast cancer stem cell maintenance by regulating IL6 secretion. *Mol. Cancer Res.* **13**, 651–658 (2015).

25. Edgar, J. R. Q&A: What are exosomes, exactly? *BMC Biol.* **14**, 46 (2016).

26. Murrow, L., Malhotra, R. & Debnath, J. ATG12-ATG3 interacts with Alix to promote basal autophagic flux and late endosome function. *Nat. Cell Biol.* **17**, 300–10 (2015).

27. Guo, H. *et al.* Atg5 Disassociates the V 1 V 0 -ATPase to Promote Exosome Production and Tumor Metastasis Independent of Canonical Macroautophagy. *Dev. Cell* **43**, 716–730 (2017).

28. Behrends, C., Sowa, M. E., Gygi, S. P. & Harper, J. W. Network organization of the human autophagy system. *Nature* **466**, 68–76 (2010).

29. Leidal, A. M. *et al.* The LC3-conjugation machinery specifies the loading of RNA-binding proteins into extracellular vesicles. *Nat. Cell Biol.* (2020). doi:10.1038/s41556-019-0450-y

30. Hosokawa, N. *et al.* Nutrient-dependent mTORC1 Association with the ULK1–Atg13–FIP200 Complex Required for Autophagy. *Mol. Biol. Cell* **20**, 1981–1991 (2009).

31. Jung, C. H. *et al.* ULK-Atg13-FIP200 Complexes Mediate mTOR Signaling to the Autophagy Machinery. *Mol. Biol. Cell* **20**, (2009).

32. Ganley, I. G. *et al.* ULK1·ATG13·FIP200 complex mediates mTOR signaling and is essential for autophagy. *J. Biol. Chem.* **284**, 12297–12305 (2009).

33. Peinado, H. *et al.* Melanoma exosomes educate bone marrow progenitor cells toward a pro-metastatic phenotype through MET. *Nat. Med.* **22**, 1502–1502 (2016).

34. Hessvik, N. P. *et al.* PIKfyve inhibition increases exosome release and induces secretory autophagy. *Cell. Mol. Life Sci.* **73**, 4717–4737 (2016).

35. Fader, C. M. & Colombo, M. I. Autophagy and multivesicular bodies: two closely related partners. *Cell Death Differ.* **16**, 70–78 (2009).

36. Baixauli, F., López-Otín, C. & Mittelbrunn, M. Exosomes and autophagy: Coordinated mechanisms for the maintenance of cellular fitness. *Front. Immunol.* **5**, 403 (2014).

37. Baixauli, F. & Mittelbrunn, M. Exosomes in the Preservation of Cellular Homeostasis. in *Inflammation, Aging, and Oxidative Stress* 17–45 (2016). doi:10.1007/978-3-319-33486-8

38. Desdín-Micó, G. & Mittelbrunn, M. Role of exosomes in the protection of cellular homeostasis. *Cell Adhesion and Migration* **11**, 127–134 (2017).

39. Berg, T. O., Fengsrud, M., Strømhaug, P. E., Berg, T. & Seglen, P. O. Isolation and characterization of rat liver amphisomes: Evidence for fusion of autophagosomes with both early and late endosomes. *J. Biol. Chem.* **273**, 21883–21892 (1998).

40. Fader, C. M., Sánchez, D., Furlán, M. & Colombo, M. I. Induction of autophagy promotes fusion of multivesicular bodies with autophagic vacuoles in K562 cells. *Traffic* **9**, 230–250 (2008).

41. Miao, Y., Li, G., Zhang, X., Xu, H. & Abraham, S. N. A TRP channel senses lysosome neutralization by pathogens to trigger their expulsion. *Cell* **161**, 1306–1319 (2015).

42. de Lartigue, J. *et al.* PIKfyve regulation of endosome-linked pathways. *Traffic* **10**, 883–

893 (2009).

43. Sano, O. *et al.* Vacuolin-1 inhibits autophagy by impairing lysosomal maturation via PIKfyve inhibition. *FEBS Letters* **590**, 1576–1585 (2016).

44. Edgar, J. R., Manna, P. T., Nishimura, S., Banting, G. & Robinson, M. S. Tetherin is an exosomal tether. *Elife* **5**, 1–19 (2016).

45. Colombo, M., Raposo, G. & Théry, C. Biogenesis, Secretion, and Intercellular Interactions of Exosomes and Other Extracellular Vesicles. *Annu. Rev. Cell Dev. Biol* **30**, 255–89 (2014).

46. Kucharzewska, P. & Belting, M. Emerging roles of extracellular vesicles in the adaptive response of tumour cells to microenvironmental stress. *J. Extracell. Vesicles* **2**, 20304 (2013).

47. de Jong, O. G. *et al.* Cellular stress conditions are reflected in the protein and RNA content of endothelial cell-derived exosomes. *J. Extracell. Vesicles* **1**, 1–12 (2012).

48. Kucharzewska, P. *et al.* Exosomes reflect the hypoxic status of glioma cells and mediate hypoxia-dependent activation of vascular cells during tumor development. *Proc. Natl. Acad. Sci.* **110**, 7312–7317 (2013).

49. Eskelinen, E. L. & Saftig, P. Autophagy: a lysosomal degradation pathway with a central role in health and disease. *Biochim. Biophys. Acta* **1793**, 664–673 (2009).

50. Platt, F. M., Boland, B. & Spoel, A. C. Van Der. Lysosomal storage disorders : The cellular impact of lysosomal dysfunction. *J. Cell Biol.* **199**, 723–734 (2012).

51. Nixon, R. A. The role of autophagy in neurodegenerative disease. *Nat. Med.* **19**, 983–997 (2013).

52. Settembre, C. *et al.* A block of autophagy in lysosomal storage disorders. *Hum. Mol.*

Genet. **17**, 119–129 (2008).

53. Bowman, E. J., Sieberst, A. & Altendorft, K. Bafilomycins: A class of inhibitors of membrane ATPases from microorganisms, animal cells, and plant cells (membrane ATPase/vacuolar ATPase/macrolide antibiotics). *Proc. Nati. Acad. Sci. USA* **85**, 7972–7976 (1988).

54. Strober, W. Trypan Blue Exclusion Test of Cell Viability. in *Current Protocols in Immunology* **111**, A3.B.1-A3.B.3 (2015).

55. Hessvik, N. P. & Llorente, A. Current knowledge on exosome biogenesis and release. *Cell. Mol. Life Sci.* **75**, 193–208 (2018).

56. Mancias, J. D., Wang, X., Gygi, S. P., Harper, J. W. & Kimmelman, A. C. Quantitative proteomics identifies NCOA4 as the cargo receptor mediating ferritinophagy. *Nature* **508**, 105–109 (2014).

57. Le Guerroué, F. *et al.* Autophagosomal Content Profiling Reveals an LC3C-Dependent Piecemeal Mitophagy Pathway. *Mol. Cell* **68**, 786-796.e6 (2017).

58. Hara, T. *et al.* FIP200, a ULK-interacting protein, is required for autophagosome formation in mammalian cells. *J. Cell Biol.* **181**, 497–510 (2008).

59. Itakura, E., Kishi, C., Inoue, K. & Mizushima, N. Beclin 1 forms two distinct phosphatidylinositol 3-kinase complexes with mammalian Atg14 and UVRAG. *Mol. Biol. Cell* **19**, 5360–5372 (2008).

60. Matsunaga, K. *et al.* Two Beclin 1-binding proteins, Atg14L and Rubicon, reciprocally regulate autophagy at different stages. *Nat. Cell Biol.* **11**, 385–396 (2009).

61. Sun, Q. *et al.* Identification of Barkor as a mammalian autophagy-specific factor for Beclin 1 and class III phosphatidylinositol 3-kinase. *Proc. Natl. Acad. Sci.* **105**, 19211–

19216 (2008).

62. Ponpuak, M. *et al.* Secretory autophagy. *Curr. Opin. Cell Biol.* **35**, 106–116 (2015).

63. Ostrowski, M. *et al.* Rab27a and Rab27b control different steps of the exosome secretion pathway. *Nat. Cell Biol.* **12**, 19–30 (2010).

64. Chen, Y. Da *et al.* Exophagy of annexin A2 via RAB11, RAB8A and RAB27A in IFN-γ-stimulated lung epithelial cells. *Sci. Rep.* **7**, 1–13 (2017).

65. Klionsky, D. J., Elazar, Z., Seglen, P. O. & Rubinsztein, D. C. Does bafilomycin A 1 block the fusion of autophagosomes with lysosomes? *Autophagy* **4**, 849–850 (2008).

66. Hamasaki, M. *et al.* Autophagosomes form at ER-mitochondria contact sites. *Nature* **495**, 389–393 (2013).

67. Kumar, S. *et al.* Phosphorylation of Syntaxin 17 by TBK1 controls autophagy initiation. *Dev. Cell* **49**, 130–144 (2019).

68. Théry, C., Clayton, A., Amigorena, S. & Raposo, G. Isolation and Characterization of Exosomes from Cell Culture Supernatants. in *Current protocols in cell biology* **Chapter 3**, 1–29 (2006).

69. Chen, E. Y. *et al.* Enrichr: interactive and collaborative HTML5 gene list enrichment analysis tool. *BMC Bioinformatics* **14**, 1471–2105 (2013).

70. Kuleshov, M. V. *et al.* Enrichr: a comprehensive gene set enrichment analysis web server 2016 update. *Nucleic Acids Res.* **44**, W90–W97 (2016).

71. Mi, H., Muruganujan, A., Ebert, D., Huang, X. & Thomas, P. D. PANTHER version 14: More genomes, a new PANTHER GO-slim and improvements in enrichment analysis tools. *Nucleic Acids Res.* **47**, D419–D426 (2019).

72. Hulsen, T., de Vlieg, J. & Alkema, W. BioVenn - A web application for the comparison

and visualization of biological lists using area-proportional Venn diagrams. *BMC Genomics* **9**, 1–6 (2008).

73. Kuma, A. & Mizushima, N. Chromosomal mapping of the GFP-LC3 transgene in GFP-LC3 mice. *Autophagy* **4**, 61–62 (2008).

74. Mizushima, N., Yamamoto, A., Matsui, M., Yoshimori, T. & Ohsumi, Y. In Vivo Analysis of Autophagy in Response to Nutrient Starvation Using Transgenic Mice Expressing a Fluorescent Autophagosome Marker. *Mol. Biol. Cell* **15**, 1101–1111 (2004).

75. Kulkarni, A., Chen, J. & Maday, S. Neuronal autophagy and intercellular regulation of homeostasis in the brain. *Curr. Opin. Neurobiol.* **51**, 29–36 (2018).

76. Hara, T. *et al.* Suppression of basal autophagy in neural cells causes neurodegenerative disease in mice. *Nature* **441**, 885–9 (2006).

77. Komatsu, M. *et al.* Loss of autophagy in the central nervous system causes neurodegeneration in mice. *Nature* **441**, 880–884 (2006).

78. Pyo, J. O. *et al.* Overexpression of Atg5 in mice activates autophagy and extends lifespan. *Nat. Commun.* **4**, 1–9 (2013).

79. Querfurth, H. W. & Laferla, F. M. Alzheimer's Disease. *N. Engl. J. Med.* 329–344 (2010).

80. Zhang, Y. W., Thompson, R., Zhang, H. & Xu, H. APP processing in Alzheimer's disease. *Mol. Brain* **4**, 1–13 (2011).

81. Kuperstein, I. *et al.* Neurotoxicity of Alzheimer's disease Aβ peptides is induced by small changes in the Aβ42 to Aβ40 ratio. *EMBO J.* **29**, 3408–3420 (2010).

82. Haung Yu, W. *et al.* Macroautophagy - A novel β-amyloid peptide-generating pathway activated in Alzheimer's disease. *J. Cell Biol.* **171**, 87–98 (2005).

83. Yu, W. H. *et al.* Autophagic vacuoles are enriched in amyloid precursor protein-secretase

activities: Implications for β-amyloid peptide over-production and localization in Alzheimer's disease. *Int. J. Biochem. Cell Biol.* **36**, 2531–2540 (2004).

84. Rajendran, L. *et al.* Alzheimer's disease β-amyloid peptides are released in association with exosomes. *Proc. Natl. Acad. Sci. U. S. A.* **103**, 11172–11177 (2006).

85. Meyer-Luehmann, M. *et al.* Exogenous induction of cerebral β-amyloidogenesis is governed bf agent and host. *Science (80-.).* **313**, 1781–1784 (2006).

86. Nixon, R. A. *et al.* Extensive involvement of autophagy in Alzheimer disease: An immuno-electron microscopy study. *J. Neuropathol. Exp. Neurol.* **64**, 113–122 (2005).

87. Lee, S., Sato, Y. & Nixon, R. A. Lysosomal Proteolysis Inhibition Selectively Disrupts Axonal Transport of Degradative Organelles and Causes an Alzheimer's-Like Axonal Dystrophy. *J. Neurosci.* **31**, 7817–7830 (2011).

88. Lee, J. H. *et al.* Lysosomal proteolysis and autophagy require presenilin 1 and are disrupted by Alzheimer-related PS1 mutations. *Cell* **141**, 1146–1158 (2010).

89. Lee, J. H. *et al.* Presenilin 1 Maintains Lysosomal Ca2+ Homeostasis via TRPML1 by Regulating vATPase-Mediated Lysosome Acidification. *Cell Rep.* **12**, 1430–1444 (2015).

90. Scheuner, D. *et al.* Secreted amyloid beta-protein similar to that in the senile plaques of Alzheimer's disease is increased in vivo by the presenilin 1 and 2 and APP mutations linked to familial Alzheimer's disease. *Nat. Med.* **2**, 864–870 (1996).

91. Polymeropoulos, M. H. *et al.* Mutation in the α-synuclein gene identified in families with Parkinson's disease. *Science (80-.).* **276**, 2045–2047 (1997).

92. Masliah, E. *et al.* Dopaminergic loss and inclusion body formation in α-synuclein mice: Implications for neurodegenerative disorders. *Science (80-.).* **287**, 1265–1269 (2000).

93. Luk, K. C. *et al.* Pathological a-Synuclein Transmission in Nontransgenic Mice. *Science*

(80-.). **949**, 949–953 (2012).

94. Luk, K. C. *et al.* Intracerebral inoculation of pathological α-synuclein initiates a rapidly progressive neurodegenerative α-synucleinopathy in mice. *J. Exp. Med.* **209**, 975–988 (2012).

95. Masuda-Suzukake, M. *et al.* Prion-like spreading of pathological α-synuclein in brain. *Brain* **136**, 1128–1138 (2013).

96. Emmanouilidou, E. *et al.* Cell-produced alpha-synuclein is secreted in a calcium-dependent manner by exosomes and impacts neuronal survival. *J Neurosci* **30**, 6838–6851 (2010).

97. Webb, J. L., Ravikumar, B., Atkins, J., Skepper, J. N. & Rubinsztein, D. C. α-synuclein Is Degraded by Both Autophagy and the Proteasome. *J. Biol. Chem.* **278**, 25009–25013 (2003).

98. Tanik, S. A., Schultheiss, C. E., Volpicelli-Daley, L. A., Brunden, K. R. & Lee, V. M. Y. Lewy body-like α-synuclein aggregates resist degradation and impair macroautophagy. *J. Biol. Chem.* **288**, 15194–15210 (2013).

99. Stefanis, L., Larsen, K. E., Rideout, H. J., Sulzer, D. & Greene, L. a. Expression of A53T mutant but not wild-type alpha-synuclein in PC12 cells induces alterations of the ubiquitin-dependent degradation system, loss of dopamine release, and autophagic cell death. *J. Neurosci.* **21**, 9549–60 (2001).

100. Gitler, A. D. *et al.* α-Synuclein is part of a diverse and highly conserved interaction network that includes PARK9 and manganese toxicity. *Nat. Genet.* **41**, 308–315 (2009).

101. Dehay, B. *et al.* Loss of P-type ATPase ATP13A2/PARK9 function induces general lysosomal deficiency and leads to Parkinson disease neurodegeneration. *Proc. Natl. Acad.*

Sci. **109**, 9611–9616 (2012).

102. Henry, A. G. *et al.* Pathogenic LRRK2 mutations, through increased kinase activity, produce enlarged lysosomes with reduced degradative capacity and increase ATP13A2 expression. *Hum. Mol. Genet.* **24**, 6013–6028 (2015).

103. Wallings, R., Connor-Robson, N. & Wade-Martins, R. LRRK2 interacts with the vacuolar-type H+-ATPase pump a1 subunit to regulate lysosomal function. *Hum. Mol. Genet.* **28**, 2696–2710 (2019).

104. Melentijevic, I. *et al.* C. elegans neurons jettison protein aggregates and mitochondria under neurotoxic stress. *Nature* **542**, 367–371 (2017).

105. Nilsson, P. *et al.* Autophagy-related protein 7 deficiency in amyloid β (Aβ) precursor protein transgenic mice decreases Aβ in the multivesicular bodies and induces Aβ accumulation in the golgi. *Am. J. Pathol.* **185**, 305–313 (2015).

106. Nilsson, P. *et al.* Aβ Secretion and Plaque Formation Depend on Autophagy. *Cell Rep.* **5**, 61–69 (2013).

107. Alvarez-Erviti, L. *et al.* Lysosomal dysfunction increases exosome-mediated alpha-synuclein release and transmission. *Neurobiol. Dis.* **42**, 360–367 (2011).

108. Danzer, K. M. *et al.* Exosomal cell-to-cell transmission of alpha synuclein oligomers. *Mol. Neurodegener.* **7**, 1–18 (2012).

109. Minakaki, G. *et al.* Autophagy inhibition promotes SNCA/alpha-synuclein release and transfer via extracellular vesicles with a hybrid autophagosome-exosome-like phenotype. *Autophagy* **14**, 98–119 (2018).

APPENDIX A: At the crossroads of autophagy and infection: Noncanonical roles for ATG proteins in viral replication

The following appendix is published work

Solvik T, Debnath J.

Contributions: I performed the literature review search and wrote the initial drafts of the article. Jayanta Debnath developed the article concept and edited the drafts before publication.

At the crossroads of autophagy and infection: Noncanonical roles for ATG proteins in viral replication

Tina Solvik[1,2,3] and Jayanta Debnath[1,2]

[1]Department of Pathology, [2]Helen Diller Family Comprehensive Cancer Center, and [3]Biomedical Sciences Graduate Program, University of California, San Francisco, San Francisco, CA 94143

Autophagy-related (ATG) proteins have increasingly demonstrated functions other than cellular self-eating. In this issue, Mauthe et al. (2016. J. Cell Biol. http://dx.doi.org/10.1083/jcb.201602046) conduct an unbiased RNA interference screen of the ATG proteome to reveal numerous noncanonical roles for ATG proteins during viral infection.

Macroautophagy (autophagy) involves the formation of a double-membrane organelle called the autophagosome, which sequesters cytoplasmic components that are degraded upon its fusion with the lysosome (Stolz et al., 2014; Kaur and Debnath, 2015). Studies in yeast have identified >30 autophagy-related (ATG) proteins, many of which have identified mammalian orthologues. The canonical process of autophagy begins with initiation at the phagophore assembly site, mediated by the UNC51-like kinase (ULK) complex, which is composed of the ATG proteins ULK1/2, ATG13, FIP200, and ATG101. The ULK complex supports the activation of a class III phosphatidylinositol 3-kinase complex consisting of Beclin 1 (ATG6), ATG14, and VPS34 to produce phosphatidylinositol triphosphate, which serves as the initial membrane mark recognized by early autophagic effector proteins. Phagophore membrane expansion is mediated by the two ubiquitin-like conjugation systems involving multiple ATG proteins that ultimately lead to the lipidation of microtubule-associated protein 1 light chain 3 (LC3), the mammalian orthologue of ATG8. LC3 is recognized by autophagy cargo receptors that promote the selective capture and engulfment of proteins, organelles, or microbes. The closed autophagosome is then trafficked to and fuses with the lysosome to degrade its cargo (Stolz et al., 2014; Kaur and Debnath, 2015). ATG proteins traditionally have been studied for their roles in autophagosome formation and maturation, but we have recently begun to appreciate that they may have pleiotropic roles beyond autophagy (Bestebroer et al., 2013). In this issue, through a comprehensive functional screen for ATG proteins in the control of viral replication, Mauthe et al. highlight the importance of the nontraditional functions of ATG proteins in the host viral response.

In a tour-de-force study examining multiple models of viral infection, Mauthe et al. (2016) interrogated the individual roles of ATG proteins in the replication of herpes simplex virus type 1, mouse hepatitis virus (MHV), vaccinia virus (VaV), semliki forest virus, encephalomyocarditis virus, and influenza A virus. The authors generated a curated siRNA library to target all ATG proteins individually as well as functionally redundant groups concurrently to evaluate how they promote the replication of these six viruses in two model cell lines (HeLa and U2OS). Indeed, their screen reveals that unconventional functions of ATG proteins are widespread; overall, 16 out of the 44 tested ATG proteins (36%) appear to have unconventional functions. Rarely does knockdown of individual ATG genes result in concordant effects on viral replication, arguing against a general role for autophagy. Moreover, the authors fail to identify any single ATG protein that regulates viral replication in all of the tested viruses; rather, specific ATG genes influenced the replication of each virus. Remarkably, most of the ATG proteins show a beneficial role for VaV replication in U2OS cells yet negatively impact VaV replication in HeLa cells. Overall, the effect of ATG loss of function on viral replication is exquisitely ATG specific, virus specific, and cell line specific.

To demonstrate functions of ATG proteins independent of autophagy, the authors scrutinized ATG13 and FIP200, two ULK complex proteins that initiate formation of the autophagosome, and found that these proteins exert effects on viral replication distinct from the effects of other ULK complex components. Mauthe et al. (2016) demonstrate that depletion of ATG13 and FIP200 reduces the replication of two picornaviruses, encephalomyocarditis virus and coxsackievirus (CV) B3, whereas the other ULK complex components promote their replication. Furthermore, a principal upstream regulator of ULK complex activity, mammalian target of rapamycin complex 1, showed no changes in activity during infection or knockdown of the ULK complex components. Altogether, this evidence indicates that ATG13 and FIP200 act independently of the ULK complex to modify picornaviral replication outside the context of autophagy.

Although the precise mechanism of this unconventional function of ATG13 and FIP200 remains to be elucidated, Mauthe et al. (2016) uncovered that these proteins control viral replication as opposed to viral entry or viral translation. However, ATG13 and FIP200 do not interact with any CV proteins or affect the morphology of CV replication structures, suggesting

Correspondence to Jayanta Debnath: jayanta.debnath@ucsf.edu

The Rockefeller University Press $30.00
J. Cell Biol. Vol. 214 No. 5 503–505
www.jcb.org/cgi/doi/10.1083/jcb.201608032

the proteins have an indirect effect on viral replication. RNA sequencing analysis demonstrates that ATG13 and FIP200 affect genes predominantly involved in transcriptional regulation during CV infection. Future studies expanding on these results are needed to dissect the exact mechanism by which ATG13 and FIP200 reduce picornaviral replication.

Autophagy has inexorably been linked to the host cellular response to diverse intracellular pathogens. Indeed, autophagy frequently serves as an innate mechanism that sequesters or clears offending pathogens from the host cell, termed xenophagy. In response to infection, pathogen- and damage-associated molecular patterns stimulate pattern recognition receptors, which then activate ATG proteins to induce autophagy or promote recognition of the microbe by the LC3-positive autophagosome (Deretic et al., 2015). Nevertheless, the autophagy trafficking process can be subverted by pathogens that have adapted to avoid or use autophagy to their own benefit (Deretic and Levine, 2009). One example is poliovirus, which utilizes LC3 to promote its nonlytic viral release, potentially by the fusion of LC3-positive vesicles containing poliovirus with the plasma membrane (Bird et al., 2014).

Interestingly, this last example broaches how ATG proteins, either as individual proteins or in groups, may enable unconventional functions distinct from the canonical process of autophagy. This can include entirely novel functions or ATG processes that use only a subset of the core components (Bestebroer et al., 2013). Before Mauthe et al. (2016), a comprehensive, unbiased analysis of the entire ATG proteome to uncover the autophagy-independent functions of ATG proteins during infection had not been undertaken. Nevertheless, other studies have highlighted some of the emerging noncanonical roles of ATG proteins during microbial pathogenesis. A well characterized example is LC3-associated phagocytosis (LAP), in which a select group of ATG proteins promotes maturation and degradation of the phagosome. Upon toll-like receptor-triggered phagocytosis, Beclin 1 is recruited to the phagosome, where it induces production of phosphatidylinositol triphosphate and localization of LC3, causing fusion with the lysosome (Sanjuan et al., 2007). Although LAP requires several ATG proteins—Beclin 1, LC3, ATG5, and ATG7, among others—it is mechanistically distinct from autophagy as it does not use the ULK complex that initiates canonical autophagy. In addition, LAP utilizes proteins such as Rubicon, which is inhibitory to autophagy, further demonstrating deviation from the conventional functions of ATG proteins (Martinez et al., 2015). LAP serves as a host defense system that targets several pathogens, including *Salmonella typhimurium* and *Aspergillus fumigatus* (Huang et al., 2009; Martinez et al., 2015).

In other cases, the growing list of noncanonical functions of ATG proteins has led the field to reevaluate a general role of the autophagy pathway in certain aspects of microbial pathogenesis. First, the autophagy pathway was proposed to defend against *Mycobacterium tuberculosis* infection because induction of autophagy by starvation or treatment with rapamycin reduces *M. tuberculosis* viability and because myeloid-specific deletion of ATG5 results in increased inflammation and bacterial load in the lungs (Castillo et al., 2012; Watson et al., 2012). Although this result originally assumed a protective function of autophagy, recent work demonstrates that ATG5 is unique in its ability to restrict *M. tuberculosis* infection. In stark contrast to ATG5, the genetic deletion of other essential ATG genes (ATG3, ATG7, ATG12, ATG14L, and ATG16L) has no effect on *M. tuberculosis* infection in vivo. Instead, ATG5 prevents accumulation of polymorphonuclear cells in the lungs, thereby controlling inflammation and *M. tuberculosis* replication (Kimmey et al., 2015).

During *Brucella abortus* infection, multiple ATG proteins implicated in the early steps of autophagosome initiation, such as ULK1 and Beclin 1, are involved in the formation of a *B. abortus*–containing vacuole (BCV) with autophagic features (aBCV), which promotes bacterial proliferation. Double-membrane crescents reminiscent of the autophagosome engulf BCVs late in infection but do not degrade or clear the bacteria. Instead, ULK1, Beclin 1, and class III phosphatidylinositol 3-kinase activity are all required for the conversion of BCVs into aBCVs. However, the ATG conjugation pathways involved in autophagosome elongation play no role in aBCV formation. Furthermore, these aBCVs facilitate bacterial release and infection of neighboring cells, demonstrating that very specific components of autophagosome initiation promote *B. abortus* infection (Starr et al., 2012).

Moreover, the lipidated form of LC3 (LC3-II) is essential for autophagosome formation and crucially interacts with cytoplasmic cargo to be degraded. However, during MHV infection, unlipidated LC3 (LC3-I) promotes viral replication in double-membrane vesicles (DMVs). The similarity of DMVs to autophagosomes prompted speculation that classical autophagy controlled MHV infection. However, ATG5 does not affect infection, and only LC3-I colocalizes with MHV DMVs, suggesting that canonical autophagy is not involved (Zhao et al., 2007). Further investigation revealed that two proteins in the ER-associated degradation pathway interact with LC3-I and MHV replication translation complexes, that MHV DMVs are of ER origin, and that LC3-I, but not LC3-II, is required for MHV replication (Reggiori et al., 2010). Remarkably, these LC3-I–positive DMVs represent another LC3-presenting membrane distinct from the canonical double-membrane autophagosome as well as the LC3-II–positive single-membrane phagosome in LAP.

Lastly, during mouse norovirus (MNV) infection, IFN-γ–activated phagocytes use ATG5-ATG12/ATG16L1 to inhibit formation of the viral replication complex, thus restricting infection. This ATG complex typically promotes LC3 lipidation, resulting in expansion of the autophagosome. Based on the requirement for ATG5 in IFN-γ–mediated inhibition of MNV replication, autophagy was initially suggested as the mechanism of host defense. However, IFN-γ has no effect on autophagy in phagocytes, and inducing or inhibiting autophagy does not alter MNV replication. Instead, only ATG5-ATG12/ATG16L1 is required for MNV replication inhibition, and ATG16L1 localizes to the MNV replication complex. ATG5-ATG12/ATG16L1 is required for IFN-γ–mediated suppression of MNV polymerase expression and, therefore, replication as a whole, an example of multiple ATG proteins functioning to inhibit viral infection (Hwang et al., 2012).

Ultimately, the discovery of widespread autophagy-independent functions of ATG proteins marks a significant turning point as well as reinforces an important caveat for the field. Going forward, researchers must use caution when attributing a phenotype to canonical autophagy based on the genetic analysis of a single ATG protein. The experiments in Mauthe et al. (2016) poignantly illustrate the need to functionally test multiple ATG proteins when characterizing a phenotype to ascertain a general role for autophagy as opposed to a distinct function mediated by individual ATG proteins.

Acknowledgments

J. Debnath is supported by the National Institutes of Health (CA126792, CA188404, and CA201849), U.S. Department of Defense Breast Cancer Research Program (W81XWH-11-1-0130), and Samuel Waxman Cancer Research Foundation.

The authors declare no competing financial interests.

Submitted: 8 August 2016
Accepted: 8 August 2016

References

Bestebroer, J., P. V'kovski, M. Mauthe, and F. Reggiori. 2013. Hidden behind autophagy: the unconventional roles of ATG proteins. *Traffic.* 14:1029–1041. http://dx.doi.org/10.1111/tra.12091

Bird, S.W., N.D. Maynard, M.W. Covert, and K. Kirkegaard. 2014. Nonlytic viral spread enhanced by autophagy components. *Proc. Natl. Acad. Sci. USA.* 111:13081–13086. http://dx.doi.org/10.1073/pnas.1401437111

Castillo, E.F., A. Dekonenko, J. Arko-Mensah, M.A. Mandell, N. Dupont, S. Jiang, M. Delgado-Vargas, G.S. Timmins, D. Bhattacharya, H. Yang, et al. 2012. Autophagy protects against active tuberculosis by suppressing bacterial burden and inflammation. *Proc. Natl. Acad. Sci. USA.* 109:E3168–E3176. http://dx.doi.org/10.1073/pnas.1210500109

Deretic, V., and B. Levine. 2009. Autophagy, immunity, and microbial adaptations. *Cell Host Microbe.* 5:527–549. http://dx.doi.org/10.1016/j.chom.2009.05.016

Deretic, V., T. Kimura, G. Timmins, P. Moseley, S. Chauhan, and M. Mandell. 2015. Immunologic manifestations of autophagy. *J. Clin. Invest.* 125:75–84. http://dx.doi.org/10.1172/JCI73945

Huang, J., V. Canadien, G.Y. Lam, B.E. Steinberg, M.C. Dinauer, M.A. Magalhaes, M. Glogauer, S. Grinstein, and J.H. Brumell. 2009. Activation of antibacterial autophagy by NADPH oxidases. *Proc. Natl. Acad. Sci. USA.* 106:6226–6231. http://dx.doi.org/10.1073/pnas.0811045106

Hwang, S., N.S. Maloney, M.W. Bruinsma, G. Goel, E. Duan, L. Zhang, B. Shrestha, M.S. Diamond, A. Dani, S.V. Sosnovtsev, et al. 2012. Nondegradative role of Atg5-Atg12/Atg16L1 autophagy protein complex in antiviral activity of interferon gamma. *Cell Host Microbe.* 11:397–409. http://dx.doi.org/10.1016/j.chom.2012.03.002

Kaur, J., and J. Debnath. 2015. Autophagy at the crossroads of catabolism and anabolism. *Nat. Rev. Mol. Cell Biol.* 16:461–472. http://dx.doi.org/10.1038/nrm4024

Kimmey, J.M., J.P. Huynh, L.A. Weiss, S. Park, A. Kambal, J. Debnath, H.W. Virgin, and C.L. Stallings. 2015. Unique role for ATG5 in neutrophil-mediated immunopathology during *M. tuberculosis* infection. *Nature.* 528:565–569. http://dx.doi.org/10.1038/nature16451

Martinez, J., R.K. Malireddi, Q. Lu, L.D. Cunha, S. Pelletier, S. Gingras, R. Orchard, J.L. Guan, H. Tan, J. Peng, et al. 2015. Molecular characterization of LC3-associated phagocytosis reveals distinct roles for Rubicon, NOX2 and autophagy proteins. *Nat. Cell Biol.* 17:893–906. http://dx.doi.org/10.1038/ncb3192

Mauthe, M., M. Langereis, J. Jung, X. Zhou, A. Jones, W. Omta, S.A. Tooze, B. Stork, S.R. Paludan, T. Ahola, et al. 2016. An siRNA screen for ATG protein depletion reveals the extent of the unconventional functions of the autophagy proteome in virus replication. *J. Cell Biol.* http://dx.doi.org/10.1083/jcb.201602046

Reggiori, F., I. Monastyrska, M.H. Verheije, T. Calì, M. Ulasli, S. Bianchi, R. Bernasconi, C.A. de Haan, and M. Molinari. 2010. Coronaviruses hijack the LC3-I-positive EDEMosomes, ER-derived vesicles exporting short-lived ERAD regulators, for replication. *Cell Host Microbe.* 7:500–508. http://dx.doi.org/10.1016/j.chom.2010.05.013

Sanjuan, M.A., C.P. Dillon, S.W. Tait, S. Moshiach, F. Dorsey, S. Connell, M. Komatsu, K. Tanaka, J.L. Cleveland, S. Withoff, and D.R. Green. 2007. Toll-like receptor signalling in macrophages links the autophagy pathway to phagocytosis. *Nature.* 450:1253–1257. http://dx.doi.org/10.1038/nature06421

Starr, T., R. Child, T.D. Wehrly, B. Hansen, S. Hwang, C. López-Otin, H.W. Virgin, and J. Celli. 2012. Selective subversion of autophagy complexes facilitates completion of the Brucella intracellular cycle. *Cell Host Microbe.* 11:33–45. http://dx.doi.org/10.1016/j.chom.2011.12.002

Stolz, A., A. Ernst, and I. Dikic. 2014. Cargo recognition and trafficking in selective autophagy. *Nat. Cell Biol.* 16:495–501. http://dx.doi.org/10.1038/ncb2979

Watson, R.O., P.S. Manzanillo, and J.S. Cox. 2012. Extracellular *M. tuberculosis* DNA targets bacteria for autophagy by activating the host DNA-sensing pathway. *Cell.* 150:803–815. http://dx.doi.org/10.1016/j.cell.2012.06.040

Zhao, Z., L.B. Thackray, B.C. Miller, T.M. Lynn, M.M. Becker, E. Ward, N.N. Mizushima, M.R. Denison, and H.W. Virgin IV. 2007. Coronavirus replication does not require the autophagy gene ATG5. *Autophagy.* 3:581–585. http://dx.doi.org/10.4161/auto.4782

APPENDIX B: The LC3-conjugation machinery specifies the loading of RNA-binding proteins into extracellular vesicles

The following appendix is published work.

Leidal AM, Huang HH, Marsh T, **Solvik T**, Zhang D, Ye J, Kai F, Goldsmith J, Liu JY, Huang YH, Monkkonen T, Vlahakis A, Huang EJ, Goodarzi H, Yu L, Wiita AP, Debnath J.

Contributions: Andrew Leidal, a postdoctoral fellow in the lab, primarily performed the research presented in this paper. Jayanta Debnath supervised the project. I performed the immunofluorescence microscopy in Extended Data Figure 3h. Thank you Drew for including me in your research,

nature cell biology

ARTICLES

https://doi.org/10.1038/s41556-019-0450-y

The LC3-conjugation machinery specifies the loading of RNA-binding proteins into extracellular vesicles

Andrew M. Leidal[1], Hector H. Huang[2], Timothy Marsh[1], Tina Solvik[1], Dachuan Zhang[3], Jordan Ye[1], FuiBoon Kai[4], Juliet Goldsmith[1], Jennifer Y. Liu[1], Yu-Hsin Huang[1], Teresa Monkkonen[1], Ariadne Vlahakis[1], Eric J. Huang[1], Hani Goodarzi[5], Li Yu[3], Arun P. Wiita[2] and Jayanta Debnath[1*]

Traditionally viewed as an autodigestive pathway, autophagy also facilitates cellular secretion; however, the mechanisms underlying these processes remain unclear. Here, we demonstrate that components of the autophagy machinery specify secretion within extracellular vesicles (EVs). Using a proximity-dependent biotinylation proteomics strategy, we identify 200 putative targets of LC3-dependent secretion. This secretome consists of a highly interconnected network enriched in RNA-binding proteins (RBPs) and EV cargoes. Proteomic and RNA profiling of EVs identifies diverse RBPs and small non-coding RNAs requiring the LC3-conjugation machinery for packaging and secretion. Focusing on two RBPs, heterogeneous nuclear ribonucleoprotein K (HNRNPK) and scaffold-attachment factor B (SAFB), we demonstrate that these proteins interact with LC3 and are secreted within EVs enriched with lipidated LC3. Furthermore, their secretion requires the LC3-conjugation machinery, neutral sphingomyelinase 2 (nSMase2) and LC3-dependent recruitment of factor associated with nSMase2 activity (FAN). Hence, the LC3-conjugation pathway controls EV cargo loading and secretion.

Although autophagy is classically viewed as a lysosomal degradation process[1], genetic evidence implicates autophagy pathway components (ATGs) in secretion, including the conventional secretion of inflammatory cytokines[2], extracellular release of lysozyme[3], efficient egress of secretory lysosomes[4], EV production[5,6] and unconventional secretion of proteins lacking amino-terminal leader peptides or signal sequences[7–10]. These processes, collectively termed secretory autophagy, implicate the autophagy pathway in non-cell autonomous control of cell fate decisions and tissue microenvironments, both normally and during disease[11–13]. Nevertheless, our understanding of secretory autophagy remains rudimentary. First, apart from a limited number of protein targets, the autophagy-dependent secretome remains uncharacterized. Furthermore, studies to date largely rely on phenotypic analysis following *ATG* genetic loss-of-function, which fail to discern whether secretory defects represent a direct versus indirect consequence of impaired autophagy. Here, we describe a secretory autophagy pathway in which LC3 mediates the loading of protein and RNA cargoes into EVs for secretion outside cells.

Results

LC3 proximity-dependent biotinylation identifies proteins secreted via autophagy-dependent pathways. We developed a proximity-dependent biotinylation (BioID)[14] strategy to label proteins within autophagic intermediates that are subsequently secreted outside cells (Fig. 1a). Hypothesizing that such secreted proteins interact with or reside near MAP1LC3B (LC3), an ATG8 orthologue that captures substrates for autophagy, we fused the mutant *Escherichia coli* biotin ligase (BirA*) to the LC3 N terminus. BirA*–LC3 (myc epitope-tagged) was lipidated with phosphatidylethanolamine, localized at autophagosomes and degraded within lysosomes (Extended Data Fig. 1a–c). Biotin incubation triggered robust labelling of intracellular targets in BirA*–LC3 cells (Fig. 1b and Extended Data Fig. 1d) including multiple well-known LC3-interacting intracellular proteins (Fig. 1c). However, these molecules were not detectably secreted into conditioned medium (CM). Instead, numerous unique biotin-labelled proteins were detected in CM of BirA*–LC3 cells compared to BirA* controls (Fig. 1b). Importantly, the BirA*–LC3-labelled secretome represented secretion of proteins that were biotin-labelled inside cells, not promiscuous biotinylation following extracellular release (Extended Data Fig. 1e,f).

Combining this strategy with stable isotope labelling with amino acids in cell culture (SILAC) as a quantitative proteomics approach to detect differences in secreted protein abundance between BirA*–LC3 and BirA* via mass spectrometry (MS; Fig. 1d), we identified >350 secreted proteins in three independent biological replicates (Supplementary Table 1). Candidates were selected on the basis of significantly increased $\log_2$(BirA*–LC3/BirA*) ratios and the presence of two or more peptides. A total of 31 proteins exhibited statistically significant enrichment ($\log_2$(BirA*–LC3/BirA*) > 1; $P < 0.05$) in all 3 replicates and an additional 170 proteins were enriched in 2 of 3 replicates (Fig. 1e–g and Extended Data Fig. 2a). We refer to hits enriched in all replicates as class I proteins and those in two of three as class II proteins (Supplementary Table 1).

In the class I dataset, we identified two autophagy proteins, MAP1LC3B and ATG3, along with multiple RBPs previously shown

[1]Department of Pathology and Helen Diller Family Comprehensive Cancer Center, University of California San Francisco, San Francisco, CA, USA. [2]Department of Laboratory Medicine, University of California San Francisco, San Francisco, CA, USA. [3]State Key Laboratory of Membrane Biology, Tsinghua University-Peking University Joint Center for Life Sciences, School of Life Sciences, Tsinghua University, Beijing, China. [4]Department of Surgery, University of California San Francisco, San Francisco, CA, USA. [5]Department of Biochemistry and Biophysics, Department of Urology, and Helen Diller Family Comprehensive Cancer Center, University of California, San Francisco, San Francisco, CA, USA. *e-mail: Jayanta.Debnath@ucsf.edu

to interact with LC3 or other ATG8 family proteins[15] (Fig. 1g and Extended Data Fig. 2a–c). Together, the class I + II datasets contained 42 and 76 proteins in common with the LC3 interactome and the entire ATG8 interactome, respectively[15]. Notably, five LC3 family members ranked among the top proteins connected to the identified secreted targets (Extended Data Fig. 2d). Eighty-three percent of the proteins enriched in the BirA*–LC3-labelled secretome were previously identified in proteomics of human plasma, consistent with a role for autophagy in controlling secretion in vivo[16] (Fig. 1h). Importantly, an interaction map of the class I + II datasets revealed a highly interconnected network enriched in protein–protein interactions[17] (Extended Data Fig. 2e). Gene Ontology (GO) analyses demonstrated that the BirA*–LC-labelled secretome was highly enriched in RBPs and proteins released within EVs (Fig. 1i and Extended Data Fig. 2e); 33% of the candidates identified in our proteomic screen were previously detected in EVs and 113 out of 200 proteins have functions in messenger RNA binding[18] (Extended Data Fig. 2e–g and Supplementary Table 1). Collectively, these results suggested that LC3 and the autophagy machinery control the loading and secretion of specific proteins such as RBPs within EVs.

LC3-II and BirA*–LC3 biotinylated targets are secreted within small EVs. CM from biotin-pulsed BirA*–LC3 cells was subjected to serial differential ultracentrifugation to recover large EVs (at 10,000*g*), small EVs (at 100,000*g*)[19] and soluble proteins precipitated from the remaining sample. BirA*–LC3-labelled secreted proteins were enriched in the 100,000*g* pellet along with multiple EV markers (Fig. 2a,b). Remarkably, these 100,000*g* fractions were also enriched in the lipidated, membrane-bound form of endogenous LC3 (LC3-II), suggesting that LC3-II itself was secreted via EVs. On further purifying EVs via a linear sucrose density gradient, we found that endogenous LC3-II co-fractionated with well-defined EV markers at characteristic buoyant densities, with a slightly broader distribution into less dense fractions[19] (Fig. 2c). Transmission electron microscopy (TEM) further corroborated that samples isolated by ultracentrifugation were enriched in EVs. Importantly, endogenous LC3-II resided inside the lumen of EVs, evidenced by its protease protection in the absence of detergent, and co-purified with EVs immuno-isolated from concentrated preparations using antibodies against EV-associated tetraspanins (Fig. 2d–f). Finally, LC3-II was secreted within EVs from multiple cell types comprising diverse lineages, including primary astrocytes, and detected in vivo within EVs isolated from mouse plasma (Extended Data Fig. 3a–g).

A subset of EVs are produced by intraluminal budding from the limiting membrane of multivesicular bodies (MVBs)[20–23]. To determine whether intracellular LC3 localized to MVBs, we employed an APEX–LC3 recombinant probe[24] to visualize LC3 via TEM, which revealed numerous MVBs containing subpopulations of LC3-positive intraluminal vesicles (ILVs) (Fig. 2g). To determine whether endogenous LC3 is delivered into the lumen to MVBs, we immunostained for LC3 in cells expressing constitutively active mutant mCherry–Rab5^{Q79L}, which impairs endosomal trafficking and promotes the formation of enlarged terminal early endosomes exhibiting intraluminal budding[25,26]. We detected endogenous LC3 at the limiting membrane and in ILVs within mCherry–Rab5^{Q79L} endosomes of wild-type (WT) cells, but not in cells lacking ATG7, an autophagy regulator essential for LC3 lipidation[27] (Fig. 3a). Furthermore, LC3 co-localized with CD63 in these enlarged vesicular intermediates (Extended data 3h). In contrast, ATG14, an ATG needed for classical degradative autophagy[28,29], did not reduce the formation of LC3-positive ILVs in mCherry–Rab5^{Q79L} endosomes (Fig. 3a), suggesting a specific requirement for the LC3-conjugation pathway in incorporating LC3 into ILVs. Finally, in the absence of Rab5^{Q79L} expression, we observed significant co-localization of endogenous LC3 and CD63, further suggesting that LC3 is packaged and released within EVs by an ATG7-dependent, but not ATG14-dependent, pathway (Fig. 3b–d).

LC3-conjugation pathway is required for EV loading and secretion of RBPs. These phenotypic differences between *ATG7* versus *ATG14* deletion suggested that LC3-conjugation pathways specifically packaged proteins into EVs for secretion outside the cell[1]. To further elucidate the LC3-dependent EV proteome, we performed Tandem Mass Tag (TMT)-based quantitative proteomics comparing EVs purified from WT versus cells lacking ATG7 or ATG12, two essential components of the LC3-conjugation machinery[27] (Fig. 4a,b and Supplementary Table 2). Overall, 81% of targets enriched in the BirA*–LC3B-labelled secretome were detected in the global EV proteome, further suggesting EVs as a principal route for autophagy-dependent unconventional secretion (Fig. 2a,b and Extended Data Fig. 4a). A total of 815 proteins were enriched in EVs from WT relative to *ATG7*- and *ATG12*-deficient cells (Fig. 4c and Supplementary Table 2), including 55 proteins overlapping with the BirA*–LC3B-labelled secretome, such as the RBPs SAFB, HNRNPK, LARP1, SF3A1 and G3BP1. Although we were unable to detect LC3B, probably due to its small size and lipid modification, five LC3 family members ranked among the top proteins connected to the 815 proteins enriched in the LC3-dependent EV proteome (Fig. 4c). Moreover, as for the BirA*–LC3 secretome, GO analyses highlighted a profound enrichment in RBPs and proteins that function in RNA metabolism (Figs. 1i and 4e). Among the 815 EV proteins requiring the LC3-conjugation machinery for secretion, 112 have been identified in stress granules and 206 in processing bodies (P-bodies), two ribonucleoprotein assemblies that functionally sequester RNAs to control gene expression in response to diverse cellular stresses[30] (Extended Data Fig. 4b,c and Supplementary Table 2). Finally, among the proteins enriched within the BirA*–LC3 secretome, but not the LC3-dependent EV proteome, histones made up

Fig. 1 | Identification of proteins secreted via autophagy-dependent pathways using LC3 proximity-dependent biotinylation and quantitative secretomics. a, The proximity-dependent biotinylation strategy to label secretory autophagy targets. **b**, Protein biotinylation in whole-cell lysate (WCL, intracellular) and CM (secreted) collected from HEK293T cells stably expressing myc–BirA*–LC3, myc–BirA* or empty vector (control) following 24 h incubation with (+) or without (−) 50 μM biotin. Equal amounts of protein from TCA-precipitated CM or WCL were probed with Streptavidin–HRP (Strep–HRP) to detect biotinylated proteins, myc or GAPDH ($n = 3$ biologically independent experiments). **c**, Streptavidin affinity purification (Strep AP) and immunoblotting to detect known LC3-interacting proteins within WCL and CM of cells expressing myc–BirA*–LC3 ($n = 2$ biologically independent experiments). **d**, Autophagy-dependent secretion substrate enrichment and the quantitative secretomics workflow. **e**, A $\log_2$(H/L) histogram for the CM proteins identified in bioreplicate no. 2 and the scheme for identification of autophagy-dependent secretion candidates. **f**, Putative secretory autophagy candidates identified in $n = 3$ independent experiments (Exp.). Among the 40 hits enriched in all 3 experiments, 31 were statistically significant overall (see Extended Data Fig. 2) and classified as class I candidates. The remaining proteins along with hits enriched in 2 out of $n = 3$ experiments (170 proteins total) were designated as class II candidates. A full list of the candidates is provided in Supplementary Table 1. **g**, A $\log_2$(BirA*–LC3/BirA*) heat map of the class I candidates. **h**, The proportion of the secreted candidates (classes I and II) detected in human plasma. **i**, GO enrichment analysis of secreted candidates (classes I and II) with the top terms for molecular function and cellular component plotted according to $-\log_{10}$ FDR. The statistical significance was calculated by a one-way Fisher's exact test. Sample size, $n = 3$ independent biological replicates, yielding 200 enriched proteins in the class I + class II datasets. Data and unprocessed blots are available as source data.

a significant proportion, consistent with reports that autophagy may facilitate the secretion of histones and DNA via EV-independent mechanisms[31] (Supplementary Table 2).

Little is known regarding the pathways specifying cargo loading into EVs[20–23]. Analogous to its role in sequestering cargo during degradative autophagy[32], we hypothesized that lipidated LC3-II

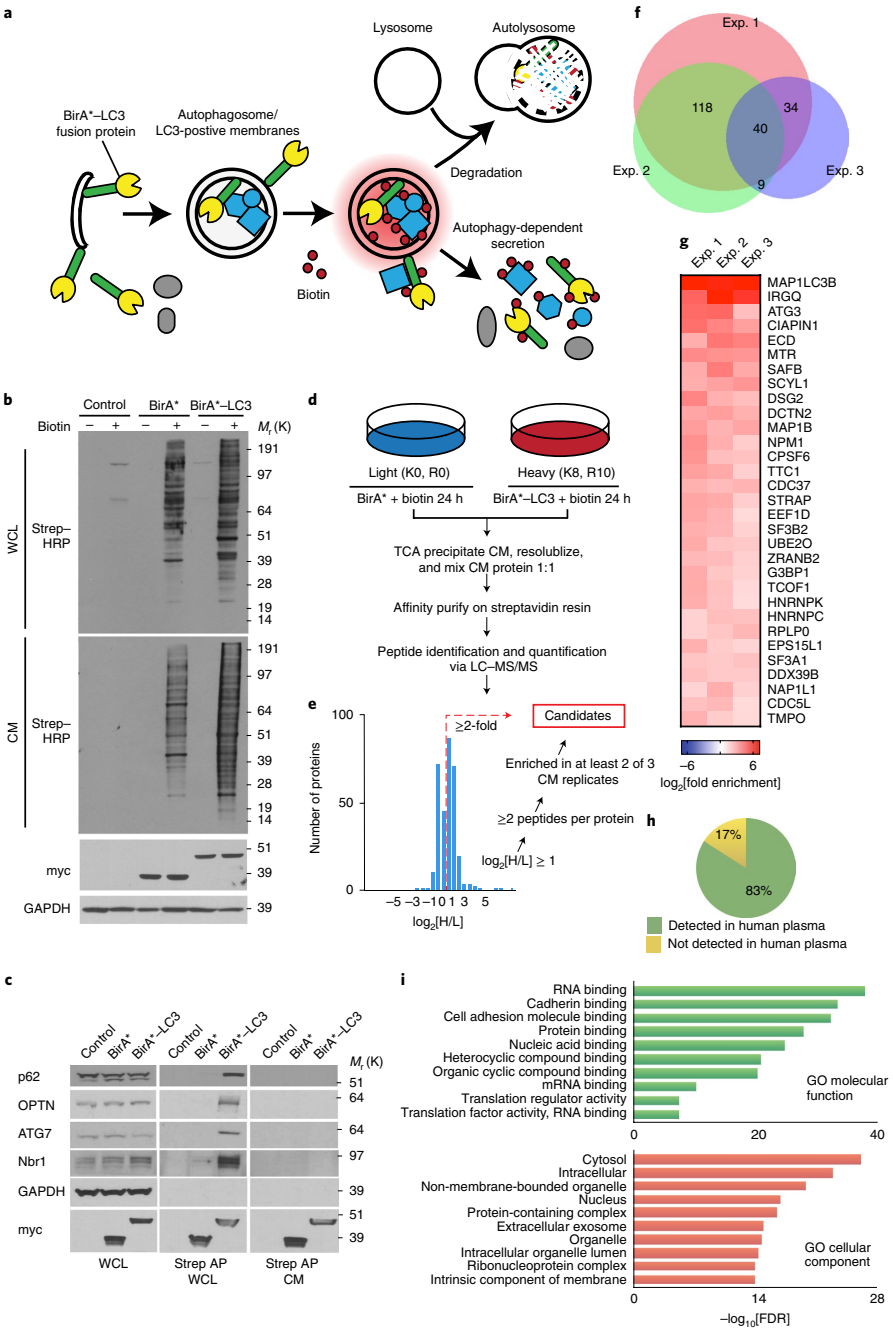

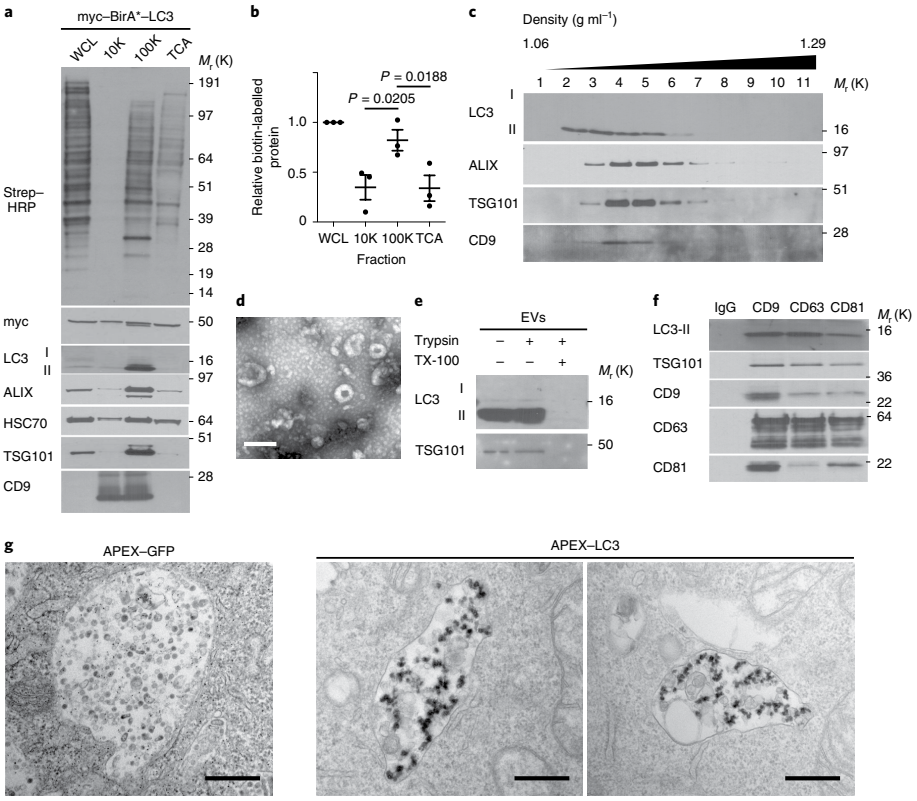

Fig. 2 | LC3-II and BirA*–LC3 biotinylated targets are secreted within EVs. a, Protein biotinylation in WCLs (intracellular) and fractionated CM collected from BirA*–LC3 HEK293T cells incubated with 50 μM biotin for 24 h. The CM was subjected to differential ultracentrifugation to recover large EVs (10,000*g*; 10K), small EVs (100,000*g*; 100K) and precipitated free soluble protein (TCA). Equal amounts of protein from WCL and fractionated CM were probed with Streptavidin–HRP (Strep–HRP) or antibodies against the indicated EV marker proteins, LC3 and myc-tagged BirA*–LC3 ($n = 3$ biologically independent replicates). **b**, Quantification of global protein biotinylation in the indicated fractions of CM relative to WCL (mean ± s.e.m.; $n = 3$ biologically independent experiments). The statistical significance between the CM fractions was calculated by one-way analysis of variance (ANOVA) coupled with Tukey's post hoc test. **c**, EVs from CM separated via linear sucrose density gradient ultracentrifugation, fractionated and immunoblotted to detect the endogenous levels of the indicated markers and LC3 ($n = 3$ biologically independent experiments). **d**, A representative transmission electron micrograph of EVs isolated via differential ultracentrifugation ($n = 3$ biologically independent samples). Scale bar, 200 nm. **e**, Representative immunoblots of the indicated proteins from untreated EVs or EVs incubated with 100 μg ml^{-1} trypsin and/or 1% Triton X-100 (TX-100) for 30 min at 4 °C ($n = 3$ biologically independent experiments). **f**, Representative immunoblots of EVs immunopurified from concentrated CM fractions using antibodies targeting the tetraspanins CD9, CD63 and CD81 or a normal mouse IgG isotype control and immunoblotted to detect the endogenous levels of the indicated markers and LC3 ($n = 3$ biologically independent experiments). **g**, Representative transmission electron micrographs of normal rat kidney epithelial cells expressing an APEX–LC3 recombinant fusion protein or APEX–GFP control and stained with 3,3-diaminobenzidine (DAB) and hydrogen peroxide (H_2O_2) ($n = 3$ biologically independent samples). Scale bars, 500 nm. Data and unprocessed blots are available as source data.

captures proteins at the MVB limiting membrane, incorporating them into ILVs for subsequent release as EVs. To test this prediction, we focused on SAFB and HNRNPK, two RBPs enriched in both the BirA*–LC3B secretome and the LC3-dependent EV proteome (Figs. 1g and 4a–c and Extended Data Fig. 4a). Endogenous SAFB and HNRNPK co-fractionated with membrane-bound LC3-II in purified EVs (Fig. 5a), interacted with LC3 (Fig. 5b), co-localized with LC3 in the lumen of a subset of mCherry–Rab5^{Q79L} endosomes (Extended Data Fig. 4d) and were detected in EVs purified from multiple cell types (Extended Data Fig. 3a). In contrast to p62 (also known as SQSTM1), these LC3-binding RBPs were not degraded during starvation-induced autophagy (Fig. 5c).

We next assessed whether various autophagy pathway components were required for SAFB and HNRNPK secretion. Deletion of the LC3-conjugation pathway components, *ATG7* and *ATG12*, reduced overall EV production and protein content relative to controls (Fig. 5d), but did not impact the size of EVs (Fig. 5e). To control for these differences in EV production among *ATG* null cells, we normalized EV lysates on the basis of protein concentration and assayed for LC3-binding RBPs. EVs from *ATG7* and *ATG12*-deleted cells were devoid of LC3-II, HNRNPK and SAFB, but still contained EV marker proteins (Fig. 5f,g). Similarly, reduced EV secretion of these targets was observed in cells deficient for *ATG3*, another essential component of the LC3-conjugation machinery[27]

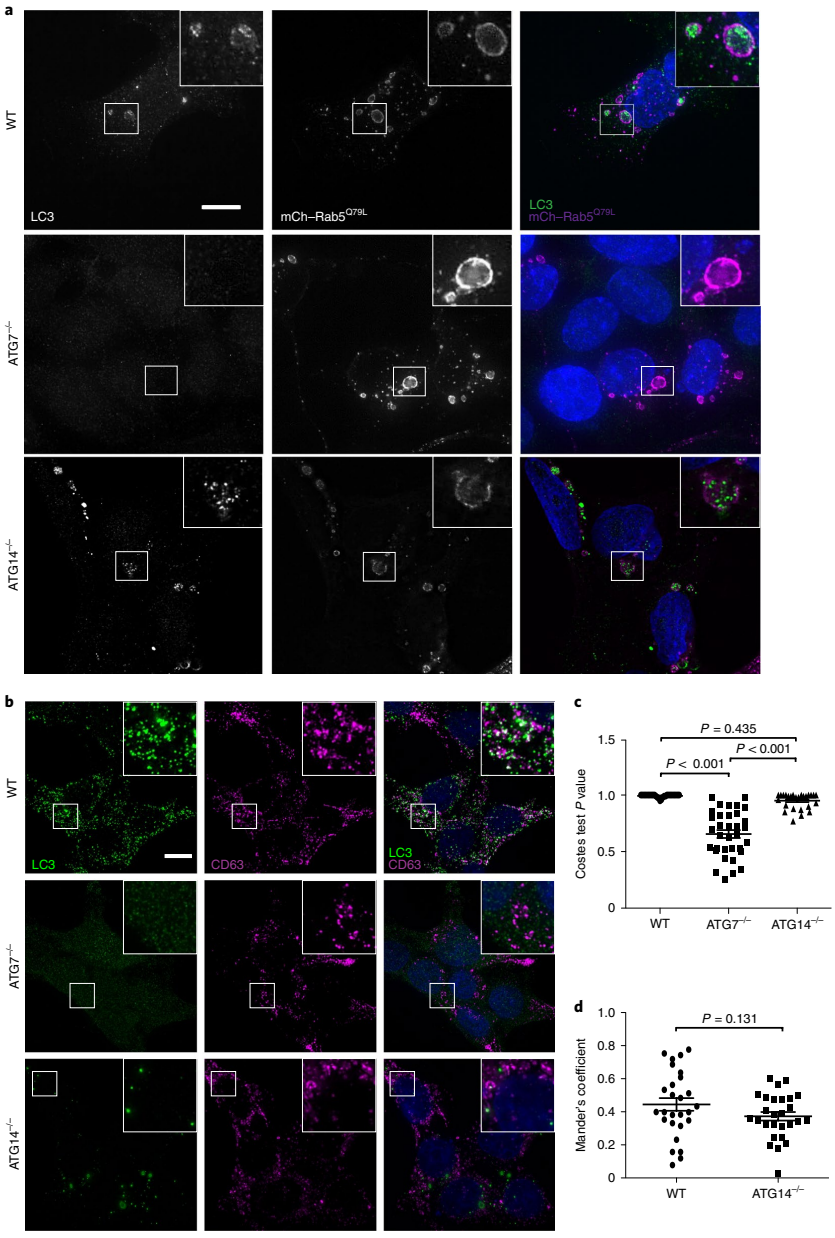

Fig. 3 | Endogenous LC3 localizes with endosomes and EV-associated tetraspanins. a, Representative fluorescence micrographs from WT, *ATG7*$^{-/-}$ and *ATG14*$^{-/-}$ HEK293T cells transfected with mCherry–Rab5^{Q79L} (magenta). Cells were immunostained for endogenous LC3 (green) ($n=3$ biologically independent experiments). Scale bar, 10 µm. **b**, Representative fluorescence micrographs from WT, *ATG7*$^{-/-}$ and *ATG14*$^{-/-}$ cells immunostained for endogenous LC3 (green) and CD63 (magenta) ($n=3$ biologically independent experiments). Scale bar, 10 µm. **c**, A scatter plot of the *P* values obtained from Costes significance tests to assess whether the overlap of LC3 and CD63 staining observed in **b** exceeds thresholds of random co-occurrence. The statistical significance was calculated by one-way ANOVA coupled with Tukey's post hoc test (mean ± s.e.m.; WT, $n=28$; *ATG7*$^{-/-}$, $n=33$; *ATG14*$^{-/-}$, $n=27$ biologically independent samples). **d**, A scatter plot of Mander's coefficients for the co-occurrence of LC3 with CD63 in the immunostained cells in **b**. The statistical significance was calculated by an unpaired two-tailed *t*-test (mean ± s.e.m.; WT, $n=27$; *ATG14*$^{-/-}$, $n=27$ biologically independent samples). Numerical data are available as source data.

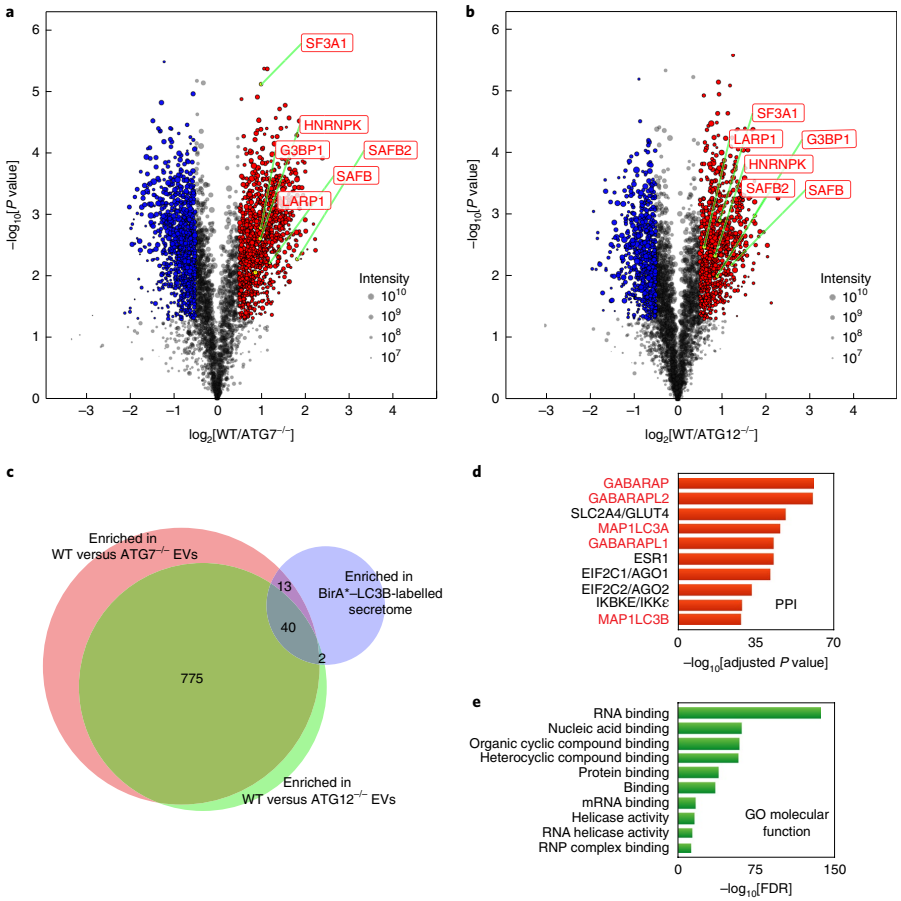

Fig. 4 | TMT quantitative secretomics identifies EV proteins secreted via the LC3-conjugation machinery. a, A volcano plot of the proteins identified within EVs from WT and *ATG7*$^{-/-}$ HEK293T cells quantified by TMT MS. The TMT-labelled proteins are plotted according to their $-\log_{10}$ *P* values as determined by two-tailed *t*-test and $\log_2$ fold enrichment (WT/*ATG7*$^{-/-}$; $n = 4$ biologically independent samples). Grey dots: proteins not relatively enriched in EVs from WT or *ATG7*$^{-/-}$ cells identified with $P > 0.05$ and/or $\log_2$ fold change between −0.5 and 0.5. Red dots: proteins significantly enriched in EVs from WT cells relative to *ATG7*$^{-/-}$ cells. Blue dots: proteins significantly enriched in EVs from *ATG7*$^{-/-}$ cells relative to WT cells. The dot size is proportional to the sum of the signal intensity for the identified proteins. **b**, A volcano plot of the proteins identified within EVs from WT and *ATG12*$^{-/-}$ cells. TMT labelled proteins according to their $-\log_{10}$ *P* values as determined by two-tailed *t*-test and $\log_2$ fold enrichment (WT/*ATG12*$^{-/-}$; $n = 4$ biologically independent samples). Grey dots: proteins not relatively enriched in EVs from WT or *ATG7*$^{-/-}$ cells identified with $P > 0.05$ and/or $\log_2$ fold change between −0.5 and 0.5. Red dots: proteins significantly enriched in EVs from WT cells relative to *ATG12*$^{-/-}$ cells. Blue dots: proteins significantly enriched in EVs from *ATG12*$^{-/-}$ cells relative to WT cells. The dot size is proportional to the sum of the signal intensity for the identified proteins. **c**, A Venn diagram showing the overlap of proteins enriched in EVs from WT cells relative to *ATG7*$^{-/-}$ cells, EVs from WT cells relative to *ATG12*$^{-/-}$ cells, and proteins enriched within the BirA*–LC3B-labelled secretome. **d**, A ranked list of the proteins with the greatest connectivity to the 815 proteins enriched in EVs from WT cells relative to *ATG7*$^{-/-}$ and *ATG12*$^{-/-}$ cells. The statistical significance was calculated in Enrichr by a one-way Fisher's exact test and adjusted using the Benjamini–Hochberg method. LC3 family members are highlighted in red. PPI, protein–protein interaction. **e**, GO enrichment analysis of 815 proteins enriched in EVs from WT cells relative to *ATG7*$^{-/-}$ and *ATG12*$^{-/-}$ cells with the top terms for molecular function plotted according to $-\log_{10}$ FDR. The statistical significance was calculated by a one-way Fisher's exact test. Data are available as source data.

(Extended Data Fig. 4e,f). Impaired secretion was not due to changes in intracellular HNRNPK and SAFB protein levels or cell death (Fig. 5f,g and Extended Data Fig. 4e–h). In contrast, loss of *ATG14* and *RB1CC1* (also known as *FIP200*), two *ATG*s required for the early initiation steps of classical autophagy, but dispensable for LC3-conjugation[28,29,33], did not attenuate EV production (Fig. 5d) or EV release of LC3-II and LC3-binding RBPs (Fig. 5f,g). Taken together with the results above that *ATG14* deletion does not impair LC3-positive ILV formation or LC3 co-localization with tetraspanins (Fig. 3a–d and Extended Data Fig. 3a), our results substantiate a specific requirement for the LC3-conjugation machinery in loading LC3-II and LC3-binding RBPs into EVs. In further

support of this, LC3-II is not secreted within plasma EVs in vivo in mice systemically deleted for *Atg12* (Extended Data Fig. 3b–d). As proteins that bind LC3 frequently contain a motif called an LC3-interaction region (LIR), we investigated whether the loading of LC3-binding RBPs into EVs involved LIR-dependent interactions. Primary sequence analyses revealed a putative LIR consensus motif within SAFB (Extended Data Fig. 5d), whereas HNRNPK contained only regions with minimal overlap. Mutation of the core hydrophobic amino acid within this motif to alanine (F199A) was sufficient to disrupt LC3 binding (Fig. 4h,i), which potently suppressed EV secretion of SAFB (Fig. 4j,k).

Overall, this secretory autophagy pathway, which we term LC3-dependent EV loading and secretion (LDELS), is distinct from classical autophagy. In support of this, treating cells with rapamycin stimulates classical autophagy, but conversely reduces EV secretion of LC3-II and LC3-binding RBPs (Extended Data Fig. 4i,j). In addition, other LC3 family members are released in EVs via mechanisms requiring the LC3-conjugation machinery (Extended Data Fig. 5a) and recent unbiased proteomic analyses have detected multiple LC3 family members in EVs from diverse cell lines[34]. Notably, we corroborated several additional RBPs identified from our proteomic screens, including G3BP1, LARP1 and SF3A1, to be secreted in EVs in an ATG7-dependent manner; similar to SAFB and HNRNPK, these targets interacted with diverse LC3 family members (Extended Data Fig. 5b,c). Together, these data suggest that the LC3-conjugation machinery and LC3 family proteins mediate the cargo loading and secretion of RBPs via EVs.

LDELS regulates extracellular RNA secretion via EVs. We further reasoned that LDELS influences extracellular RNA secretion via EVs. EVs contain diverse nucleic acids including mRNA, non-coding RNAs and DNA, but the mechanisms incorporating genetic material into EVs remain poorly defined[23,35]. To scrutinize how LDELS impacted extracellular RNA secretion, we performed quantitative RNA sequencing (RNA-seq) of samples from EVs isolated from WT, *ATG7*- and *ATG12*-deficient cells; in parallel, RNA-seq of corresponding cell samples was performed to assess intracellular gene expression differences. We observed profound differences in the small RNA bio-types isolated from EVs from WT versus LDELS-deficient cells, with minimal differences in the intracellular small RNA species (Fig. 6a,b and Supplementary Table 3). EVs derived from *ATG7*- and *ATG12*-deficient cells had relatively fewer RNA-seq reads mapping to small nucleolar RNAs (snoRNAs) and microRNAs (miRNAs), particularly in *ATG7* knockout conditions. Whereas 23% and 15% of the small RNA sequences in EVs from WT cells were snoRNAs and miRNAs, respectively, snoRNAs and miRNAs constituted 6% and 5% of EV small RNA sequences from *ATG7*-deficient cells and 18% and 5% from *ATG12*-deficient cells. Reduced levels of snoRNA and miRNA sequences in EVs from LDELS-deficient cells correlated with a relatively increased proportion of reads mapping to transfer RNA species. In contrast, *ATG7/12* deletion minimally impacted extracellular release of large RNAs within EVs (Extended Data Fig. 5e–g and Supplementary Table 3). More detailed analysis revealed 252 and 105 small non-coding RNAs to be significantly enriched in EVs from WT relative to *ATG7*- and *ATG12*-deficient cells, respectively (Fig. 6c,d); overlap between these two datasets highlighted 88 distinct RNAs requiring the LC3-conjugation machinery for efficient EV secretion (Fig. 6e and Supplementary Table 3). Most significantly, 76% of EV small non-coding RNAs regulated by LDELS were snoRNAs (or fragments thereof), a class of small RNAs canonically involved in ribosomal RNA modification[36] (Fig. 6f). Furthermore, 30% of snoRNAs secreted in an ATG7/12-dependent manner were enriched within EVs relative to total cellular RNA, consistent with their incorporation into EVs through an active packaging mechanism (Fig. 6g). Hence, LDELS influences the spectrum of extracellular small non-coding RNA species secreted within EVs.

LDELS requires nSMase2. We next scrutinized whether pathways promoting inward budding and ILV formation from the MVB limiting membrane contribute to LDELS. Although the best-characterized process involves the endosomal sorting complexes required for transport (ESCRT) machinery[20–23], short interfering RNA (siRNA) against most ESCRT components, except CHMP4b, failed to abrogate incorporation of endogenous LC3 into mCherry–Rab5^{Q79L} endosomes (Extended Data Fig. 6a–c). In parallel, we evaluated an alternative pathway in which ceramide produced by SMPD3 (also known as nSMase2) induces vesicle curvature and inward budding from the MVB[26]. Indeed, siRNA-mediated depletion of nSMase2 functionally impaired the incorporation of endogenous LC3 into mCherry–Rab5^{Q79L} endosomes (Extended Data Fig. 6a,d). Furthermore, treatment with the nSMase2 catalytic inhibitor GW4869 or short hairpin RNA (shRNA) depletion targeting nSMase2 potently suppressed secretion of LC3-II and LC3-binding RBPs (Fig. 7a–d and Extended Data Fig. 7a,b). Although nSMase2 ceramide production has been implicated in ILV formation, the mechanisms regulating nSMase2 activity and cargo selection remain obscure[32]. Bioinformatic analyses of the intracellular LC3 and ATG8 family interactomes[15] identified neutral sphingomyelinase activation associated factor (NSMAF; also known as FAN)[37] as a potential

Fig. 5 | LC3-conjugation machinery is required for EV loading and secretion of SAFB and HNRNPK. a, EVs from HEK293T CM separated via linear sucrose density gradient fractionation were immunoblotted to detect the endogenous levels of the indicated markers ($n=2$ biologically independent experiments). **b**, HEK293T cells transfected with myc-tagged LC3B or myc-BirA* were lysed, immunoprecipitated (IP) with anti-myc antibody, and immunoblotted with the indicated antibodies ($n=3$ biologically independent experiments). **c**, Cells were EBSS starved for the indicated times, lysed and immunoblotted for the indicated proteins. Baf A1 = 50 nM bafilomycin A1 for 1 h before lysis ($n=2$ biologically independent experiments). **d**, CM from equal numbers of the indicated cell types subjected to nanoparticle tracking analysis (open circles, left axis) to determine the EV number or the relative protein content measured using BCA from 100,000*g* EV fractions (black triangles, right axis) (mean ± s.e.m.; $n=3$ biologically independent experiments). The statistical significance was calculated by one-way ANOVA coupled with Dunnett's test. **e**, EV size distribution from a representative experiment for the indicated cell types in **d** ($n=3$ biologically independent experiments). **f**, WCL (left) and 100,000*g* EV fractions (right) from the indicated cell types were collected, normalized for protein concentration and immunoblotted to detect the endogenous levels of the indicated proteins ($n=4$ biologically independent experiments). **g**, Quantification of LC3 (red circles), SAFB (blue squares) and HNRNPK (green triangles) levels in EVs from the indicated *ATG*$^{-/-}$ cell lines relative to WT (mean ± s.e.m.; $n=4$ biologically independent experiments). The statistical significance was calculated by one-way ANOVA coupled with Tukey's post hoc test. **h**, HEK293T cells co-transfected with FLAG-tagged SAFB and myc-tagged LC3A, LC3B, LC3C, GABARAP (GR), GABARAPL1 (GRL1), GABARAPL2 (GRL2) or myc-BirA* were lysed, immunoprecipitated with anti-myc antibody and immunoblotted with the indicated antibodies ($n=2$ biologically independent experiments). **i**, Cells co-transfected with FLAG-tagged WT SAFB or mutant SAFB (F199A) and myc-tagged LC3A, LC3B or myc-BirA* were lysed, immunoprecipitated with anti-myc antibody and immunoblotted with the indicated antibodies ($n=2$ biologically independent experiments). **j**, WCL and EVs collected from cells expressing WT or LIR mutant SAFB (F199A) were collected and immunoblotted for FLAG–SAFB and LC3 ($n=3$ biologically independent experiments). **k**, Quantification of WT and LIR mutant SAFB (F199A) secretion in EVs from cells (mean ± s.e.m.; $n=3$ biologically independent experiments). The statistical significance was calculated by a paired two-tailed *t*-test. Data and unprocessed blots are available as source data.

LC3-associated regulator of nSMase2. Indeed, FAN robustly interacted with multiple LC3 isoforms, including LC3B, but itself was not degraded via autophagy (Fig. 7e and Extended Data Fig. 7d). Moreover, FAN knockdown suppressed EV secretion of LC3-II, SAFB and HNRNPK, whereas classical autophagy was unaltered (Fig. 7f,g and Extended Data Fig. 7e); siRNA-mediated depletion of FAN also impeded the incorporation of endogenous LC3 into mCherry–Rab5^{Q79L} endosomes (Extended Data Fig. 7f–h). Finally,

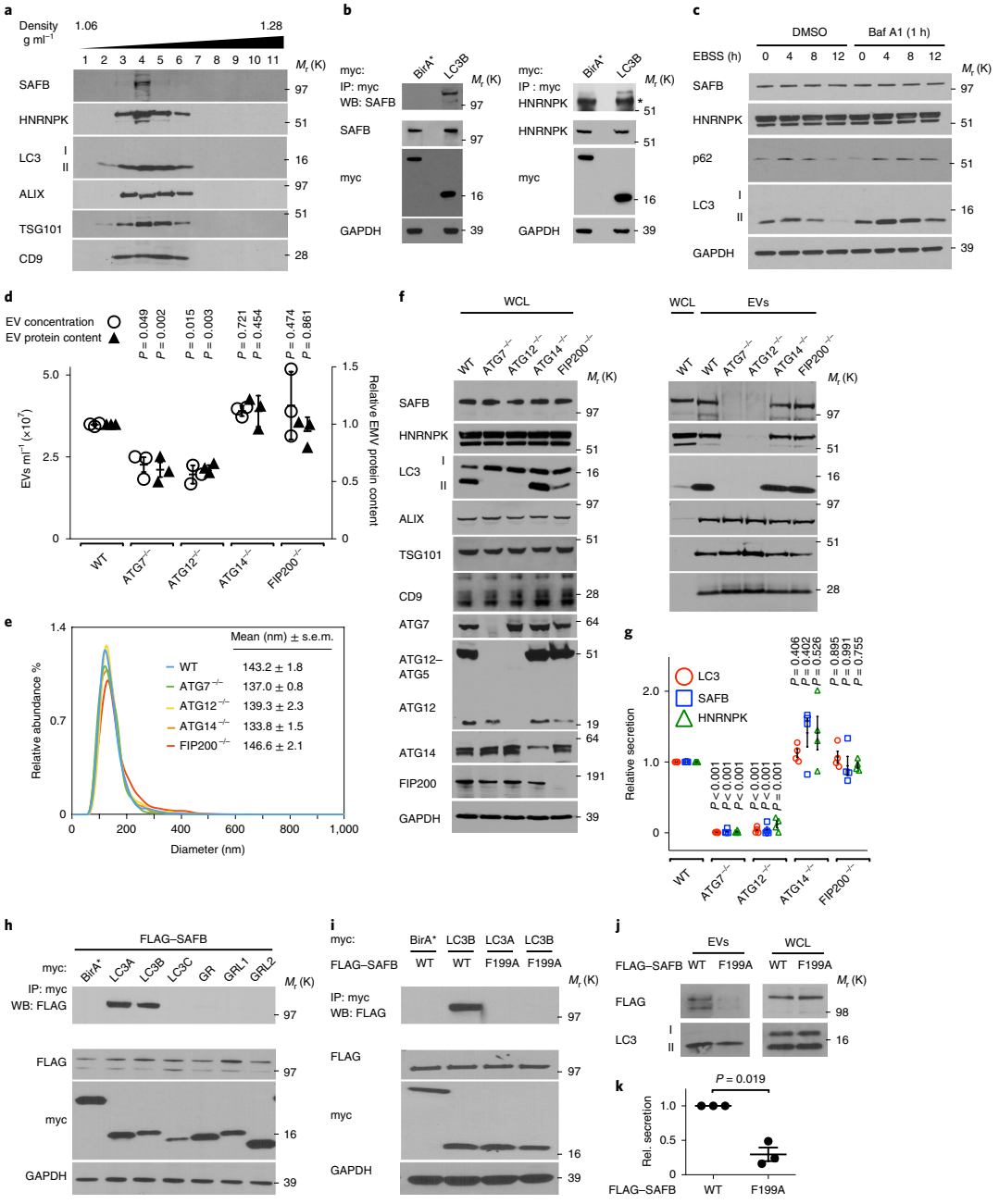

we identified a putative LIR motif within FAN, whose mutation (F602A) impaired binding to LC3 isoforms (Fig. 7h,i). Re-expression of FAN^{F602A} in FAN-deficient cells failed to rescue LDELS (Fig. 7j,k and Extended Data Fig. 7i), whereas WT FAN fully restored EV secretion of LC3 and LC3-binding RBPs (Fig. 7j,k and Extended Data Fig. 7i). Thus, FAN interaction with LC3 is crucial for an LC3-dependent circuit that coordinates cargo loading and biogenesis for nSMase pathway-derived EVs (Extended Data Fig. 7j).

Discussion

Here we demonstrate that LC3 and the LC3-conjugation machinery specify cargo loading into EVs. Previous work has intimated interconnections between autophagy and EV production. For example, we previously demonstrated a complex between ATG12 and ATG3 that interacts with the ESCRT accessory protein ALIX (PDCDIP6) and regulates small EV release[6]. In addition, the autophagy proteins ATG5 and LC3 were found to coordinately regulate MVB acidification and exosome production via control of ATP6V1E1 interactions with the V_1V_0-ATPase complex[5]. Moreover, because late endosomes can fuse to immature autophagosomes, EV biogenesis and autophagy are proposed to be functionally connected[38,39]. In this study, we delineate a process called LDELS, highlighting a unique and previously unappreciated role for the LC3-conjugation machinery in specifying the cargo packaged into EVs.

Importantly, these functions for LC3 and the conjugation machinery in LDELS are distinct from their established roles in classical autophagy. We propose that instead of using LC3 located at early autophagic intermediates, LDELS employs a pool of LC3-II located at the MVB limiting membrane to directly capture RBPs and package them into ILVs; these are subsequently released as EVs via MVB fusion with the plasma membrane (Extended Data Fig. 7j). Hence, LDELS bears similarity to a growing list of autophagy-related pathways, in which LC3-II is delivered to single membranes in the endolysosomal system, including LC3-associated endocytosis, LC3-associated phagocytosis, entosis and macroendocytic processing[40–43]. LDELS also requires nSMase2 and LC3-dependent recruitment of FAN. Indeed, ceramides produced by nSMase2 can drive the formation of membrane microdomains that impose negative membrane curvature and facilitate ESCRT-independent intraluminal budding at the MVB limiting membrane[26]. In contrast to the case for many ESCRT components, we have not detected FAN within EVs, suggesting that FAN can interact only transiently with LC3 at the limiting membrane of MVBs or may act remotely to facilitate LDELS from other compartments such as the endoplasmic reticulum or Golgi apparatus, consistent with emerging roles for inter-organelle communication in MVB cargo sorting[44,45].

Our studies also suggest that LDELS is largely independent of the ESCRT machinery; only genetic depletion of *CHMP4b* leads to reduced LC3 incorporation into Rab5^{Q79L} endosomes. CHMP4b has recently been implicated in endosomal microautophagy[42], suggesting that these two pathways may be interconnected. However, in contrast to endosomal microautophagy, LDELS does not appear to require VPS4a/b. Further scrutinizing whether LDELS requires additional components of the ESCRT machinery and its relationship to degradative pathways such as endosomal microautophagy and LC3-associated endocytosis remains an important topic for future study[41,42].

Among the array of identified LDELS cargoes, RBPs represent the most prominent functional class of proteins. Although EVs are known to contain diverse RBPs, the mechanisms specifying their loading and secretion remain largely unclear[23,35]. We demonstrate here that LC3 and ATG8 family members interact with multiple secreted RBPs, many of which contain LIR consensus motifs, and show that mutation of the LIR within SAFB (SAFB^{F199A}) is sufficient to impair its secretion via EVs. Interestingly, many LDELS targets are detected in RNA granules, including stress granules and P-bodies[46,47]. Autophagy is proposed to regulate stress granule clearance[48], but its role in RNA granule homeostasis appears more complex and nuanced beyond simple turnover of stress granule components[49–52]. We are actively investigating how LDELS interacts with classical autophagy to regulate the dynamic remodelling of RNA granules.

Consistent with its role in RBP secretion, the loss of LDELS via genetic ablation of *ATG7* and *ATG12* leads to profound changes in the extracellular small non-coding RNA profiles present in EVs. EVs contain diverse small RNA bio-types and the mechanisms that contribute to the packaging and secretion of small RNAs are only beginning to be unravelled[35,53–56]. Although LDELS affects secretion of multiple small RNA bio-types, its greatest impact is on snoRNAs, a class of nuclear small non-coding RNAs involved in ribosomal RNA modification[36]. Indeed, snoRNAs (or fragments thereof) are readily detected in EVs purified from human plasma and cell culture CM[57–63]. However, the mechanisms specifying snoRNA secretion and the functions of extracellular snoRNAs remain largely unclear. Interestingly, a number of RBPs secreted via LDELS can preferentially bind snoRNAs, including SAFB[64]. Furthermore, processed forms of snoRNAs interact with hnRNPs and cellular stresses such as starvation and oxidative damage promote the accumulation of snoRNAs in the cytoplasm[65–67]. Deciphering whether LDELS directs the EV secretion of snoRNAs as a means of regulating protein homeostasis during cell stress remains an intriguing question for future investigation.

Originally described as a mechanism to selectively eliminate proteins, lipids and nucleic acids from cells, EVs are emerging as an important mode of intercellular communication in diverse physiological and pathological processes[20–23]. Elaborating how LDELS

Fig. 6 | LDELS regulates the small non-coding RNA composition of EVs. a, The proportion of RNA-seq reads in total cellular RNA from WT, *ATG7*$^{-/-}$ and *ATG12*$^{-/-}$ HEK293T cells from the different classes of small non-coding RNA ($n=3$ biologically independent samples). **b**, The proportion of RNA-seq reads in total EV RNA from WT, *ATG7*$^{-/-}$ and *ATG12*$^{-/-}$ HEK293T cells from the different classes of small non-coding RNA ($n=3$ biologically independent samples). **c**, A volcano plot of the small non-coding RNAs detected in EVs from WT and *ATG7*$^{-/-}$ cells quantified by RNA-seq. The results are plotted according to $-\log_{10}$ *P* values as determined by DESeq2 and $\log_2$ fold enrichment ($n=3$ biologically independent samples; WT/*ATG7*$^{-/-}$). Grey dots: RNAs identified with $P>0.05$ and/or $\log_2$ fold change between −0.5 and 0.5, and thus not relatively enriched in EVs from WT or *ATG7*$^{-/-}$ cells. The $\log_2$ fold change reflects the WT EV RNA/WT cell RNA to *ATG7*$^{-/-}$ EV RNA/*ATG7*$^{-/-}$ cell RNA ratio. Black dots: small non-coding RNAs significantly enriched in EVs from WT or *ATG7*$^{-/-}$ cells. Red dots: snoRNAs significantly enriched in EVs from WT or *ATG7*$^{-/-}$ cells. **d**, A volcano plot of the small non-coding RNAs detected in EVs from WT and *ATG12*$^{-/-}$ cells quantified by RNA-seq. The results are plotted according to $-\log_{10}$ *P* values as determined by DESeq2 and $\log_2$ fold enrichment ($n=3$ biologically independent samples; WT/*ATG12*$^{-/-}$). Grey dots: RNAs with a $P>0.05$ and/or $\log_2$ fold change between −0.5 and 0.5, and thus not relatively enriched in EVs from WT or *ATG12*$^{-/-}$ cells. The $\log_2$ fold change reflects the WT EV RNA/WT cell RNA to *ATG12*$^{-/-}$ EV RNA/*ATG12*$^{-/-}$ cell RNA ratio. Black dots: small non-coding RNAs significantly enriched in EVs from WT or *ATG12*$^{-/-}$ cells. Red dots: snoRNAs significantly enriched in EVs from WT or *ATG12*$^{-/-}$ cells. **e**, A Venn diagram showing the overlap of the small non-coding RNAs enriched in EVs from WT cells relative to *ATG7*$^{-/-}$ or *ATG12*$^{-/-}$ cells. **f**, The proportion of different classes of small RNAs enriched in EVs from WT versus *ATG*-deficient cells. **g**, A heatmap of the 67 snoRNAs enriched in EVs from WT cells across all genetic conditions and sample types. The scale indicates intensity, defined as Δ(read counts − mean read count)/s.d. Data are available as source data.

impacts intercellular communication and non-cell autonomous functions in vivo remains an important topic for future study. Overall, our studies expand the repertoire of putative targets of secretory autophagy and define a previously unrecognized mechanism by which the LC3-conjugation machinery specifies cargo loading into a subpopulation of EVs.

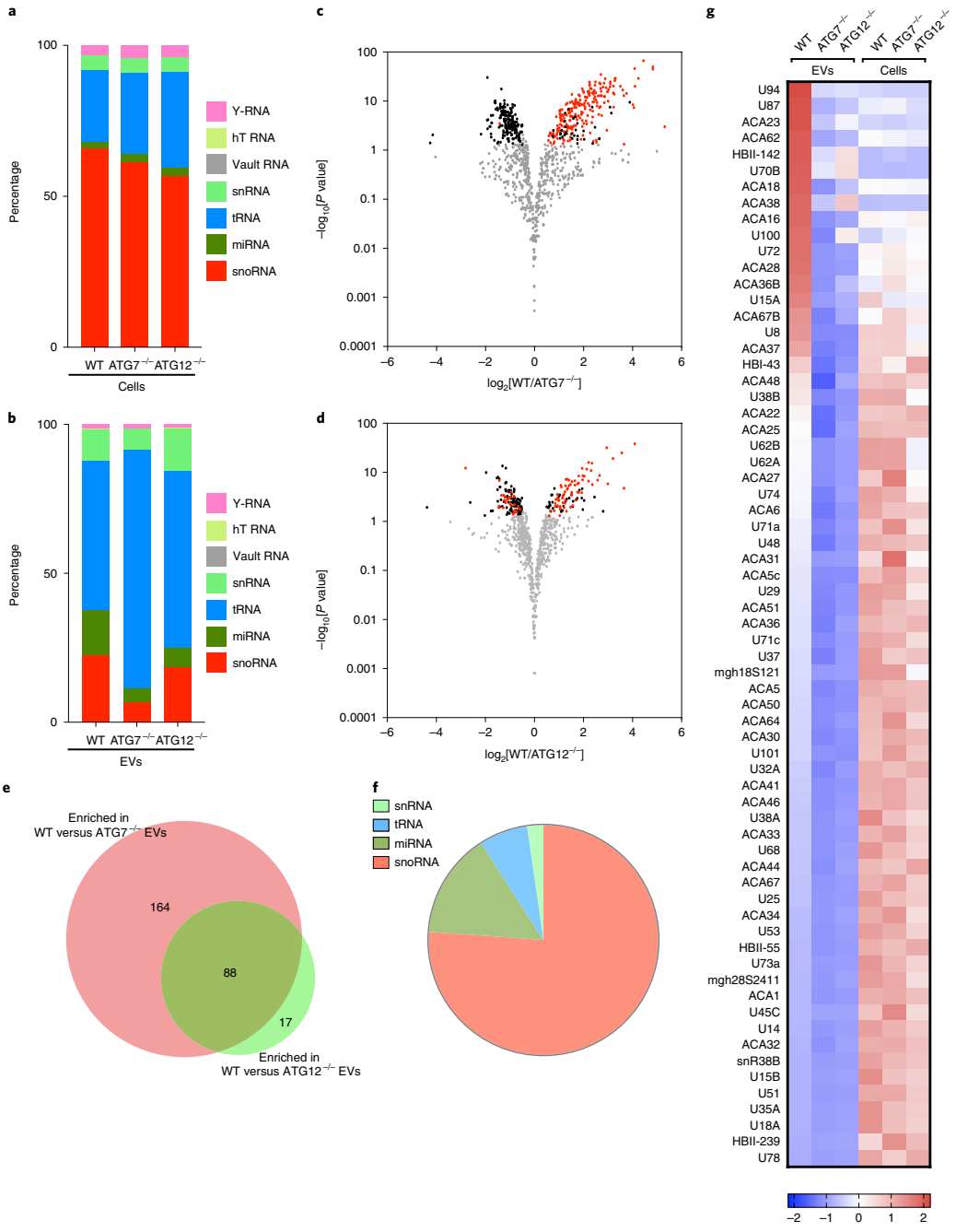

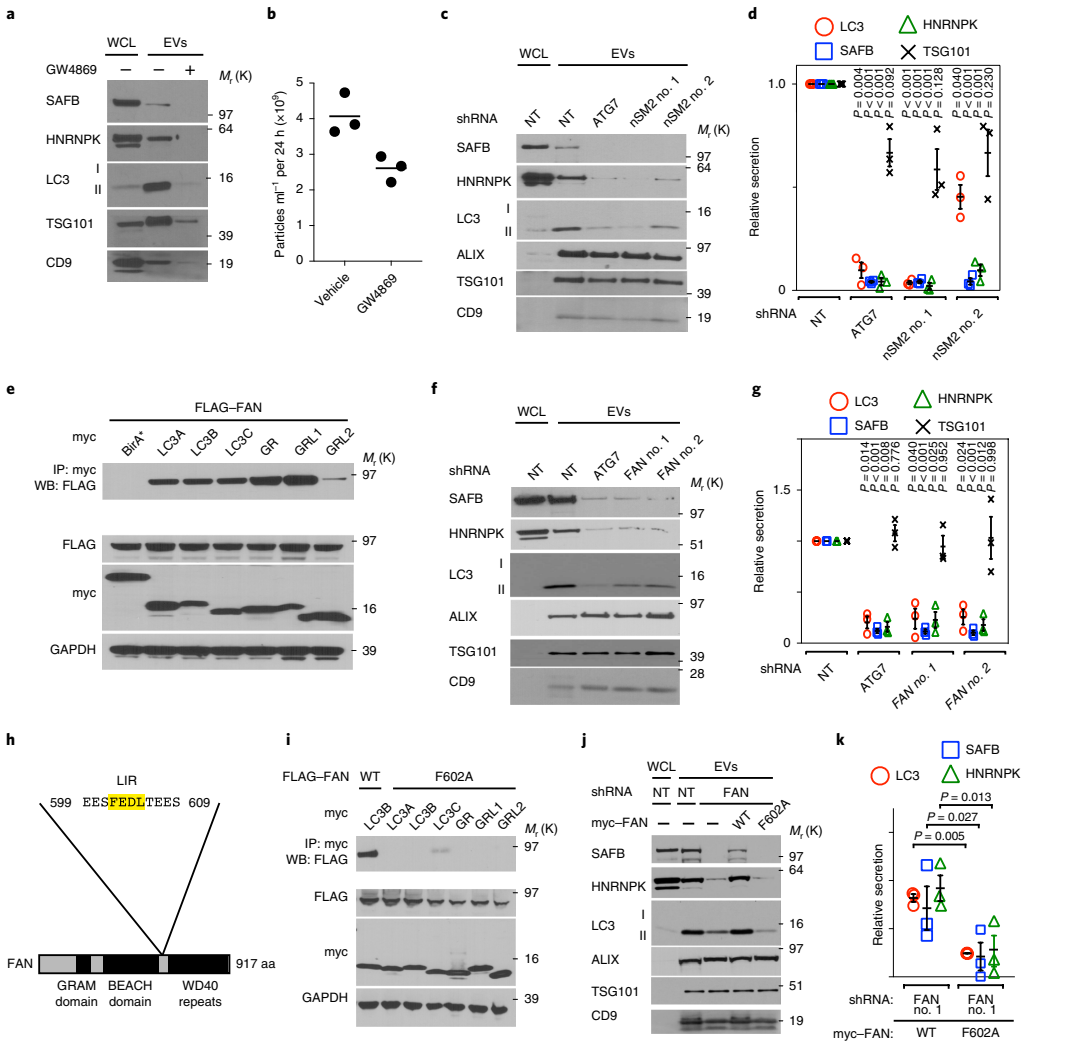

Fig. 7 | LDELS requires nSMase2 and FAN. a, WCL and EV lysates from cells treated in the absence or presence of 5 μM GW4869 for 24 h and immunoblotted for the indicated marker proteins ($n=2$ biologically independent experiments). **b**, Nanoparticle counting for a representative experiment in **a** (line, mean; $n=1$; 3 technical replicates). **c**, WCL and EV lysates collected from equal numbers of HEK293T cells stably expressing non-targeting (NT) shRNA or shRNAs that deplete ATG7 or nSMase2 (nSM2) were immunoblotted for the indicated proteins ($n=3$ biologically independent experiments). **d**, Quantification of the indicated protein levels in the EVs from equal numbers of stable knockdown cells in **c** relative to non-targeting shRNA (mean ± s.e.m.; $n=3$ biologically independent experiments). The statistical significance was calculated by one-way ANOVA coupled with Tukey's post hoc test. **e**, HEK293T cells co-transfected with FLAG-tagged FAN and myc-tagged LC3A, LC3B, LC3C, GABARAP (GR), GABARAPL1 (GRL1), GABARAPL2 (GRL2) or myc–BirA* were lysed, immunoprecipitated with anti-myc antibody and immunoblotted (WB) with the indicated antibodies ($n=2$ biologically independent experiments). **f**, WCL and EV lysates collected from equal numbers of HEK293T cells stably expressing non-targeting shRNA or shRNAs that deplete ATG7 or FAN were immunoblotted for the indicated proteins ($n=3$ biologically independent experiments). **g**, Quantification of the indicated protein levels in the EVs from equal numbers of stable knockdown cells in **c** relative to non-targeting shRNA (mean ± s.e.m.; $n=3$ biologically independent experiments). The statistical significance was calculated by one-way ANOVA coupled with Tukey's post hoc test. **h**, A domain map and the primary LIR in FAN. **i**, Cells co-transfected with FLAG-tagged FAN and myc-tagged LC3A, LC3B, LC3C, GABARAP (GR), GABARAPL1 (GRL1), GABARAPL2 (GRL2) or myc-BirA* were lysed, immunoprecipitated with anti-myc antibody and immunoblotted (WB) with the indicated antibodies ($n=2$ biologically independent experiments). **j**, WCL and EV fractions from cells stably co-expressing non-targeting or shRNA that depletes endogenous FAN along with FLAG-tagged WT FAN or mutant FAN (F602A) were immunoblotted for the indicated markers ($n=2$ biologically independent experiments). **k**, Quantification of the indicated proteins in EVs from equal numbers of FAN knockdown HEK293T cells expressing FLAG-tagged WT FAN versus mutant FAN (F602A) (mean ± s.e.m.; $n=3$ biologically independent experiments). The statistical significance was calculated by a paired two-tailed *t*-test. Data and unprocessed blots are available as source data.

Online content

Any methods, additional references, Nature Research reporting summaries, source data, extended data, supplementary information, acknowledgements, peer review information; details of author contributions and competing interests; and statements of data and code availability are available at https://doi.org/10.1038/s41556-019-0450-y.

Received: 24 January 2019; Accepted: 3 December 2019;
Published online: 13 January 2020

References

1. Kaur, J. & Debnath, J. Autophagy at the crossroads of catabolism and anabolism. *Nat. Rev. Mol. Cell Biol.* **16**, 461–472 (2015).
2. Lock, R., Kenific, C. M., Leidal, A. M., Salas, E. & Debnath, J. Autophagy-dependent production of secreted factors facilitates oncogenic RAS-driven invasion. *Cancer Discov.* **4**, 466–479 (2014).
3. Bel, S. et al. Paneth cells secrete lysozyme via secretory autophagy during bacterial infection of the intestine. *Science* **357**, 1047–1052 (2017).
4. DeSelm, C. J. et al. Autophagy proteins regulate the secretory component of osteoclastic bone resorption. *Dev. Cell* **21**, 966–974 (2011).
5. Guo, H. et al. Atg5 disassociates the V_1V_0-ATPase to promote exosome production and tumor metastasis independent of canonical macroautophagy. *Dev. Cell* **43**, 716–730.e7 (2017).
6. Murrow, L., Malhotra, R. & Debnath, J. ATG12-ATG3 interacts with Alix to promote basal autophagic flux and late endosome function. *Nat. Cell Biol.* **17**, 300–310 (2015).
7. Dupont, N. et al. Autophagy-based unconventional secretory pathway for extracellular delivery of IL-1beta. *EMBO J.* **30**, 4701–4711 (2011).
8. Duran, J. M., Anjard, C., Stefan, C., Loomis, W. F. & Malhotra, V. Unconventional secretion of Acb1 is mediated by autophagosomes. *J. Cell Biol.* **188**, 527–536 (2010).
9. Manjithaya, R., Anjard, C., Loomis, W. F. & Subramani, S. Unconventional secretion of *Pichia pastoris* Acb1 is dependent on GRASP protein, peroxisomal functions, and autophagosome formation. *J. Cell Biol.* **188**, 537–546 (2010).
10. Torisu, T. et al. Autophagy regulates endothelial cell processing, maturation and secretion of von Willebrand factor. *Nat. Med.* **19**, 1281–1287 (2013).
11. Cadwell, K. & Debnath, J. Beyond self-eating: the control of nonautophagic functions and signaling pathways by autophagy-related proteins. *J. Cell Biol.* **217**, 813–822 (2018).
12. Malhotra, V. Unconventional protein secretion: an evolving mechanism. *EMBO J.* **32**, 1660–1664 (2013).
13. Ponpuak, M. et al. Secretory autophagy. *Curr. Opin. Cell Biol.* **35**, 106–116 (2015).
14. Roux, K. J., Kim, D. I., Raida, M. & Burke, B. A promiscuous biotin ligase fusion protein identifies proximal and interacting proteins in mammalian cells. *J. Cell Biol.* **196**, 801–810 (2012).
15. Behrends, C., Sowa, M. E., Gygi, S. P. & Harper, J. W. Network organization of the human autophagy system. *Nature* **466**, 68–76 (2010).
16. Nanjappa, V. et al. Plasma Proteome Database as a resource for proteomics research: 2014 update. *Nucleic Acids Res.* **42**, D959–D965 (2014).
17. Szklarczyk, D. et al. STRING v10: protein–protein interaction networks, integrated over the tree of life. *Nucleic Acids Res.* **43**, D447–D452 (2015).
18. Castello, A. et al. Insights into RNA biology from an atlas of mammalian mRNA-binding proteins. *Cell* **149**, 1393–1406 (2012).
19. Thery, C., Amigorena, S., Raposo, G. & Clayton, A. Isolation and characterization of exosomes from cell culture supernatants and biological fluids. *Curr. Protoc. Cell Biol.* **30**, 3.22.1–3.22.29 (2006).
20. Maas, S. L. N., Breakefield, X. O. & Weaver, A. M. Extracellular vesicles: unique intercellular delivery vehicles. *Trends Cell Biol.* **27**, 172–188 (2017).
21. Mathieu, M., Martin-Jaular, L., Lavieu, G. & Thery, C. Specificities of secretion and uptake of exosomes and other extracellular vesicles for cell-to-cell communication. *Nat. Cell Biol.* **21**, 9–17 (2019).
22. Pegtel, D. M. & Gould, S. J. Exosomes. *Annu. Rev. Biochem.* **88**, 487–514 (2019).
23. van Niel, G., D'Angelo, G. & Raposo, G. Shedding light on the cell biology of extracellular vesicles. *Nat. Rev. Mol. Cell Biol.* **19**, 213–228 (2018).
24. Martell, J. D., Deerinck, T. J., Lam, S. S., Ellisman, M. H. & Ting, A. Y. Electron microscopy using the genetically encoded APEX2 tag in cultured mammalian cells. *Nat. Protoc.* **12**, 1792–1816 (2017).
25. Stenmark, H. et al. Inhibition of rab5 GTPase activity stimulates membrane fusion in endocytosis. *EMBO J.* **13**, 1287–1296 (1994).
26. Trajkovic, K. et al. Ceramide triggers budding of exosome vesicles into multivesicular endosomes. *Science* **319**, 1244–1247 (2008).
27. Ichimura, Y. et al. A ubiquitin-like system mediates protein lipidation. *Nature* **408**, 488–492 (2000).
28. Itakura, E., Kishi, C., Inoue, K. & Mizushima, N. Beclin 1 forms two distinct phosphatidylinositol 3-kinase complexes with mammalian Atg14 and UVRAG. *Mol. Biol. Cell* **19**, 5360–5372 (2008).
29. Matsunaga, K. et al. Two Beclin 1-binding proteins, Atg14L and Rubicon, reciprocally regulate autophagy at different stages. *Nat. Cell Biol.* **11**, 385–396 (2009).
30. Ivanov, P., Kedersha, N. & Anderson, P. Stress granules and processing bodies in translational control. *Cold Spring Harb. Perspect. Biol.* **11**, a032813 (2019).
31. Jeppesen, D. K. et al. Reassessment of exosome composition. *Cell* **177**, 428–445.e18 (2019).
32. Stolz, A., Ernst, A. & Dikic, I. Cargo recognition and trafficking in selective autophagy. *Nat. Cell Biol.* **16**, 495–501 (2014).
33. Kishi-Itakura, C., Koyama-Honda, I., Itakura, E. & Mizushima, N. Ultrastructural analysis of autophagosome organization using mammalian autophagy-deficient cells. *J. Cell Sci.* **127**, 4089–4102 (2014).
34. Zhang, H. et al. Identification of distinct nanoparticles and subsets of extracellular vesicles by asymmetric flow field-flow fractionation. *Nat. Cell Biol.* **20**, 332–343 (2018).
35. Villarroya-Beltri, C., Baixauli, F., Gutierrez-Vazquez, C., Sanchez-Madrid, F. & Mittelbrunn, M. Sorting it out: regulation of exosome loading. *Semin. Cancer Biol.* **28**, 3–13 (2014).
36. Dupuis-Sandoval, F., Poirier, M. & Scott, M. S. The emerging landscape of small nucleolar RNAs in cell biology. *Wiley Interdiscip. Rev. RNA* **6**, 381–397 (2015).
37. Adam-Klages, S. et al. FAN, a novel WD-repeat protein, couples the p55 TNF-receptor to neutral sphingomyelinase. *Cell* **86**, 937–947 (1996).
38. Berg, T. O., Fengsrud, M., Stromhaug, P. E., Berg, T. & Seglen, P. O. Isolation and characterization of rat liver amphisomes. Evidence for fusion of autophagosomes with both early and late endosomes. *J. Biol. Chem.* **273**, 21883–21892 (1998).
39. Fader, C. M., Sanchez, D., Furlan, M. & Colombo, M. I. Induction of autophagy promotes fusion of multivesicular bodies with autophagic vacuoles in k562 cells. *Traffic* **9**, 230–250 (2008).
40. Florey, O., Kim, S. E., Sandoval, C. P., Haynes, C. M. & Overholtzer, M. Autophagy machinery mediates macroendocytic processing and entotic cell death by targeting single membranes. *Nat. Cell Biol.* **13**, 1335–1343 (2011).
41. Heckmann, B. L. et al. LC3-associated endocytosis facilitates beta-amyloid clearance and mitigates neurodegeneration in murine Alzheimer's disease. *Cell* **178**, 536–551.e14 (2019).
42. Mejlvang, J. et al. Starvation induces rapid degradation of selective autophagy receptors by endosomal microautophagy. *J. Cell Biol.* **217**, 3640–3655 (2018).
43. Puri, C. et al. The RAB11A-positive compartment is a primary platform for autophagosome assembly mediated by WIPI2 recognition of PI3P-RAB11A. *Dev. Cell* **45**, 114–131 e118 (2018).
44. Progida, C. & Bakke, O. Bidirectional traffic between the Golgi and the endosomes - machineries and regulation. *J. Cell Sci.* **129**, 3971–3982 (2016).
45. Raiborg, C., Wenzel, E. M. & Stenmark, H. ER-endosome contact sites: molecular compositions and functions. *EMBO J.* **34**, 1848–1858 (2015).
46. Hubstenberger, A. et al. P-body purification reveals the condensation of repressed mRNA regulons. *Mol. Cell* **68**, 144–157.e5 (2017).
47. Jain, S. et al. ATPase-modulated stress granules contain a diverse proteome and substructure. *Cell* **164**, 487–498 (2016).
48. Buchan, J. R., Kolaitis, R. M., Taylor, J. P. & Parker, R. Eukaryotic stress granules are cleared by autophagy and Cdc48/VCP function. *Cell* **153**, 1461–1474 (2013).
49. Alberti, S., Mateju, D., Mediani, L. & Carra, S. Granulostasis: protein quality control of RNP granules. *Front. Mol. Neurosci.* **10**, 84 (2017).
50. Ganassi, M. et al. A surveillance function of the HSPB8-BAG3-HSP70 chaperone complex ensures stress granule integrity and dynamism. *Mol. Cell* **63**, 796–810 (2016).
51. Mateju, D. et al. An aberrant phase transition of stress granules triggered by misfolded protein and prevented by chaperone function. *EMBO J.* **36**, 1669–1687 (2017).
52. Wang, B. et al. ULK1 and ULK2 regulate stress granule disassembly through phosphorylation and activation of VCP/p97. *Mol. Cell* **74**, 742–757.E8 (2019).
53. Abels, E. R. & Breakefield, X. O. Introduction to extracellular vesicles: biogenesis, RNA cargo selection, content, release, and uptake. *Cell. Mol. Neurobiol.* **36**, 301–312 (2016).
54. Skog, J. et al. Glioblastoma microvesicles transport RNA and proteins that promote tumour growth and provide diagnostic biomarkers. *Nat. Cell Biol.* **10**, 1470–1476 (2008).
55. Spinelli, C., Adnani, L., Choi, D. & Rak, J. Extracellular vesicles as conduits of non-coding RNA emission and intercellular transfer in brain tumors. *Noncoding RNA* **5**, 1 (2018).
56. Valadi, H. et al. Exosome-mediated transfer of mRNAs and microRNAs is a novel mechanism of genetic exchange between cells. *Nat. Cell Biol.* **9**, 654–659 (2007).
57. Bellingham, S. A., Coleman, B. M. & Hill, A. F. Small RNA deep sequencing reveals a distinct miRNA signature released in exosomes from prion-infected neuronal cells. *Nucleic Acids Res.* **40**, 10937–10949 (2012).

58. Freedman, J. E. et al. Diverse human extracellular RNAs are widely detected in human plasma. *Nat. Commun.* **7**, 11106 (2016).
59. Kaur, S. et al. CD63, MHC class 1, and CD47 identify subsets of extracellular vesicles containing distinct populations of noncoding RNAs. *Sci. Rep.* **8**, 2577 (2018).
60. Lasser, C. et al. Two distinct extracellular RNA signatures released by a single cell type identified by microarray and next-generation sequencing. *RNA Biol.* **14**, 58–72 (2017).
61. Lefebvre, F. A. et al. Comparative transcriptomic analysis of human and *Drosophila* extracellular vesicles. *Sci. Rep.* **6**, 27680 (2016).
62. Rimer, J. M. et al. Long-range function of secreted small nucleolar RNAs that direct 2′-*O*-methylation. *J. Biol. Chem.* **293**, 13284–13296 (2018).
63. Shurtleff, M. J. et al. Broad role for YBX1 in defining the small noncoding RNA composition of exosomes. *Proc. Natl Acad. Sci. USA* **114**, E8987–E8995 (2017).
64. Hong, E. et al. Unravelling the RNA-binding properties of SAFB proteins in breast cancer cells. *Biomed. Res. Int.* **2015**, 395816 (2015).
65. Falaleeva, M. & Stamm, S. Processing of snoRNAs as a new source of regulatory non-coding RNAs: snoRNA fragments form a new class of functional RNAs. *Bioessays* **35**, 46–54 (2013).
66. Holley, C. L. et al. Cytosolic accumulation of small nucleolar RNAs (snoRNAs) is dynamically regulated by NADPH oxidase. *J. Biol. Chem.* **290**, 11741–11748 (2015).
67. Li, M. W. et al. Nuclear export factor 3 regulates localization of small nucleolar RNAs. *J. Biol. Chem.* **292**, 20228–20239 (2017).

Methods

Cell culture. HEK293T cells (ATCC, CRL-3216), including all cell derivatives generated in this study, were cultured in DMEM (Thermo Fisher, 11995065) supplemented with 10% fetal bovine serum (FBS), 25 mM HEPES, 100 U ml^{-1} penicillin and 100 µg ml^{-1} streptomycin (Thermo Fisher, 15140163). Murine RAW 264.7 macrophages and murine B16F10 were gifts from M. Krummel (UCSF) and were cultured in DMEM (Thermo Fisher, 11995065) supplemented with 10% FBS, 25 mM HEPES, penicillin and streptomycin. Murine LLC1 cells were purchased from ATCC (CRL-1642) and were cultured in DMEM (Thermo Fisher, 11995065) supplemented with 10% FBS, 25 mM HEPES, penicillin and streptomycin. All cell lines were authenticated using STR profiling (IDEXX BioResearch) and routinely tested for mycoplasma contamination (Sigma, MP0025).

To induce biotin-labelling, HEK293T cells expressing myc–BirA* or myc–BirA*–LC3B were incubated with 50 µM biotin in DMEM with all supplements except FBS for 24 h. Unless indicated, CM and EV preparations were collected following 24 h incubation in DMEM containing all supplements except FBS. For autophagy flux assays, cells were incubated with 50 µM chloroquine (Sigma, C6628) or 50 µM bafilomycin A1 (Sigma, B1793) as indicated for 1 h before lysis. Treatment with 5 µM GW4869 (Cayman, 13127) or vehicle (dimethylsulfoxide, Sigma) in serum-free DMEM for 24 h was used to inhibit nSMase activity.

Plasmid constructs. The following plasmids were obtained or are available from Addgene: pcDNA3.1-myc-BirA* (mycBioID; Addgene no. 35700), pBABE-GFP-LC3B (Addgene no. 22405), pBABE-HRas^{V12} (Addgene no. 9051), mCherry-Rab5Q79L (Addgene no. 35138). Human LC3B (NM_022818.4), SAFB (NM_001201338.1), HNRNPK (NM_002140.4), LC3A (NM_032514.3), LC3C (NM_001004343.2), GABARAP (NM_007278.1), GABARAPL1 (NM_031412.2), GABARAPL2 (NM_007285.6), SF3A1 (NM_005877.5), LARP1 (NM_015315.4), G3BP1 (NM_005754) and FAN (NM_003580.3) were subcloned from mRNA isolated from human cell lines that was reverse transcribed using AccuScript High Fidelity Reverse Transcriptase (Agilent) and complementary DNA amplified using PfuUltra II Hot Start DNA polymerase and gene-specific primers (LC3B Fwd: agtcggatccatgccgtcggagaagacct; LC3B Rev: gactctcgagttacactgacaatttcatcccg; SAFB Fwd: agctggatccatggcggagactctgtcag; SAFB Rev: agctgtcgactcagtagcggcgagtgaag; HNRNPK Fwd: agtcggaattcgcatggaaactgaacagccagaag; HNRNPK Rev: agtcctcgagttagaatccttcaacatctgcata; LC3A Fwd: agtcggatccatgccctcagaccggcct; LC3A Rev: gactctcgagtcagaagccgaaggtttcct; LC3C Fwd: agtcggatccatgccgcctccacagaaaat; LC3C Rev: gactctcgagctagagaggattgcagggtc; GABARAP Fwd: agtcggatccatgaagttcgtgtacaaagaaga; GABARAP Rev: gactctcgagtt aaagaccgtagacactttc; GABARAPL1 Fwd: agtcggatccatgaagttccagtacaaggac; GABARAPL1 Rev: gactctcgagtcatttcccatagacactctc; GABARAPL2 Fwd: agtcagatctatgaagtggatgttcaaggag; GABARAPL2 Rev: gactctcgagtcagaagcc aaaagtgttctc; SF3A1 Fwd: agtctgatcaatgccggccggacccgtg; SF3A1 Rev: gatcctcgagctacttcttcctcccgcctc; LARP1 Fwd: agctagatctatgctttggagggtgcttttg; LARP1 Rev: agctctcgagtcactttcccaaagtctgtgt; G3BP1 Fwd: agctggatccatggtgatggagaagcctagt; G3BP1 Rev: agctgtcgactcactgccgtggcgcaagc; FAN Fwd: agcttgatcaatggcgtttatccg gaagaag; FAN Rev: agctctcgagttaatactgcaatttccagaatata). Subsequently, the cDNAs were subcloned into pcDNA3 between the BamHI and XhoI or EcoRI and XhoI restriction sites downstream of an N-terminal myc-tag or 3×Flag-tag. All constructs were verified by sequencing.

To generate pBABE-myc-BirA*, myc–BirA* was amplified with flanking primers (Fwd: agctaagcttaccggtgccaccatggaacaaaaactc; Rev: gactctcgagttacttctctgcgcttctcagg) from pcDNA3.1-myc-BirA* and sub-cloned into pBABE-GFP-LC3 between AgeI and SalI, entirely replacing the GFP–LC3 open reading frame. To generate pBABE-myc-BirA*-LC3, myc–BirA* was amplified with flanking primers (Fwd: agctaagcttaccggtgccaccatggaacaaaaactc; Rev: gactggatcccttctctgcgcttctcagg) from pcDNA3.1-myc-BirA* and sub-cloned into the HindIII and BamHI sites in front of pcDNA3-FLAG-LC3, replacing the FLAG sequence. Subsequently, the myc–BirA*–LC3 fragment was sub-cloned from pcDNA3-myc-BirA*–LC3 using AgeI (introduced 3′ to the HindIII site) and XhoI into pBABE-GFP-LC3 between AgeI and SalI, replacing the GFP–LC3 open reading frame. All constructs were verified by sequencing.

Site-directed mutagenesis of FLAG-tagged SAFB and FAN was performed via QuikChange PCR. Overlapping primers carrying the desired mutation (SAFB Fwd: ttagatacttca tcatctgacgccactatattacaggaaattgaa; SAFB Rev: ttagatacttcatcatctgacgccactatattacaggaaattgaa; FAN Fwd: gattccccaggtgaagagtctgccgaagacctgaccgaagaaagc; FAN Rev: gctttcttcggtcaggtcttcggcagactcttcacctgggggaatc) were used to amplify pcDNA3 FLAG–SAFB and FLAG–FAN, respectively, and template plasmid was eliminated via DpnI digestion. Subsequently, individual clones were sequenced to verify mutagenesis of the desired sites. Finally, for FAN rescue experiments, WT FAN and FAN F602A were amplified with primers incorporating an N-terminal myc-tag (myc–FAN/F602A Fwd: agcttgatcaaccatggaacaaaaactttatttctgaagaggatctgggctccatggcgttt atccggaagaag; Rev: agctctcgagttaatactgcaatttccagaatata) and cloned between the BamHI and XhoI of pLenti-CMV-blast (Addgene: no. 17486).

Retroviral and lentiviral packaging, infection and selection. Retroviral pBABE expression vectors were packaged and target cells were transduced according to established protocols[68]. Briefly, Phoenix-AMPHO cells (gift from C. McCormick, Dalhousie University) were seeded and transfected with retroviral vectors using polyethylenimine. Virus-containing CM was collected 2 d after transfection and clarified using a 0.45-µM filter. Before infection, virus-containing medium was diluted 1:4 in DMEM growth medium and the mix was supplemented with Polybrene to a final concentration of 8 µg ml^{-1}. Subsequently, the viral transduction mix (5 ml total volume/10 cm culture dish) was incubated with HEK293T cells for 24 h. Cells were selected 24 h post-transduction with 1 µg ml^{-1} puromycin for 2 d. To package lentivirus, HEK293T cells were seeded and co-transfected with the packaging vectors psPAX2 and pMD2.G, and individual pLKO.1 transfer vectors. Virus collection, infection and puromycin selection of stable cell pools were carried out as above.

SILAC, proximity-dependent biotinylation and affinity purification of biotin-labelled secretome. For experimental replicates no. 1 and no. 2, HEK293T cells stably expressing myc–BirA* were grown in Lys- and Arg-free DMEM supplemented with 10% dialysed FBS (Thermo Fisher), 25 mM HEPES, penicillin/streptomycin, and light (K0) lysine (50 µg ml^{-1}) and light (R0) arginine (50 µg ml^{-1}), whereas HEK293T cells stably expressing myc–BirA*–LC3 were grown in lysine- and arginine-free DMEM medium with supplements and the heavy isotopes K8 lysine (Cambridge Isotopes) and R10 arginine (Cambridge Isotopes). For experimental replicate no. 3, a label swap was performed to rule out potential labelling artefacts; the heavy and light labelling was reversed between myc–BirA* and myc–BirA*–LC3 cells. Cells were labelled in SILAC medium and expanded into 18×15 cm culture dishes of equal cell density (80% confluent).

Cells were gently washed twice in 20 ml EBSS and incubated with 15 ml serum-free SILAC medium supplemented with 50 µM biotin to trigger biotin labelling according to standard protocols[14]. CM was collected 24 h later and centrifuged serially at 200*g* for 10 min to pellet cells, followed by 2,000*g* for 20 min to pellet cellular debris and apoptotic bodies. CM was routinely stored at −80 °C before analysis. CM was precipitated by adding trichloroacetic acid (TCA) to a final concentration of 15% and incubating on ice for 1 h. Subsequently, precipitated protein was pelleted by ultracentrifugation at 200,000*g* for 18 h. Pellets were washed with 10 ml of ice-cold acetone, re-centrifuged at 200,000*g* for 1 h and air-dried. To solubilize protein, pellets were resuspended in 8 M guanidine hydrochloride (Sigma G3272), 100 mM Tris hydrochloride pH 8.0 for 1 h with manual trituration every 15 min. Re-solubilized protein from myc–BirA* or myc–BirA*–LC3 was pooled separately and protein concentrations were quantified via BCA protein assays (Thermo Fisher, 23225), diluting samples below BCA threshold limits for chaotropic agents. Subsequently, samples from light myc–BirA* and heavy myc–BirA*–LC3 were mixed in equal protein proportions and the combined sample was diluted to 2.5 mM guanidine hydrochloride with 50 mM Tris pH 8.0. Biotin-labelled proteins were captured on 120 µl of packed high-capacity neutravidin Sepharose (Thermo Fisher, 29204) overnight at 4 °C, followed by 3 washes with 5 ml 2.5 mM guanidine hydrochloride, 50 mM Tris HCl pH 8.0 before analysis by immunoblotting or MS.

Sample preparation, LC–MS/MS, peptide identification and protein quantification for MS of affinity-purified proteins. Neutravidin Sepharose- and affinity-purified proteins were resuspended and mildly denatured in 1 M guanidine hydrochloride, 1 mM calcium chloride and 100 mM Tris buffer pH 8.0. Disulfide bonds were reduced with 4 mM tris(2-carboxyethyl)phosphine (Sigma, C4706), and free thiols were alkylated with 10 mM iodoacetamide (Sigma, I1149). Subsequently, 10 µg of MS-grade trypsin (Thermo Fisher) dissolved in 10 µl 50 mM acetic acid was added to proteins on beads, and incubated at 37 °C for at least 18 h. The eluate was transferred to a new tube, acidified to a final concentration of 0.3% trifluoroacetic acid (TFA; pH < 3) and desalted by a reversed-phase C18 solid-phase extraction (SPE) cartridge, using either a Sep-pak (Waters Corp.) or SOLA SPE (Thermo Fisher), and then dried down in a speed-vac. Dried peptides were stored at −20 °C, and resuspended in 2% acetonitrile (ACN), 0.1% formic acid (FA) in a bath sonicator for 5 min to a concentration of 2 µg µl^{-1} before MS analysis.

Peptides (0.5–1 µg) were submitted for nano-LC–electrospray ionization–MS/MS, using a 195-min reversed-phase (2.4–32% ACN, 0.1–0.08% FA) buffer gradient with a 15-cm Acclaim PepMap 100 C18 analytical column (2-µm beads, 75 µm i.d.), running at 200 nl min^{-1} on a Dionex Ultimate 3000 RSLCnano pump, in-line with a hybrid quadrupole–Orbitrap Q-Exactive Plus mass spectrometer (Thermo Fisher). A data-dependent method with a parent ion scan at a resolving power of 70,000 was run on each sample and a top 12 method for replicates 1 and 2 and a top 15 method for replicate 3 were selected for the 12 and 15 most intense peaks for MS/MS using HCD fragmentation (normalized collision energy 27), respectively. Dynamic exclusion was activated such that parent ions were excluded from MS/MS fragmentation for 20 s after initial selection.

For protein identification and quantification, Thermo.RAW files were analysed by Maxquant[69]. The recorded spectra from three independent biological replicates were searched against the human reference proteome from UniProt (2014-11-16 release, with 20,193 unique proteins, including isoforms, on SwissProt and 47,673 entries in TrEMBL) using MaxQuant, version 1.5.1.2. Maxquant uses the Andromeda search engine to identify peptides. The search parameters allowed for a 4.5-ppm peptide ion search tolerance, a 7.5-ppm centroided

fragment ion tolerance and 2 missed tryptic cleavages. Oxidation of methionine, phosphorylation of serine/threonine/tyrosine and N-terminal acetylation were allowed as variable modifications, while carbamidomethylation of cysteines was selected as a constant modification and a threshold peptide spectrum match false discovery rate (FDR) and protein FDR of 1% was allowed. Quantification of SILAC ratios was performed by Maxquant on the MS1 level and the resulting ratios for all replicates were compared using statistical tools found in the Perseus bioinformatics analysis package[70]. Proteins with ratio quantification in only one replicate were filtered out. The statistical significance was determined by applying a one-sample Student *t*-test to the replicates with a *P*-value cutoff of $P = 0.05$. Protein group ratios and *P* values are included in Supplementary Table 1.

EV preparation and characterization. EVs were purified according to standard differential centrifugation protocols[19]. Briefly, cells seeded in 15-cm culture dishes at approximately 70% confluence were incubated with serum-free DMEM for 24 h. CM was collected and centrifuged serially at 200*g* for 10 min to pellet cells, 2,000*g* for 20 min to pellet cellular debris and apoptotic bodies, 10,000*g* for 30 min to pellet large EVs, and 100,000*g* in an ultracentrifuge for 2 h to pellet EVs. Crude EVs pellets were then gently triturated in PBS using a P1000 pipette, diluted further in PBS (12 ml), and ultracentrifuged for an additional 70 min at 100,000*g* to generate EV preparations for further analysis as described below. Importantly, for all comparisons of EVs between experimental conditions, results from individual cohorts were corrected as indicated on the basis of total cell number or WCL protein concentration to ensure that EV or EV protein quantification was not confounded by seeding differences.

Sucrose density gradient separation was utilized to generate highly purified EV preparations and to analyse the co-fractionation of LC3-II and LC3-binding proteins with EV marker proteins on linear sucrose gradients. Briefly, the 100,000*g* EV pellets generated via differential centrifugation as described above were thoroughly resuspended in 100 µl 10% sucrose solution and gently layered onto a continuous 10–60% sucrose gradient formed on a gradient station (BioComp Instruments) and then ultracentrifuged at 210,000*g* for 18 h. Subsequently, 1 ml fractions from the gradient were top unloaded, weighed and diluted in 10 ml of PBS. The diluted fractions were spun at 100,000*g* for 70 min and the pellets were resuspended in urea lysis buffer for analysis by immunoblotting.

For protease protection assays, equal amounts of EVs were resuspended in PBS or PBS containing 1% Triton X-100 in the absence or presence of 100 µg ml^{-1} trypsin for 30 min at 4 °C. Subsequently, the reactions were stopped by the addition of 2× protein sample buffer and the lysates were subjected to immunoblotting. Established protocols were used to perform TEM of HEK293T EVs prepared by differential centrifugation[5].

Nanoparticle tracking analysis for EV preparations was performed with an LM10 nanoparticle analyser (NanoSight). The camera level was set at 9 for all recordings. The camera focus was adjusted to make the particles appear as individual dots with surrounding refractory rings. Five 60-s videos were recorded for each sample with a delay of 10 s between each recording. All post-acquisition functions were set at automatic, with the exception of the detection threshold, which was set to 2. The protein content in EV pellets was quantified via BCA assay (Thermo Fisher, 23225), diluting samples below the threshold limits for interfering detergents and chaotropic agents.

Sample preparation, TMT labelling, LC–MS/MS, peptide identification and protein quantification for MS of EV proteins. Serum-free medium conditioned for 24 h from four bioreplicates of approximately 5×10^9 WT, *ATG7*$^{-/-}$ and *ATG12*$^{-/-}$ HEK293T cells was collected and EVs were isolated using the standard differential centrifugation protocols described above. On purification, EVs from each condition were lysed in 800 µl of radioimmunoprecipitation buffer (25 mM Tris HCl pH 7.6, 150 mM NaCl, 1% NP-40, 1% sodium deoxycholate, 0.1% SDS), supplemented with 2% SDS and sonicated with a probe sonicator set to an amplitude of 8 for 10 bursts of 10 s. Each 800 µl sample was then diluted in 3.5 ml ice-cold 100% acetone and incubated at −20 °C for 12 h. Subsequently, the samples were spun in an ultracentrifuge at 200,000*g* for 18 h, the acetone was decanted and the pelleted protein was left to air dry. Dried pellets were stored at −80 °C before solubilization and TMT labelling.

Biological replicates of HEK293T WT, *ATG7*$^{-/-}$ and *ATG12*$^{-/-}$ precipitated EV proteins were resuspended in 30 µl 6 M guanidine chloride, 100 mM Tris pH 8.0, 10 mM TCEP, 40 mM 2-chloroacetamide (CAA). Proteins were denatured for 1 h at 37 °C and quantified with 660 nm Protein Assay Reagent (Thermo). The 4 bioreplicates from each condition were pooled into 2 separate samples and subsequently diluted sixfold with 150 µl 100 mM Tris pH 8.0. Two hundred micrograms of protein for each sample was trypsinized with 4 µg trypsin (Thermo) in an orbital shaker at 250 r.p.m., 37 °C for ~20 h. After 20 h, trypsin digestion was stopped by acidifying samples with 10% TFA to a final concentration of 0.5% TFA, and then desalting with SOLA C18 reverse-phase SPE columns (Thermo), where the samples were washed with 1.5 ml 0.1% TFA, then 0.5 ml 0.1% FA, 2% ACN, and eluted with 450 µl 0.1% FA, 50% ACN. These samples were dried by speed-vac, then resuspended in 10 µl 50 mM HEPES (pH 8.5) and quantified by a peptide quantification kit (Thermo).

For TMT labelling, 800 µg of each TMT six-plex (Thermo no. 90061) isobaric compound was resuspended with 41 µl 100% anhydrous ACN (Sigma). A 15 µg quantity of peptides for each replicate was individually combined with 7.69 µl (or 150 µg) of the TMT isobaric tags. Samples were incubated at 25 °C for 1 h, and then the reaction was quenched with 8 µl 5% hydroxylamine for 15 min. After labelling, the six individually labelled samples were pooled and 1/3 of the pooled sample (30 µg) was fractionated by high-pH reverse-phase fractionation into 8 fractions and dried down by speed-vac. The fractions were then resuspended in 0.1% FA, 2% ACN before LC–MS/MS analysis.

For LC–MS/MS analysis, 1 µg TMT-labelled peptides were analysed on a 15-cm C18 analytical column, in-line with a Q-Exactive Plus mass spectrometer. The peptides were separated on a multi-slope, 100 min gradient (6.4%–27.2% ACN with 0.1% FA for 80 min at 0.2 µl min^{-1}, then 27.2%–40% ACN with 0.09% FA for 15 min at 0.3 µl min^{-1}, then 40%–56% ACN with 0.09% FA for 5 min at 0.3 µl min^{-1}, and then washed for 3 min). Data-dependent acquisition with MS1 resolution of 70,000, top15 method, and HCD normalized collision energy of 32 was used, with MS2 resolution of 35,000 and an isolation window of 0.7 *m*/*z*. Dynamic exclusion was activated for 30 s after initial parent ion selection.

Eight injections of the different fractions of TMT-labelled exosome peptides were analysed together via Maxquant (v1.6.0.16). The search parameters included a peptide search tolerance of 4.5 ppm, a centroided MS2 tolerance of 7.5 ppm, and allowed for two missed tryptic cleavages. Constant modification of carbamidomethylation of cysteines and variable modifications of N-terminal acetylation, methionine oxidation and serine/threonine/tyrosine phosphorylation were allowed. Peptide spectrum match FDR and protein FDR was set at 1%. Match between runs was enabled to increase peptide identifications. Type is set to 'Reporter ion MS2', and TMT6plex-Nter126 to 131, TMT6plex-Lys126 to 131 labels are selected. The resulting quantifications are then median normalized for each protein group and statistical analysis (two-sample two-sided *t*-test) was applied in Perseus, with a statistical significance threshold of $P < 0.05$.

Isolation and sequencing of small and large RNA species in EVs. Serum-free medium conditioned for 24 h from 4.5×10^8 WT, *ATG7*$^{-/-}$ and *ATG12*$^{-/-}$ HEK293T cells was collected and EVs were isolated according to the standard differential centrifugation protocols described above. Small and large RNA was isolated from EVs and cells using the Macherey-Nagel NucleoSpin kit (no. 740971) according to the manufacturer's protocol.

Short RNA libraries were prepared using the SMARTer smRNA-Seq Kit for Illumina (Takara no. 635030). Briefly, input RNA from three bio-replicates of WT, *ATG7*$^{-/-}$ and *ATG12*$^{-/-}$ cells and EV RNA samples was first polyadenylated and then reverse transcribed using Primescript Reverse Transcriptase and oligo(dT) and SMART smRNA oligonucleotides. Subsequently, primers with unique Illumina i5 and i7 adapter sequences were used to PCR amplify the cDNA from the different samples for 12 cycles. Libraries were then subjected to size selection to enrich for small RNA species using SPRI AMPure Beads (Beckman Coulter, no. A63880) and the yield and concentration were assessed using a Qubit 2.0 Fluorometer (Invitrogen) and DNA 1000 chips on an Agilent 2100 Bioanalyzer (Applied Biosystems), respectively. Libraries were then diluted to 8 nM and pooled together.

Large RNA libraries were prepared using the SMARTer Stranded Total RNA Sample Prep Kit - HI (Takara no. 634875). Input RNA from three bio-replicates of WT, *ATG7*$^{-/-}$ and *ATG12*$^{-/-}$ cells and EV RNA samples was depleted of ribosomal RNA, chemically fragmented and then reverse transcribed using Primescript Reverse Transcriptase, random primers and SMART stranded oligonucleotides. The cDNA was then purified using SPRI AMPure Beads (Beckman Coulter, no. A63880). Subsequently, primers with unique Illumina i5 and i7 adapter sequences were used to PCR amplify the cDNA from the different samples for 22 cycles. Libraries were then purified using SPRI AMPure Beads (Beckman Coulter, no. A63880) and the yield and concentration were assessed using a Qubit 2.0 Fluorometer (Invitrogen) and DNA 1000 chips on an Agilent 2100 Bioanalyzer (Applied Biosystems), respectively.

Each library was diluted to a final concentration of 4.2 nM and pooled before single-end, 50-base-pair sequencing on two separate lanes of a HiSeq 4000 sequencer (UCSF Center for Advanced Technology, San Francisco, CA). For small RNAs, raw reads were first trimmed using cutadapt (v2.3) by removing the polyA tail and the tri-nucleotide template switch. Trimmed reads were then mapped to the human reference genome (GRCh38/hg38) using bowtie2 (v2.3). Bedtools (intersectBed) was used to count the number of reads that overlap annotated small RNA species (DASHRv2.0[71]). Differential expression analysis was performed using DESeq2. For RNA-seq, salmon (v0.14) was used to map reads to the human transcriptome (Gencode v28). Tximport was used to import the data into R and DESeq2 was then used to perform differential gene expression analysis.

Bioinformatic analyses. Candidate proteins identified by MS of the BirA*–LC3-labelled secretome were subdivided into class I proteins, which were significantly enriched ($\log_2$(BirA*–LC3/BirA*) > 1) in the three quantitative MS bioreplicates, and class II proteins, which were enriched in two out of three biological replicates. Unless indicated, higher stringency class I and lower stringency class II datasets were combined to generate the BirA*–LC3-labelled secretome for all bioinformatic analyses. The proportion of candidates detected in human plasma was established by searching the BirA*–LC3-labelled secretome against the Plasma Proteome Database[16]. GO analysis was performed using protein analysis through

evolutionary relationships (PANTHER) and the top 10 terms for molecular function and cellular component were plotted according to their $-\log_{10}$ FDR[72]. The network map of the BirA*–LC3-labelled secretome was plotted with Search Tool for the Retrieval of Interacting Genes/Proteins (STRING) using experiments and databases for interaction sources with a minimum interaction confidence score of 0.400 (ref. [73]). Extracellular exosome and RBPs within the network were identified using PANTHER GO analyses for individual candidates. The number of candidate proteins associated with the GO term extracellular exosome was obtained using PANTHER. The top ten proteins with the greatest connectivity to the combined class I and class II data were identified using the protein–protein interaction tool in the Enrichr gene set enrichment analysis suite and plotted according to their adjusted *P* values[74]. Overlap between datasets, including individual Q-MS bioreplicates, LC3 and the broader ATG8 interactome[15] and mRNA-binding proteome[18], was visualized using Biovenn[75].

For TMT Q-MS, the overlap between candidates significantly enriched in EVs from WT versus EVs from *ATG7*$^{-/-}$ and *ATG12*$^{-/-}$ ($P<0.05$; $\log_2$(WT/*ATG7*$^{-/-}$) or (WT/*ATG12*$^{-/-}$)>0.5; $n=2$) and the BirA*–LC3-labelled secretome (classes I and II), as well the *ATG7*- and *ATG12*-dependent EV proteome versus the stress granule[47] and P-body[46] proteomes was visualized using Biovenn[13]. The top ten proteins with the greatest connectivity to the ATG7- and ATG12-dependent EV proteome were identified using the protein–protein interaction tool in the Enrichr gene set enrichment analysis suite and plotted according to their adjusted *P* values[10]. GO analysis of the *ATG7*- and *ATG12*-dependent EV proteome was performed with PANTHER and the top 10 non-redundant terms for molecular function were plotted according to their $-\log_{10}$ FDR[8].

For RNA-seq data, the overlap between RNA candidates significantly enriched in EVs from WT versus EVs from *ATG7*$^{-/-}$ and *ATG12*$^{-/-}$ ($P<0.05$; $\log_2$ WT EV RNA/WT cell RNA versus *ATG7*$^{-/-}$ EV RNA/*ATG7*$^{-/-}$ cell RNA or WT EV RNA/WT cell RNA versus *ATG12*$^{-/-}$ EV RNA/ *ATG12*$^{-/-}$ cell RNA>0.5) was visualized using Biovenn[13]. The classes of different RNA species identified were annotated using metascape[76] and the heatmap of snoRNA species enriched in WT EVs relative to *ATG7*$^{-/-}$ and *ATG12*$^{-/-}$ EVs was plotted using Prism statistical analysis software.

Antibodies. Immunoblotting: Streptavidin–HRP (Thermo Fisher, cat. no. 21130, lot no. TA263511, SB241752A; 1:40,000), rabbit anti-MAP1LC3 (Millipore, cat. no. ABC232; 1:1,000), rabbit anti-myc (Cell Signaling Technology, cat. no. 2278S, clone no. 71D10, lot no. 5; 1:1,000), mouse anti-myc (Sigma, cat. no. M5546, clone no. 9E10, lot no. 128M4898V; 1:1,000), mouse anti-GAPDH (Millipore, cat. no. MAB374, lot no. 3075597; 1:1,000), guinea pig anti-SQSTM1 (also known as p62) (Progen/Cedarlane, cat. no. GP62-C, lot no. 703241-1; 1:1,000), rabbit anti-OPTN (Abcam, cat. no. ab23666, lot no. GR3270251; 1:1,000), goat anti-ATG7 (Santa Cruz Biotechnology, cat. no. sc-8668, clone no. N-20, lot no. B0316; 1:1,000), mouse anti-Nbr1 (Santa Cruz Biotechnology, cat. no. sc-130380, clone no. 4BR, lot no. B2019; 1:1,000), mouse anti-ALIX (Cell Signaling Technology, cat. no. 2171S, clone no. 3A9, lot no. 5; 1:1,000), rabbit anti-Hsc70 (Cell Signaling Technology, cat. no. 8444, clone no. D12F2, lot no. 1; 1:1,000), rabbit anti-TSG101 (BD Biosciences, cat. no. 612696, lot no. 8172853; 1:1,000), mouse anti-CD9 (Millipore, cat. no. CBL162, clone no. MM2-57, lot no. 2691299; 1:1,000), mouse anti-FLAG-M2 (Sigma-Aldrich, cat no. F3165, clone no. M2, lot no. SLBN8915V, SLCC4005, SLBF1225; 1:5,000), rabbit anti-DYKDDDDK (Cell Signaling Technology, cat. no. 2368S, lot no. 12; 1:1,000), rabbit anti-SAFB (Abcam, cat. no. ab187650, clone no. EPR13588, lot no. GR167184-1, GR167184-4, GR167184-5; 1:500), mouse anti-HNRNPK (Abcam, cat. no. ab39975, clone no. 3C2, lot no. GR275360-20, GR275360-6, GR275360-8, GR148352-24; 1:1,000), rabbit anti-ATG12 (Cell Signaling Technology, cat. no. 2010S, clone no. human specific, lot nos. 2, 5; 1:1,000), rabbit anti-ATG14 (MBL, cat. no. PD026, lot no. 5; 1:1,000), rabbit anti-CHMP3 (Abcam, cat. no. ab175930, clone no. EPR12821, lot no. YK032912CS; 1:1,000), rabbit anti-VPS4a (Sigma, cat. no. SAB4200022, lot no. 119K4789; 1:1,000), rabbit anti-VPS4b (Abcam, cat. no. ab102687, lot no. GR60499-4; 1:1,000), rabbit anti-CHMP4b (Abcam, cat. no. ab76334, lot no. GR26679-7; 1:1,000), rabbit anti-FIP200/RB1CC1 (Proteintech, cat. no. 17250-1-AP, lot no./barcode no. 00012978; 1:1,000), rabbit anti-phospho-S6 (Cell Signaling Technology, cat. no. 4858S, D57.2.2E, lot no. 3; 1:1,000), rabbit anti-S6 (Cell Signaling Technology, cat. no. 2217L, clone no. 5G10, lot no. 3; 1:1,000), rabbit anti-nSMase2 (Santa Cruz Biotechnology, cat. no. sc-67305, clone no. H-195, lot no. E1116; 1:1,000), rabbit anti-CD9 (Abcam, cat. no. ab92726, clone no. EPR2949, lot no. GR260186-21, 1:1,000), rabbit anti-CD63 (Abcam, cat. no. ab134045, clone no. EPR5702, lot no. GR3212162-2; 1:1,000), rabbit anti-CD81 (Abcam, cat. no. ab109201, clone no. EPR4244, lot no. GR181359; 1:1,000), rabbit anti-FAN (Abcam, cat. no. ab81260, lot no. GR32198-5; 1:1,000), rabbit anti-ATG3 (Sigma-Aldrich, cat. no. A3231, lot no. NA; 1:500), rabbit anti-LC3A (Cell Signaling Technology, cat. no. 4599T, clone no. D50G8, lot no. 5; 1:1,000), rabbit anti-LC3B (Cell Signaling Technology, cat. no. 3868T, clone no. D11, lot no. 11; 1:1,000), rabbit anti-LC3C (Cell Signaling Technology, cat. no. 14736T, lot no. 1; 1:1,000), rabbit anti-GABARAP (Cell Signaling Technology, cat. no. 13733T, clone no. E1J4E, lot no. 3; 1:1,000), rabbit anti-GABARAPL1 (Cell Signaling Technology, cat. no. 26632T, clone no. D5R9Y, lot no. 1; 1:1,000), rabbit anti-GABARAPL2 (Cell Signaling Technology, 14256T, clone no. D1W9T, lot no. 3; 1:1,000), rabbit anti-LARP1 (Cell Signaling Technology, cat. no. 14763S, lot no. 1; 1:500), mouse anti-G3BP1 (BD Biosciences, cat. no. 611126, clone no. 23/G3BP, lot no. 39834, 1:500), mouse anti-SF3A1 (Abcam, cat. no. ab139271, clone no. OTI2C4, lot no. GR128640-10, 1:500), peroxidase-AffiniPure donkey anti-rabbit IgG (H+L) (Jackson, cat. no. 711-035-152, lot no. 143451; 1:5,000), peroxidase-AffiniPure donkey anti-guinea pig IgG (H+L) (Jackson, cat. no. 706-035-148, lot no. 108535; 1:5,000), peroxidase-AffiniPure donkey anti-goat IgG (H+L) (Jackson, cat. no. 705-035-147, lot no. 125729; 1:5,000), peroxidase-AffiniPure donkey anti-mouse IgG (H+L) (Jackson, cat. no. 715-035-150, lot no. 142341;1:5,000).

EV immuno-isolation: mouse anti-CD9 (Millipore, cat. no. CBL162, clone no. MM2-57, lot no. 2691299), mouse anti-CD63 (Abcam, cat. no. ab8219, clone no. MEM-259, lot no. GR3196070-12), mouse anti-CD81 (BD Biosciences, cat. no. 555675, lot no. 7096566).

Immunofluorescence: rabbit anti-LC3B (1:500, MBL, cat. no. PM036, lot no. 031), mouse anti-CD63 (1:200, Abcam, cat. no. ab8219, clone no. MEM-259, lot no. GR3196070-12), mouse anti-LC3 (1:200, Nanotools, cat. no. 0231-100/LC3-5F10, clone no. 5F10, lot no. 0231S), rabbit anti-CD9 (1:200, Abcam, cat. no. ab92726, clone no. EPR2949, lot no. GR260186-21), rabbit anti-LC3B (1:200, Cell Signaling Technology, cat. no. 3868T, clone no. D11, lot no. 11), AlexaFluor goat anti-rabbit 488 (1:500, Thermo Fisher, cat. no. A-11034, lot no. 52700A), goat anti-mouse 647 (1:500, Thermo Fisher, cat. no. A21235, lot no. 490187).

Immunoblotting. To generate WCL, cells were lysed in NP40 buffer (25 mM Tris, pH 8.0, 150 mM NaCl, 1% NP40, 5% glycerol) plus protease inhibitor cocktail (Sigma-Aldrich), 2 mM EDTA, 2 mM EGTA, 10 mM β-glycerophosphate, 2.5 mM sodium pyrophosphate, 10 mM NaF, 1 mM Na_3VO_4. For EV lysate and re-solubilization of precipitated material for immunoblotting, samples were resuspended in urea buffer (50 mM Tris-HCl, pH 8.0, 8 M urea, 2% SDS, 10 mM sodium fluoride, 5 mM EDTA) plus protease inhibitor cocktail. Lysates were cleared by centrifugation, quantified by BCA assay (Thermo Fisher, 23225), mixed with sample buffer, resolved by SDS–polyacrylamide gel electrophoresis (PAGE) and transferred to polyvinylidene fluoride membrane. Membranes were blocked for 1 h in 5% milk in PBS with 0.1% Tween 20, incubated in primary antibody overnight at 4 °C, washed, incubated for 1 h at room temperature with HRP-conjugated secondary antibodies (1:5,000; Jackson), washed and visualized via enhanced chemiluminescence (Thermo Fisher) on film. Immunoblots were quantified by densitometry using Fiji.

Immunoprecipitation. For immunoprecipitation of endogenous SAFB and HNRNPK, cells transiently transfected with myc-tagged BirA*, LC3B were lysed 24 h post-transfection in NP40 buffer (25 mM Tris, pH 8.0, 150 mM NaCl, 1% NP40, 5% glycerol) plus protease inhibitor cocktail (Sigma-Aldrich), 2 mM EDTA, 2 mM EGTA, 10 mM β-glycerophosphate, 2.5 mM sodium pyrophosphate, 10 mM NaF, 1 mM Na_3VO_4. Lysates were pre-cleared with protein A/G beads (Santa Cruz, sc-2003) and normal mouse IgG (Santa Cruz, sc-2025) at 4 °C and incubated overnight with mouse anti-myc antibody (Sigma, M5546; 1 µg per 200 µg lysate) at 4 °C. Immune complexes were captured by incubation with protein A/G beads for 4 h at 4 °C and then washed five times with NP40 buffer plus inhibitors, eluted with sample buffer and analysed by immunoblotting. For immunoprecipitation of epitope-tagged prey, cells transiently transfected with myc-tagged BirA*, LC3B (or individual LC3 family members) and FLAG–SAFB, FLAG–G3BP1, FLAG–LARP1, FLAG–SF3A1, FLAG–FAN or mutants thereof were lysed 24 h post-transfection and captured using methods identical to those employed for endogenous protein immunoprecipitations.

Immuno-isolation of EVs. The following antibodies were employed for immune-isolation of EVs: mouse anti-CD9 (Millipore, CBL162), mouse anti-CD63 (Abcam, ab8219), mouse anti-CD81 (BD, 555675). Briefly, EVs purified from approximately 4.5×10^8 cells by differential centrifugation were resuspended in 100 µl of PBS, split equally between four Eppendorf tubes (25 µl each), and resuspended in 500 µl PBS. Each sample was mixed with 2 µg of normal mouse IgG and 50 µl of MACs microbeads (Miltenyi Biotec) for 1 h and then pre-cleared through a MACs magnetic µ Column (Miltenyi Biotec). Flow-through from each of the samples was collected, mixed with 2 µg of antibody against 1 of 3 different EV-associated tetraspanins or normal mouse IgG, 50 µl of MACs microbeads (Miltenyi Biotec) and left to capture overnight at 4 °C. The following day, bound EVs were captured separately on MACs magnetic µ Columns, washed with 1,500 µl PBS and then eluted with 100 µl of hot 2× sample buffer. Samples were then resolved via SDS–PAGE and immunoblotted for LC3 and EV marker proteins.

Immunofluorescence and fluorescence microscopy. For immunofluorescence of myc–BirA* and myc–BirA*–LC3, cells stably expressing GFP–LC3 and myc–BirA* probes were seeded on coverslips coated with 10 µg ml^{-1} fibronectin (BD Biosciences, 356008) diluted in PBS. The next day, cells were briefly washed with PBS, fixed with 4% paraformaldehyde (PFA) for 20 min at room temperature, quenched with PBS/glycine and permeabilized with 0.2% Triton X-100 in PBS. Cells were blocked for 1 h in blocking buffer (5% goat serum in PBS), incubated with mouse anti-myc antibody (1:1,000) overnight at 4 °C, washed, incubated with Alexa Fluor 594 goat anti mouse-secondary antibodies (1:500; Life Technologies) for 1 h at

room temperature, washed and mounted using Prolong Gold Anti-Fade mounting medium (Thermo Fisher, P36934). For immunofluorescence of endogenous LC3, cells stably expressing myc–BirA* probes were processed as above with the exception that rabbit anti-LC3 antibody (1:500, MBL PM036) and Alexa Fluor 488 goat anti rabbit-secondary antibody (1:500; Life Technologies) were incorporated into the primary and secondary staining steps, respectively. Confocal imaging was performed using a TI-inverted microscope stand (Nikon) equipped with a Borealis-modified Yokogawa CSU-X1 confocal head (Spectral Applied Research), solid-state 488-nm (for GFP) and 561-nm (for Alexa Fluor 594) lasers, and a Clara cooled scientific-grade interline CCD (charge-coupled device) camera (Andor) or a CoolSNAP MYO cooled scientific-grade CCD camera (Photometrics). Intracellular fluorescent-tagged protein and immunofluorescence images were acquired at 37 °C using a 100× (NA, 1.49; oil) objective (CFI Aprochromat; Nikon). Microscope hardware was controlled with Nikon Elements Advanced (version 4.5.1) and the images were prepared in Fiji and Adobe Photoshop.

For immunofluorescence detection of endogenous LC3, CD63, SAFB and HNRNPK in enlarged Rab5-positive endosomes, cells of the indicated genotypes were transiently transfected with mCherry–Rab5CA(Q79L) at 70% confluency with Lipofectamine 2000 (Thermo Fisher, 11668027) according to the manufacturer's instructions; in RNA interference experiments, cells were first transfected with siRNA SMARTpools and 24 h later mCherry–Rab5^{Q79L} was transfected using Lipofectamine 2000 (Thermo Fisher, 11668027). After 6 h, DNA-transfected cells were plated onto coverslips coated with fibronectin. Cells were incubated on coverslips for 72 h and then fixed with 4% PFA in PBS for 15 min at room temperature, permeabilized with ice-cold methanol and incubated at −20 °C for 5 min before quenching with PBS/glycine. Cells were blocked in blocking buffer (PBS + 0.1% Tween + 10% goat serum) for 1 h at room temperature, incubated with rabbit anti-LC3B (1:200, MBL PM036), mouse anti-CD63 (1:200, Abcam ab8219) or mouse anti-LC3 (1:200, Axxora 5F10) and rabbit anti-SAFB (1:200, Abcam ab187650) or rabbit anti-LC3B (1:200, CST 3868) and mouse anti-HNRNPK (1:200, Abcam ab39975) antibodies diluted in blocking buffer overnight at 4 °C, washed with PBS, and then incubated with AlexaFluor goat anti-rabbit 488 (1:500, Thermo Fisher, A-11034) and goat anti-mouse 647 (1:500, Thermo Fisher, A21235) secondary antibodies in blocking buffer for 1 h at room temperature. Coverslips were washed with PBS and mounted using Prolong Gold (Thermo Fisher, P36934). For immunofluorescence of endogenous LC3 and CD63 in the absence of Rab5CA(Q79L) perturbation, cells were processed as above using rabbit anti-LC3B (1:200, CST 3868) and mouse anti-CD63 (1:200, Abcam ab8219) antibodies for primary staining. Cells were visualized using a DeltaVision microscope (Applied Precision) fitted with a 60X, 1.4-NA objective and a CoolSnap HQ camera (Photometrics). Images were acquired using softWoRx software (Applied Precision) and prepared in Fiji and Adobe Photoshop. Costes significance tests for co-occurrence[77] and the Mander's overlap coefficient for LC3 with CD63 were performed by drawing a region of interest around individual cells and then employing the Coloc 2 analysis function within Fiji (PSF: 20, Costes randomizations: 10). Furthermore, the proportion of mCherry–Rab5^{Q79L} endosomal area that overlaps with endogenous LC3 in siRNA-treated cells was quantified using Fiji.

APEX staining and TEM. APEX staining and TEM was performed as previously described[24]. Briefly, cells transfected with APEX–LC3 or APEX–GFP were fixed using room-temperature 2.5% glutaraldehyde (Electron Microscopy Sciences) in buffer (100 mM sodium cacodylate with 2 mM $CaCl_2$, pH 7.4), and then transferred to ice. All subsequent steps until resin infiltration were performed at 4 °C. After 30 min, cells were rinsed 5 × 2 min in cold buffer (100 mM sodium cacodylate with 2 mM $CaCl_2$, pH 7.4), and then incubated for 5 min in buffer containing 20 mM glycine, followed by 5 × 2 min washes in cold buffer. Freshly prepared 1 mg ml^{-1} DAB tetrahydrochloride (Sigma, 32750) dissolved in 0.1 M HCl was combined with 0.03% (v/v) (10 mM) H_2O_2 in chilled buffer, and the solution was added to cells for 2 min. The reaction was terminated by removal of the DAB solution, and cells were rinsed 5 × 2 min with cold buffer. Post-fixation staining was performed with 2% osmium tetroxide (Electron Microscopy Sciences, 19152) for 30 min in chilled buffer. Cells were washed 5 × 2 min in ice-cold distilled water, and then placed in 2% aqueous uranyl acetate (Electron Microscopy Sciences, 22400) at 4 °C overnight. Samples were then incubated in a cold-graded ethanol series (20%, 50%, 70%, 90%, 100%, 100%; 2 min in each), washed once in room-temperature anhydrous ethanol, and infiltrated in Durcupan ACM resin (Electron Microscopy Sciences, 14040) using 1:1 (v/v) anhydrous ethanol and resin for 30 min, then 100% resin 2 × 1 h, and finally into fresh resin and polymerized in a vacuum oven at 60 °C for 48 h.

For TEM, DAB-stained areas of resin-embedded cultured cells were identified by bright-field microscopy. Areas of interest were sawed out using a jeweller's saw and mounted onto dummy blocks using cyanoacrylic glue, with the glass coverslip opposite the dummy block. The coverslip was carefully removed, the block was trimmed, and ultrathin (80 nm thick) sections were cut using an ultramicrotome (Leica Ultracut UTC6). Electron micrographs were recorded using a JEOL 1200 TEM operating at 80 keV.

In vivo EV isolation from mice. All experimental procedures and treatments were conducted in compliance with UCSF Institutional Animal Care and Use Committee (IACUC) guidelines under an approved animal protocol (no. AN170608). Compound transgenic C57bl/6 male and female mice harbouring floxed alleles of *Atg12* (*Atg12$^{f/f}$*) or Atg5 (*Atg5$^{f/f}$*) and Cre-recombinase under the ubiquitous CAG promoter (Cag-Cre^{ER}) were generated by cross-breeding of *Atg12$^{f/f}$* or *Atg5$^{f/f}$* mice[15] and CagCre^{ER} mice[78]. Offspring were genotyped with the following PCR primers: *Atg12* WT and f/f: 5′-atgtgaatcagtcctttgccc-3′, 5′-actctgaaggcgttcacggc-3′, 5′-ctctgaaggcgttcacaaca-3′; *Atg5* WT and f/f: 5′-gaatatgaaggcacacccctgaaatg-3′, 5′-acaacgtcgagcacagctgcgcaagg-3′, 5′-gtactgcataatggtttaactcttgc-3′; Cag-Cre^{ER}: 5′- gcctgcattaccggtcgatgc-3′, 5′-cagggtgttataagcaatccc-3′.

Primary astrocyte cultures were prepared as previously described[79]. Briefly, cerebral cortices were collected from P3–4 *Atg5$^{f/f}$* and Cag-Cre^{ER};*Atg5$^{f/f}$* pups (eight male and eight female across conditions). The meninges were removed and the cerebral cortices were dissected into smaller pieces with forceps and then triturated in DMEM, 20% FBS, penicillin/streptomycin and 20 ng ml^{-1} of GM-CSF (PeproTech). The cells were grown in poly-L-lysine-coated flasks. The medium was replenished 3 d after the initial collection. Microglia were removed from the astrocyte layer 6–10 d later by shaking flasks at 200 r.p.m. for 1–2 h at 37 °C. The remaining primary astrocytes were trypsinized and expanded in DMEM, 20% FBS, penicillin/streptomycin and 20 ng ml^{-1} of GM-CSF (PeproTech) for 11 d. Finally, astrocyte cultures were treated with medium containing 2 μM 4-hydroxytamoxifen (4-OHT) for 3 d, washed with PBS and replenished with Neurobasal medium supplemented with N2, L-glutamine and penicillin/streptomycin. After 5 d, the CM from primary astrocyte cultures was collected for EV purification by differential centrifugation (see the section on EV preparation above) and cells were lysed to assess genetic deletion.

For plasma and kidney analysis, 6-week-old Cag-Cre^{ER};*Atg12$^{f/f}$* animals or controls received either tamoxifen (0.2 mg per gram of mouse) or vehicle (peanut oil) via oral gavage for five consecutive days (eight male and eight female across conditions). At 10 weeks after the first tamoxifen treatment, tissues were collected. Kidney was homogenized and lysed before immunoblotting. Whole blood was collected in heparin-coated tubes (Sarstedt, CB 300 LH), centrifuged at 2,000*g* for 5 min at room temperature and the plasma phase was collected. For purification of plasma EVs, approximately 1 ml of platelet-free murine plasma (pooled from four mice per cohort) was diluted in 10 ml of PBS and clarified through a 0.22-μm filter. Subsequently, filtered samples were ultracentrifuged at 100,000*g* for 2 h at 4 °C and purified EV pellets were resuspended in lysis buffer for analysis.

Cell viability assays. To quantify EV-independent release of lactate dehydrogenase, cells were seeded in 6-well culture plates and serum starved for 24 h; cells treated with 100 μM etoposide for 24 h served as a positive control for cell death. After 24 h, CM was collected and EVs were pelleted via differential centrifugation. The supernatant from these samples was then collected and soluble proteins were precipitated by adding TCA to a final concentration of 20% and incubating on ice for 1 h. Subsequently, precipitated protein was pelleted by ultracentrifugation at 200,000*g* for 1 h. Pellets were washed with 5 ml of ice-cold acetone, re-centrifuged at 200,000*g* for 1 h and air-dried. Urea lysis buffer was added to re-solubilize the pellets and the levels of lactate dehydrogenase were quantified by western blot.

To quantify viability following serum starvation, cells were seeded on coverslips coated with fibronectin and subjected to serum starvation or control medium with full serum for 24 h. Cells were then stained for viability using Calcein AM and ethidium homodimer-1 (Thermo Fisher, MP 03224) according to the manufacturer's instructions, visualized on an Axiovert 200 epifluorescent microscope, and dead cells (ethidium-positive, Calcein-negative) were enumerated.

CRISPR–Cas9 gene deletion. HEK293T knockout cell lines were generated by transient transfection of pSpCas9(BB)-2A-Puro (Addgene no. 48139) encoding U6-driven expression of sgRNAs (Scramble guide: GCACTACCAGAGCTAACTCA; *ATG7* guide: ACACACTCGAGTCTTTCAAG; *ATG12* guide: CCGTCTTCCGCTGCAGTTTC; *ATG14* guide: CTACTTCGACGGCCGCGACC; *FIP200* guide: AGAGTGTGTACCTACAGTGC). Cells were selected 48–72 h post-transfection with 1 μg ml^{-1} puromycin for 48 h. Polyclonal populations were collected for Surveyor analysis (IDT, 706020) and were sorted into single-cell populations by limiting dilution at 1.5 cells per well per 96-well plate. For DNA analysis, genomic DNA samples were prepared using QuickExtract (Epicentre). The PCR products were column purified and analysed with the Surveyor Mutation Detection Kit (IDT). For genotyping of single-sorted cells, PCR-amplified products encompassing the edited region (*ATG7* Fwd: TGGGGGACAGTAGAACAGCA, *ATG7* Rev: CCTGGATGTCCTCTCCCTGA; *ATG12* Fwd: AGCCGGGAACACCAAGTTT, *ATG12* Rev: GTGGCAGCCAAGTATCAGGC; *ATG14* Fwd: AAAATCCCACGTGACTGGCT, *ATG14* Rev: AATGGCAGCAACGGGAAAAC; *FIP200* Fwd: ATTCTCTGGCTTGACAGGACAG, *FIP200* Rev: AAATACTGAGCGTGCACATTGC) were cloned into the pCR4-TOPO TA vector using the TOPO-TA cloning kit (Thermo Fisher no. 450030) and sequence verified. Sequencing is available on request.

RNA interference. For transient siRNA-mediated knockdown, cells were first transfected with siRNA and using DharmaFECT no. 1 (Dharmacon T-2001-03)

according to the manufacturer's instructions, and after 24 h were transfected with a plasmid encoding mCherry–Rab5^{Q79L}. ON-TARGETplus smart pools against *ATG7* (10533; L-020112-00-0005), *PDCD6IP* (also known as ALIX) (10015; L-004233-00-0005), *TSG101* (7251; L-003549-00-0005), *CHMP3* (51652; L-004696-00-0005), *VPS4a* (27183; L-013092-00-0005), *VPS4b* (9525; L-013119-00-0005), *CHMP4b* (128866; L-018075-01-0005), SMPD3 (also known as nSMase2) (55512, L-006678-00-0005), NSMAF (also known as FAN) (8439; L-017920-00-0005) and non-targeting siRNA (D-001810-01-20) were purchased from Dharmacon. To generate stable knockdowns, cells were transduced with pLKO.1 lentiviral vectors (Sigma-Aldrich) expressing shRNAs targeting *ATG7* (TRCN0000007584), *ATG3* (no. 1, TRCN0000148120; no. 2, TRCN0000146846; no. 3, TRCN0000147381), *SMPD3* (nSMase2) (no. 1, TRCN0000048944; no. 2, TRCN0000048945), *NSMAF* (FAN) (no. 1, TRCN0000145430; no. 2, TRCN0000143925) and non-targeting shRNA (SHC002).

Quantitative PCR. For quantitative PCR analysis, total RNA from cells was isolated using QIAzol lysis reagent (Qiagen). RNA was reverse transcribed using MMLV reverse transcriptase (Roche) and the resulting cDNA was analysed via real-time quantitative PCR using QuantiTect SYBR Green PCR Master Mix and gene-specific primers (*GAPDH* Fwd: TGTCAAGCTCATTTCCTGGTATG, *GAPDH* Rev: CTCTCTTCCTCTTGTGCTCTTG; *SMPD3* (nSMase2) Fwd: CAACAAGTGTAACGACGATGCC, *SMPD3* (nSMase2) Rev: CGATTCTTTGGTCCTGAGGTGT) according to the manufacturer's instructions. Ct values for intracellular transcripts were converted to fold expression changes ($2-\Delta\Delta$Ct values) following normalization to intracellular *GAPDH*. Quantitative real-time PCR was performed using an Applied Biosystems StepOneplus Real-Time PCR System (Thermo Fisher).

Statistics and reproducibility. Statistical analyses were performed using Prism GraphPad 5 software. Groups were compared using unpaired or paired Student's *t*-test where indicated for pairwise comparisons or one-way ANOVA followed by Tukey's post-hoc test for multiple comparisons. The sample size was chosen on the basis of the size of the effect and variance for the different experimental approaches. Details regarding the statistical analysis of the proteomic data and the bioinformatics analysis of the BirA*–LC3-labelled secretome (both class I and class II datasets), the ATG7- and ATG12-dependent EV proteome and the RNA profiles are provided in the corresponding figure legends and/or the Methods sections above. *P* values of less than 0.05 are considered to be significant.

Reporting Summary. Further information on research design is available in the Nature Research Reporting Summary linked to this article.

Data availability

The MS proteomics data associated with this study have been deposited to the ProteomeXchange Consortium via the PRIDE[80] partner repository with the dataset identifier PXD015479. RNA-seq data have been deposited in GEO: GSE137618. Furthermore, the data and/or reagents that support the findings of this study are available from the corresponding author, J.D., upon reasonable request. Source data for Figs. 1–7 and Extended Data Figs. 1–7 are provided online.

References

68. Pear, W. S., Scott, M. L. & Nolan, G. P. Generation of high-titer, helper-free retroviruses by transient transfection. *Methods Mol. Med.* **7**, 41–57 (1997).
69. Cox, J. & Mann, M. MaxQuant enables high peptide identification rates, individualized p.p.b.-range mass accuracies and proteome-wide protein quantification. *Nat. Biotechnol.* **26**, 1367–1372 (2008).
70. Tyanova, S. et al. The Perseus computational platform for comprehensive analysis of (prote)omics data. *Nat. Methods* **13**, 731–740 (2016).
71. Kuksa, P. P. et al. DASHR 2.0: integrated database of human small non-coding RNA genes and mature products. *Bioinformatics* **35**, 1033–1039 (2019).
72. Mi, H., Muruganujan, A., Ebert, D., Huang, X. & Thomas, P. D. PANTHER version 14: more genomes, a new PANTHER GO-slim and improvements in enrichment analysis tools. *Nucleic Acids Res.* **47**, D419–D426 (2019).
73. Szklarczyk, D. et al. STRINGv11: protein–protein association networks with increased coverage, supporting functional discovery in genome-wide experimental datasets. *Nucleic Acids Res.* **47**, D607–D613 (2019).
74. Kuleshov, M. V. et al. Enrichr: a comprehensive gene set enrichment analysis web server 2016 update. *Nucleic Acids Res.* **44**, W90–W97 (2016).
75. Hulsen, T., de Vlieg, J. & Alkema, W. BioVenn - a web application for the comparison and visualization of biological lists using area-proportional Venn diagrams. *BMC Genomics* **9**, 488 (2008).
76. Zhou, Y. et al. Metascape provides a biologist-oriented resource for the analysis of systems-level datasets. *Nat. Commun.* **10**, 1523 (2019).
77. Costes, S. V. et al. Automatic and quantitative measurement of protein–protein colocalization in live cells. *Biophys. J.* **86**, 3993–4003 (2004).
78. Hayashi, S. & McMahon, A. P. Efficient recombination in diverse tissues by a tamoxifen-inducible form of Cre: a tool for temporally regulated gene activation/inactivation in the mouse. *Dev. Biol.* **244**, 305–318 (2002).
79. Albuquerque, C., Joseph, D. J., Choudhury, P. & MacDermott, A. B. Dissection, plating, and maintenance of cortical astrocyte cultures. *Cold Spring Harb. Protoc.* https://doi.org/10.1101/pdb.prot5273 (2009).
80. Vizcaino, J. A. et al. 2016 update of the PRIDE database and its related tools. *Nucleic Acids Res.* **44**, 11033 (2016).

Acknowledgements

We thank M. Krummel (UCSF) for generously providing reagents, members of the Debnath laboratory for helpful discussions and R. Perera (UCSF) for critical reading of the manuscript. We also thank S. Kilinc and A. Goga (UCSF) for assistance with EV concentration and size analysis, and A. Navickas for advice on RNA-seq library preparation. Grant support includes the NIH (CA201849, CA126792, CA201849 and CA213775 to J.D.; R00CA194077 and R01CA240984 to H.G.; K08CA184116 to A.P.W.; and AG057462 to J.D. and E.J.H.), the DOD BCRP (W81XWH-11-1-0130 to J.D.), the Samuel Waxman Cancer Research Foundation (to J.D.), a UCSF QB3 Calico Longevity Fellowship (to J.D. and A.M.L.) and a Dale Frey Breakthrough Award from the Damon Runyon Cancer Research Foundation (DFS 14-15 to A.P.W.). Fellowship support includes a Banting Postdoctoral Fellowship from the Government of Canada (201409BPF-335868) and a Cancer Research Society Scholarship for Next Generation of Scientists to A.M.L., NSF Graduate Student Fellowships (1650113 to T.S. and 1144247 to J.G.), a Canadian Institutes of Health Research Post-doctoral Fellowship to F.K., NRSA awards from the NCI (F31CA217015 to T. Marsh, F30CA224693 to J.Y.L.), a UCSF IRACDA Postdoctoral Fellowship (K12GM081266) to T. Monkkonen and an NCI T32 training grant (T32CA108462) to A.V.

Author contributions

J.D. and A.M.L. conceived the study and designed the experiments. A.M.L., H.H.H., A.P.W. and J.D. designed and optimized the quantitative proteomics workflows. A.M.L., J.D. and H.G. designed, performed and analysed the extracellular and intracellular RNA-seq experiments. A.M.L., T.S., J.Y., F.K., J.Y.L., T. Monkkonen and A.V. performed biochemical and cell biological experiments. H.H.H. and A.P.W. performed MS and analysed the resulting liquid chromatography (LC)–MS/MS data with A.M.L. A.M.L. and J.G. performed bioinformatics analysis of the BirA*–LC3-labelled secretome. A.M.L., T. Marsh, Y.-H.H. and E.J.H. performed mouse experiments and primary astrocyte isolation. D.Z. and L.Y. performed APEX staining and TEM. A.M.L. and J.D. analysed the biochemical and cell biological data. A.M.L. and J.D. wrote the paper, with input from all other authors.

Competing interests

J.D. is a Scientific Advisory Board Member for Vescor Therapeutics, LLC.

Additional information

Extended data is available for this paper at https://doi.org/10.1038/s41556-019-0450-y.

Supplementary information is available for this paper at https://doi.org/10.1038/s41556-019-0450-y.

Correspondence and requests for materials should be addressed to J.D.

Reprints and permissions information is available at www.nature.com/reprints.

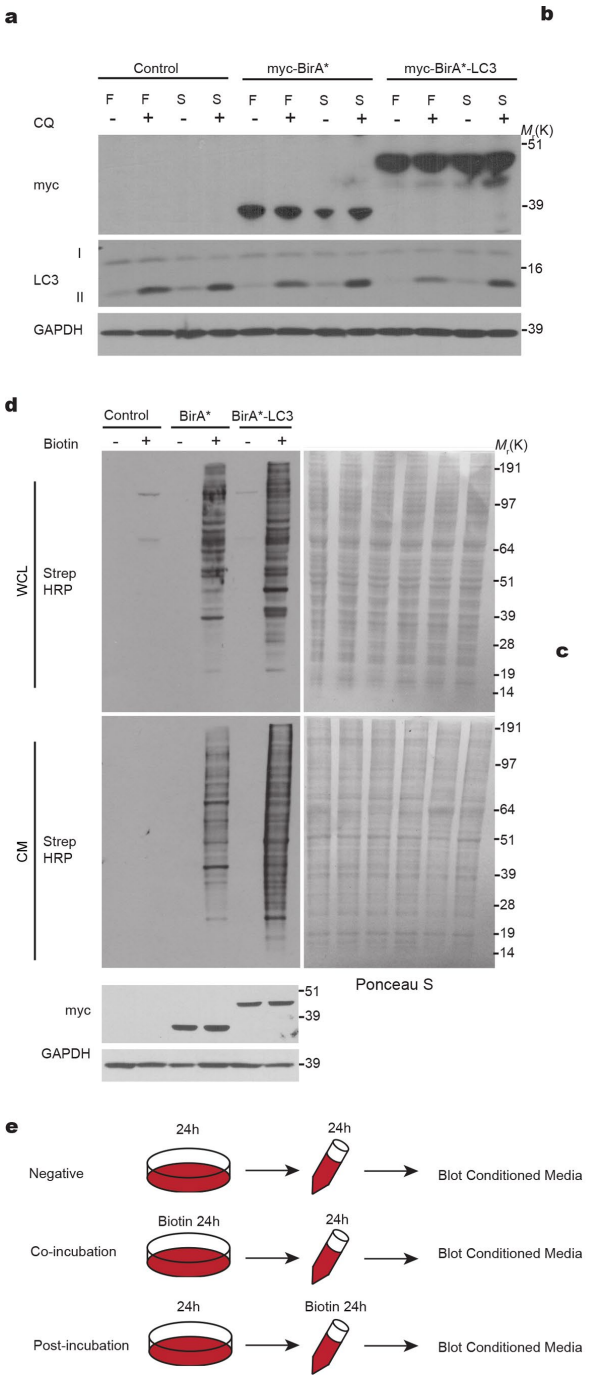

Extended Data Fig. 1 | See next page for caption.

Extended Data Fig. 1 | Functional validation of the BirA*-LC3 recombinant probe. a, Cells stably expressing myc-BirA*-LC3, myc-BirA* or vector control were incubated in either full (F) or serum free media (S) for 4h in the absence or presence of 50 μM chloroquine (CQ) for the last 1h. Cells were lysed and subject to immunoblotting for indicated proteins (n=2 biologically independent experiments). **b**, Representative images of cells stably expressing GFP-LC3 and myc-BirA*-LC3 or myc-BirA* and immunostained with anti-myc antibody (n=3 biologically independent samples). **c**, Representative images of cells stably expressing myc-BirA*-LC3 or myc-BirA* and co-immunostained with anti-LC3 (green) and anti-myc (magenta) antibody (n=3 biologically independent samples). **d**, Biotinylation blots reproduced from Fig. 1b with accompanying Ponceau S stained membranes of whole cell lysate (WCL) and conditioned media (CM) (n=3 biologically independent experiments). **e**, Schematic of experiment to test for intracellular versus extracellular origin of BirA* and BirA*-LC3-mediated biotinylated targets isolated from CM. **f**, Representative Strep-HRP blot for biotinylated proteins in the precipitated CM from myc-BirA*-LC3 or myc-BirA* cells co-incubated (Co) or post-incubated (Post) with 50 μM biotin for 24h and negative control (Neg). CM was probed to validate expression and secretion of the myc-tagged recombinant proteins (n=2 biologically independent experiments). Unprocessed blots available in Source Data Extended Data Fig. 1.

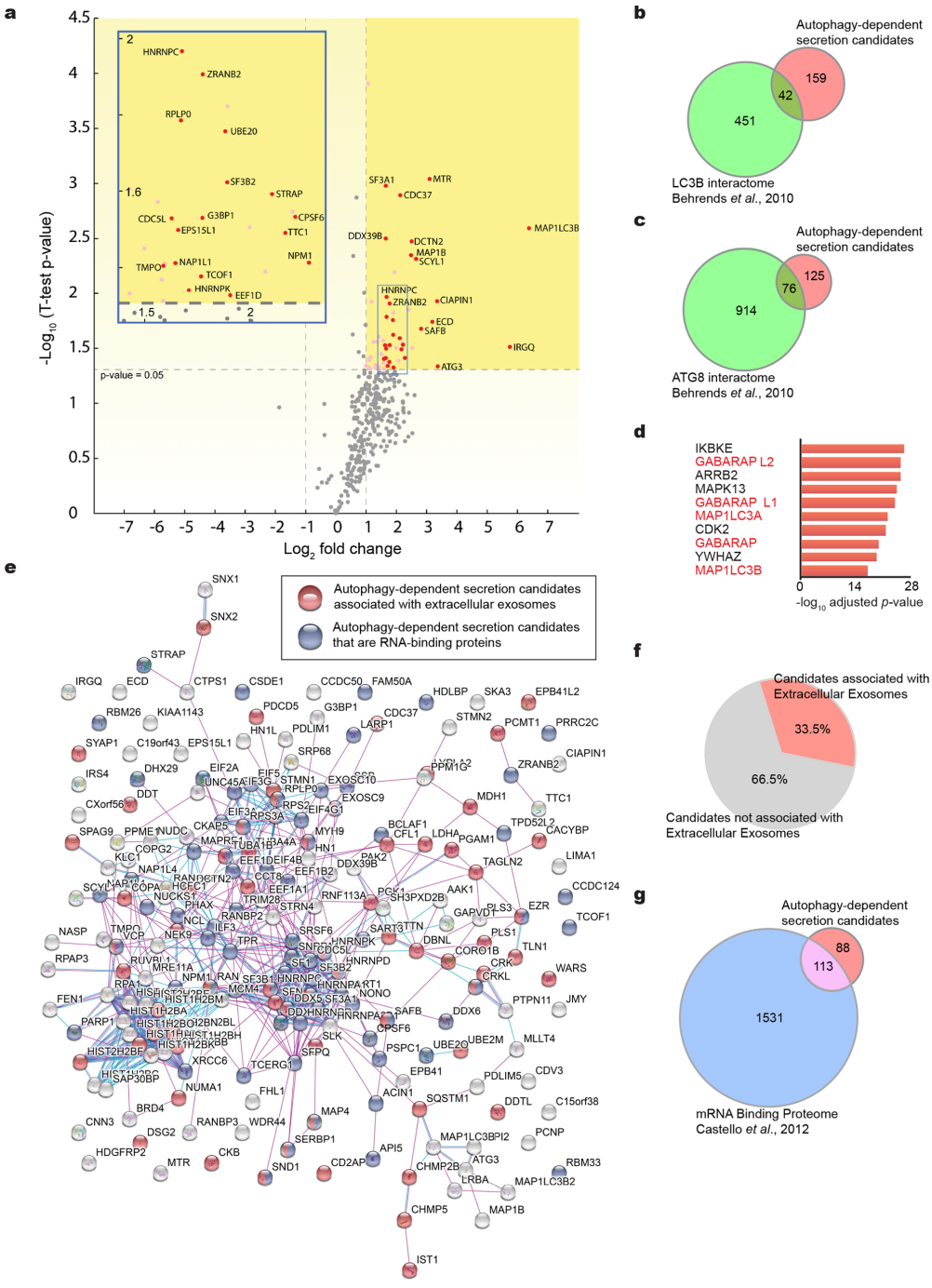

Extended Data Fig. 2 | See next page for caption.

Extended Data Fig. 2 | BirA*-LC3B-labelled secretome is enriched in RBPs. a, Volcano plot of BirAf*-LC3-labeled secretome quantified by mass spectrometry. SILAC labelled biotin-tagged proteins plotted according to -log_{10} p-values as determined by two-tailed t-test and log_2 fold enrichment (BirA*-LC3/BirA*) (n=3 biologically independent samples). Grey horizontal dotted line: significance cut-off with p-value of 0.05. Log_2 fold change reflects LC3-BirA* to BirA* alone ratio. Grey vertical dotted line: 2-fold enriched and de-enriched cut-off. Pink: significantly enriched proteins relative to BirA* alone. Red: Class I enriched proteins represented in heat map in Fig. 1. Inset: Expanded view of significantly enriched proteins. **b**, Venn diagram showing overlap of secretory autophagy candidates (Class I and II hits) with the LC3B intracellular interactome defined in Behrends *et al*. 2010. **c**, Venn diagram showing the overlap of secretory autophagy candidates (Class I and II hits) with the entire ATG8 intracellular interactome defined in Behrends *et al*. 2010. **d**, Ranked list of proteins with greatest connectivity to secretory autophagy candidates as determined by the Enrichr gene enrichment analysis tool (n=3 biologically independent samples; 200 enriched proteins in Class I + II datasets). Statistical significance calculated by one-way Fisher's exact test and adjusted using the Benjamini–Hochberg method. LC3 family members highlighted in red. **e**, Network map of autophagy-dependent secretion candidates. Class I and II secretory autophagy candidates mapped to zero-order protein interaction network using Search Tool for the Retrieval of Interacting Genes/Proteins (STRING) and proteins associated with extracellular exosomes or with RNA-binding functions coloured in red and blue, respectively. **f**, Pie chart plotting percentage of Class I and II secretory autophagy candidates assigned to Gene Ontology (GO) term extracellular exosome by PANTHER. **g**, Venn diagram showing overlap of class I and II secretory autophagy candidates with the mRNA binding proteins from Castello *et al*. 2012. Data available in Source Data Extended Data Fig. 2.

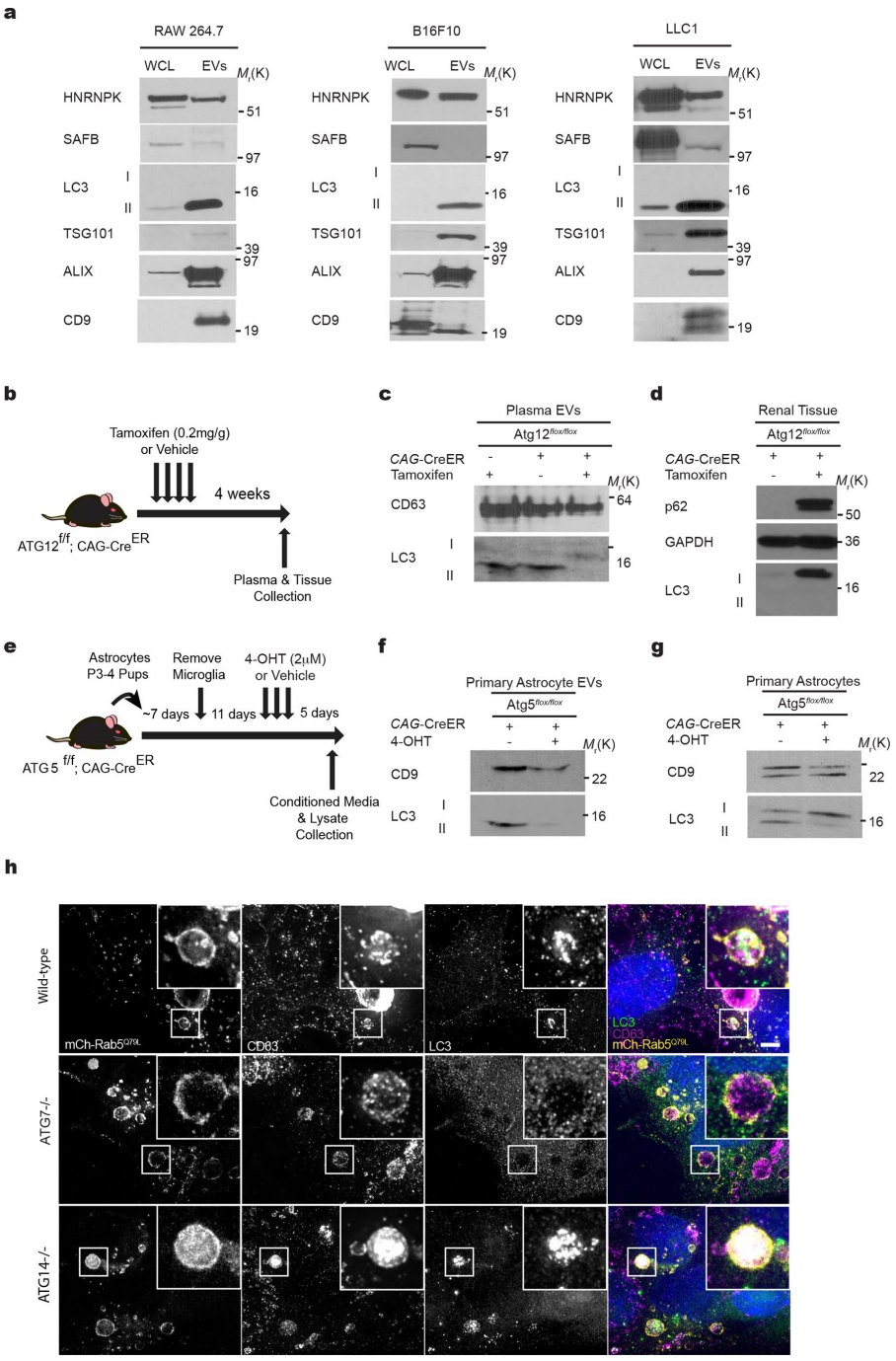

Extended Data Fig. 3 | See next page for caption.

Extended Data Fig. 3 | Endogenous LC3-II is secreted within EVs isolated from cultured cells and murine plasma. a, Whole cell lysate (WCL) and extracellular vesicle lysates (EVs) from murine RAW264.7 macrophages treated with 100 ng/ml LPS for 24h and 20 μM nigericin for 1 h, murine B16F10 melanoma cells, and murine LLC1 cells were immunoblotted for LC3, SAFB, HNRNPK and extracellular vesicle marker proteins (n=2 biologically independent experiments). **b**, Workflow employed to obtain plasma and tissue from *CAG-Cre^{ER};Atg12$^{flox/flox}$* mice in which *Atg12* was systemically deleted via tamoxifen treatment. **c**, Extracellular vesicles (EVs) isolated from the plasma of naïve wild-type mice (*CAG-Cre^{ER}* or *Atg12$^{flox/flox}$*) and mice in which *Atg12* was systemically deleted by 4-OHT treatment (*CAG-Cre^{ER}; Atg12$^{flox/flox}$*) were lysed and immunoblotted for LC3 and the indicated extracellular vesicle marker proteins (n=2 biologically independent experiments). **d**, Whole cell lysates (WCL) derived from the renal tissue of mice in Panel **c** were immunoblotted for LC3 and the indicated marker proteins (n=2 biologically independent experiments). **e**, Workflow employed to obtain CM from murine astrocytes (*CAG-Cre^{ER};Atg5$^{flox/flox}$*) in which *Atg5* was deleted *ex vivo* via 4-OHT treatment. **f**, Extracellular vesicles (EVs) isolated from the conditioned media of naive wild-type (*Atg5$^{flox/flox}$*) primary astrocytes and astrocyte cultures in which *Atg5* was deleted *ex vivo* (*CAG-Cre^{ER}; Atg5$^{flox/flox}$*) by 4-OHT treatment were lysed and immunoblotted for LC3 and CD9 (n=2 biologically independent experiments). **g**, Whole cell lysates (WCL) primary astrocyte cultures in Panel d were immunoblotted for LC3 and CD9 (n=2 biologically independent experiments). **h**, Representative fluorescence micrographs from wild-type, *ATG7-/-* and *ATG14-/-* HEK293T cells transfected with mCherry-Rab5^{Q79L} (yellow). Cells were immunostained for endogenous LC3 (green) and CD63 (magenta) (n=3 biologically independent samples). Scale bar=10μm. Unprocessed blots available in Source Data Extended Data Fig. 3.

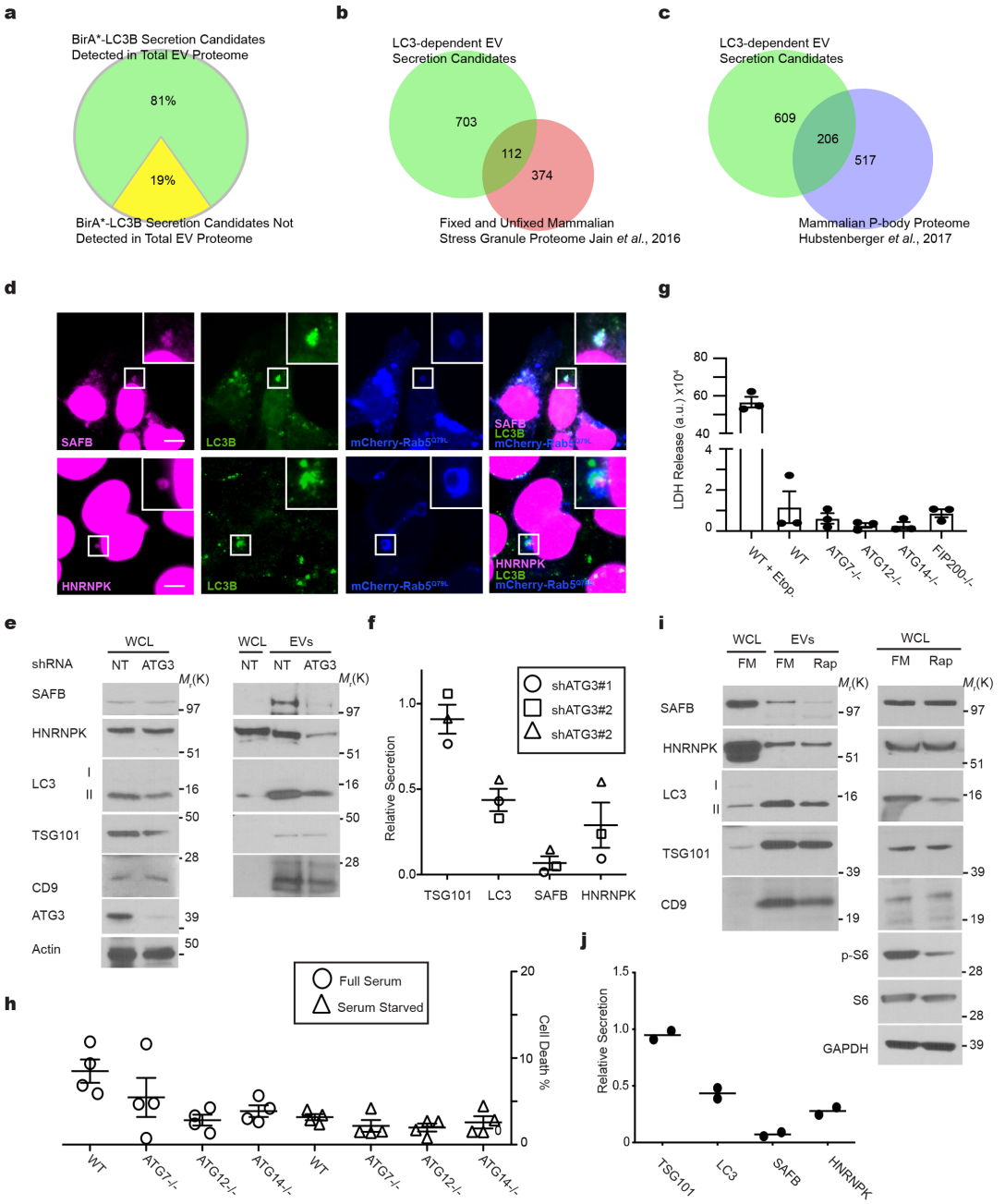

Extended Data Fig. 4 | See next page for caption.

Extended Data Fig. 4 | Components of stress granules and P-bodies secreted in EVs through mechanisms requiring the LC3-conjugation machinery. a, Proportion of BirA*-LC3B- labelled secretome (Class I, II candidates) detected in the total extracellular vesicle (EV) proteome defined by TMT quantitative mass spectrometry. **b**, Venn diagram showing overlap of EV components requiring ATG7 and ATG12 for secretion with the fixed and unfixed stress granule proteome from Jain *et al*., 2016. **c**, Venn diagram showing the overlap of EV components requiring ATG7 and ATG12 for secretion with the P-body proteome from Hubstenberger *et al*., 2017. **d**, Representative fluorescence micrographs from wild-type HEK293T cells transfected with mCherry-Rab5Q79L (blue) and immunostained for endogenous LC3 (green) and SAFB or HNRNPK (magenta) (n=3 biologically independent samples). Scale bar=10μm. **e**, Whole cell (WCL) and EV lysates harvested from equal numbers of cells stably expressing non-targeting (NT) or *ATG3* shRNA were immunoblotted for indicated proteins (n=3 biologically independent samples). **f**, Quantification of indicated protein levels in EVs from cells stably expressing shRNAs targeting *ATG3* relative to non-targeting shRNA (mean ±s.e.m.; n=3 biologically independent samples). **g**, Quantification of Lactate Dehydrogenase (LDH) in EV-depleted conditioned media from wild-type (WT) HEK293T cells treated 100 μM Etoposide (Etop) for 24h or WT and *ATG* knockout cells serum starved for 24h (mean ±s.e.m.; n=3 biologically independent experiments). **h**, Cell death in wild-type (WT) and *ATG* knockout cells (KO) after 24h in full serum media (FM) or serum starved media (SS) quantified using Calcein-AM and ethidium bromide staining (mean ±s.e.m.; n=3 biologically independent experiments). **i**, Whole cell and EV lysates from wild-type cells grown in EV-depleted full serum media (FM) or EV-depleted FM with 100 nM Rapamycin (Rap) for 24h. Immunoblots probed against the indicated proteins (n=2 biologically independent experiments). **j**, Quantification of the relative levels of indicated proteins in EVs from Rap-treated cells in Panel d (line=mean; n=2 biologically independent experiments). Data and unprocessed blots available in Source Data Extended Data Fig. 4.

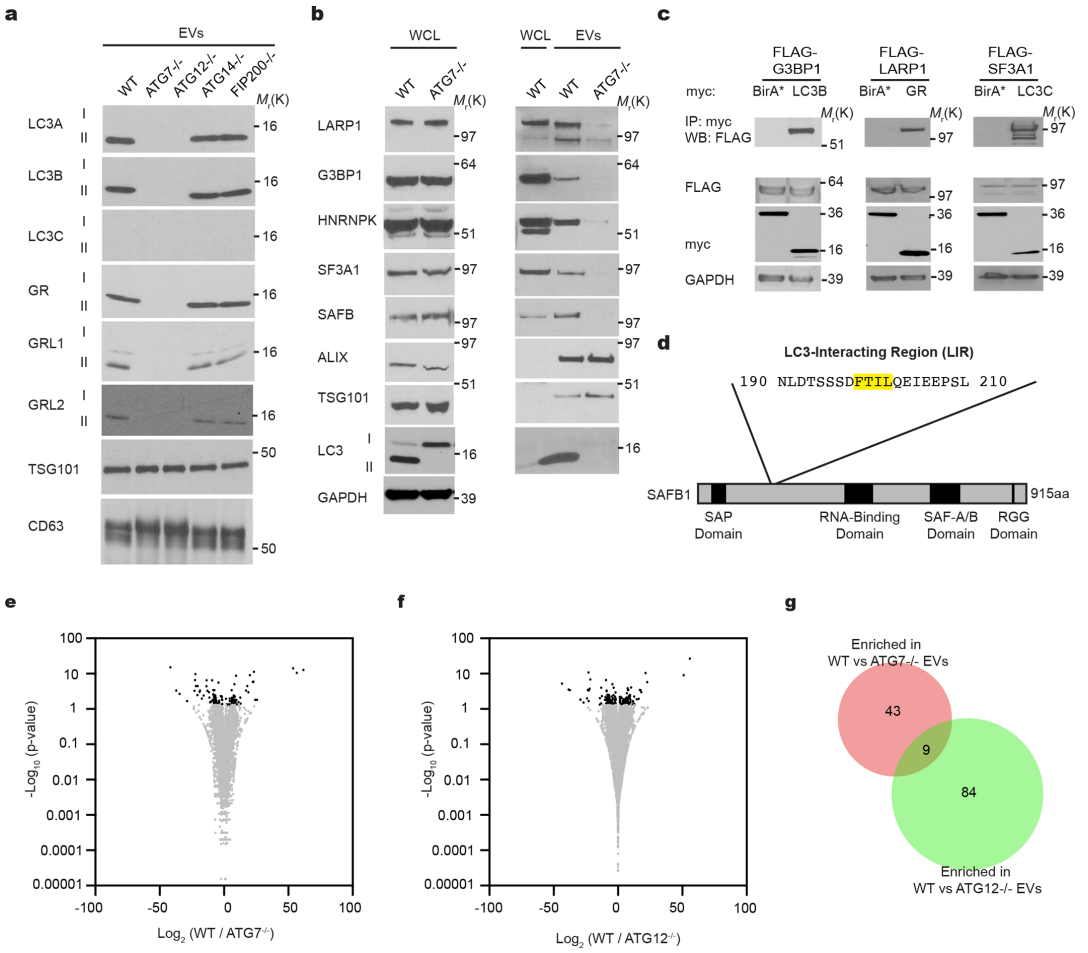

Extended Data Fig. 5 | LC3-conjugation machinery controls EV-mediated secretion of diverse RBPs. a, EVs from WT and ATG deficient cells normalized for protein concentration and immunoblotted to detect endogenous LC3A, LC3B, LC3C, GABARAP (GR), GABARAPL1 (GRL1), GABARAPL2 (GRL2), and indicated marker proteins (n=2 biologically independent experiments). **b**, Whole cell (WCL) and EV lysates from WT and *ATG7-/-* cells were normalized for protein concentration and immunoblotted for indicated proteins (n=3 biologically independent experiments). **c**, HEK293T cells co-transfected with FLAG-tagged G3BP1, LARP1 or SF3A1, and myc-tagged LC3B, GABARAP (GR), LC3C respectively, or myc-BirA* were lysed, immunoprecipitated (IP) with anti-myc antibody and immunoblotted (WB) with indicated antibodies (n=3 biologically independent experiments). **d**, Diagram mapping the domains and primary LC3-interaction region (LIR) in SAFB. **e**, Volcano plot of mRNA and long non-coding RNA (large RNA) detected in EVs from WT and *ATG7-/-* cells. Results plotted according to -log10 p-values as determined by DESeq2 and log2 fold enrichment (n=3 biologically independent samples; WT/*ATG7-/-*). Grey dots: RNAs not enriched in EVs from WT or *ATG7-/-* cells identified with a *p*-value >0.05 and/or log2 fold change between -0.5 and 0.5 (-0.5<log2FC<0.5). Black dots: Large RNAs enriched in EVs from WT cells or *ATG7-/-* cells. **f**, Volcano plot of mRNA and long non-coding RNA (large RNA) detected in EVs from WT and *ATG12-/-* cells. Results plotted according to -log10 p-values as determined by DESeq2 and log2 fold enrichment (n=3 biologically independent samples; WT/*ATG12-/-*). Grey dots: RNAs not enriched in EVs from WT or *ATG12-/-* cells identified with a *p*-value >0.05 and/or log2 fold change between -0.5 and 0.5 (-0.5<log2FC<0.5). Black dots: Large RNAs enriched in EVs from WT or *ATG12-/-* cells. **g**, Venn diagram showing the overlap of mRNA and long non-coding RNAs (large RNAs) enriched in EVs from WT relative to *ATG7-/-* cells and EVs from WT relative to *ATG12-/-* cells. Data and unprocessed blots available in Source Data Extended Data Fig. 5.

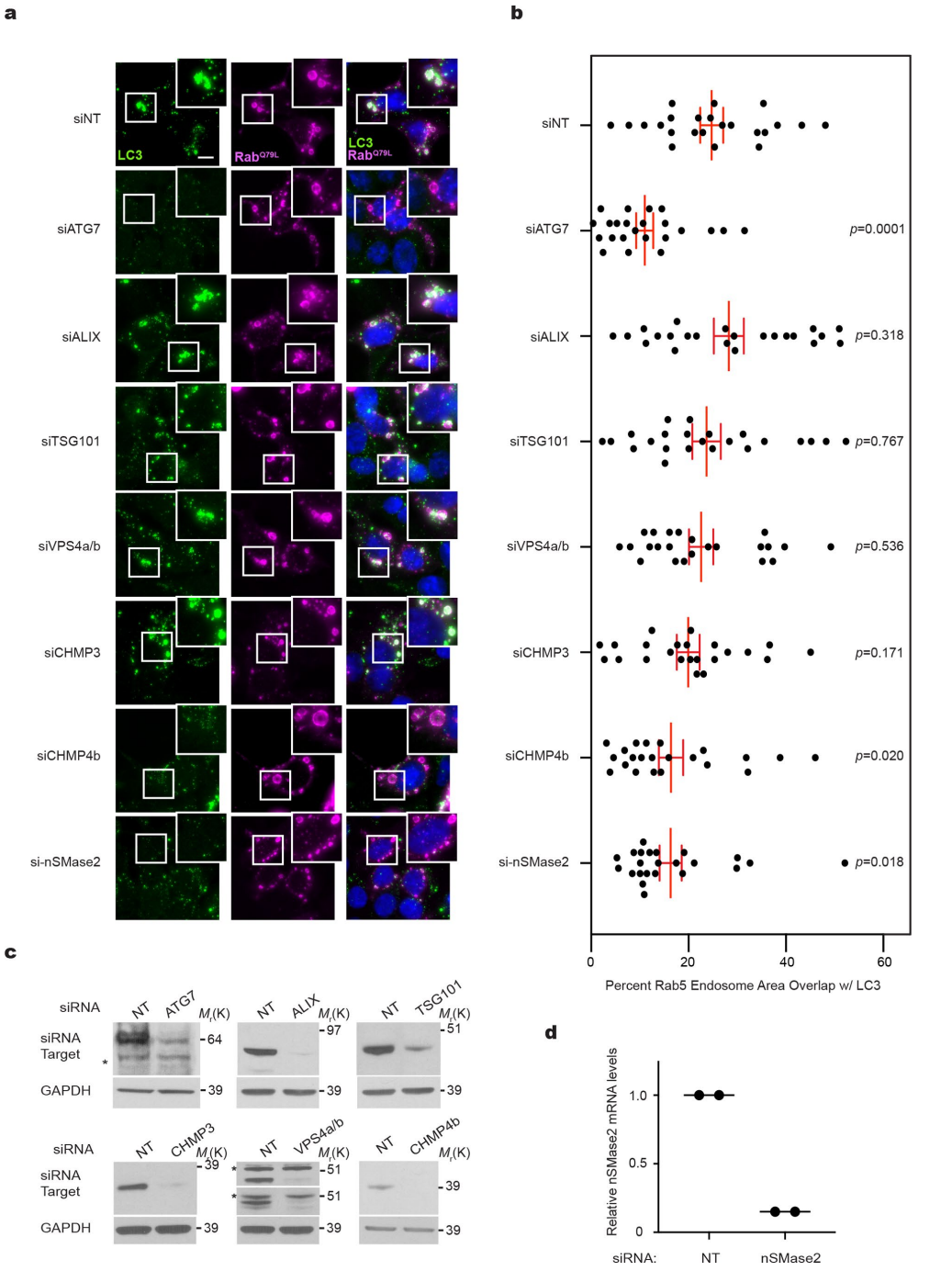

Extended Data Fig. 6 | See next page for caption.

Extended Data Fig. 6 | LC3 delivery into ILVs of Rab5Q79L endosomes requires CHMP4b and nSMase2, but is independent of other ESCRT machinery components. a, Representative fluorescence micrographs from wild-type HEK293T cells co-transfected with mCherry-Rab5Q79L (magenta) and non-targeting (NT) control siRNA or siRNAs that deplete ATG7, ALIX, TSG101, VPS4a/b, CHMP3, CHMP4b and nSMase2. Cells were immunostained for endogenous LC3 (green) (n=2 biologically independent experiments). Scale bar=10μm. **b**, Scatter plot of the proportion of mCherry-Rab5^{Q79L} endosomes that overlap with LC3 in immuno-stained cells in Panel a (mean ± s.e.m.; n=23 biologically independent samples). Statistical significance calculated by one-way ANOVA coupled with Fisher's least significant difference test. **c**, Lysates from cells in Panel a were immunoblotted with antibodies the various siRNA targets and GAPDH as a loading control. Representative blots are shown (n=2 biologically independent experiments). Non-specific bands are indicated with an asterisk (*). **d**, Quantitative PCR (QPCR) measurement of *nSMase2* mRNA in HEK293T cells transfected with siRNAs targeting *nSMase2*, *nSMase2* (nSM2) relative to non-targeting siRNA (NT) control cells (line=mean; n=1, 2 technical replicates). Data and unprocessed blots available in Source Data Extended Data Fig. 6.

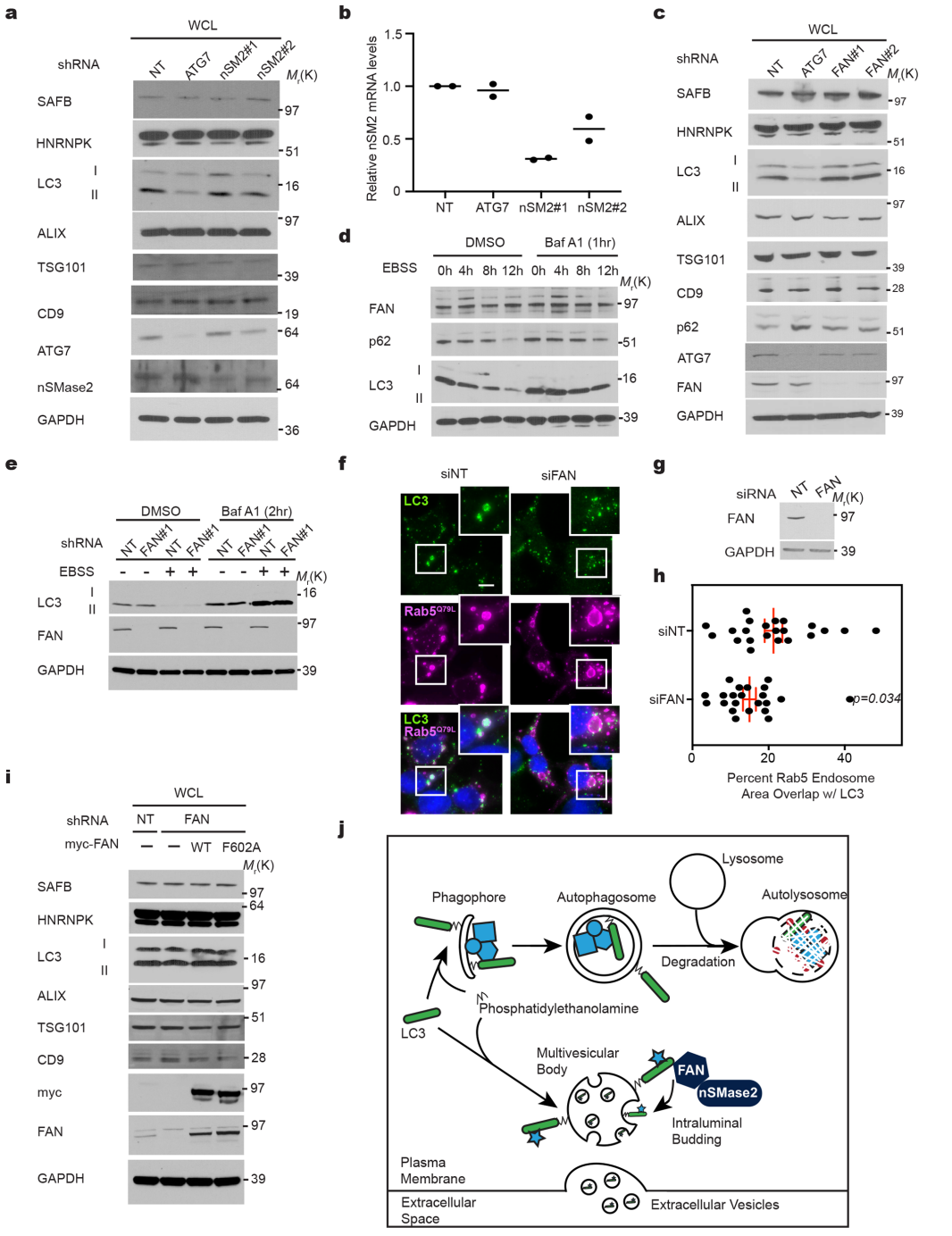

Extended Data Fig. 7 | See next page for caption.

Extended Data Fig. 7 | LC3-dependent EV loading and secretion (LDELS) requires FAN and nSMase2. a, Whole cell lysate harvested from equal numbers of HEK293Ts stably expressing non-targeting (NT) shRNA or shRNAs that deplete ATG7 or nSMase2(nSM2) immunoblotted for indicated proteins (n=2 biologically independent experiments). **b**, Quantitative PCR (QPCR) for *nSMase2* mRNA in HEK293Ts stably expressing shRNAs targeting ATG7, nSMase2 (nSM2) relative to non-targeting shRNA (NT) control cells (line=mean; n=1, 2 technical replicates). **c**, Whole cell lysates from HEK293Ts stably expressing non-targeting shRNA (NT) or shRNAs that deplete ATG7 or FAN were immunoblotted with antibodies for the indicated proteins (n=2 biologically independent experiments). **d**, HEK293Ts were EBSS starved for the indicated times, treated with DMSO or 50nM Bafilomycin A1 (Baf A1) for 1 h prior to lysis, lysed and immunoblotted for FAN and the indicated proteins (n=2 biologically independent experiments). **e**, HEK293Ts expressing non-targeting (NT) shRNA or shRNA that depletes FAN were starved in EBSS for 4h, treated with DMSO or 50nM Bafilomycin A1 (Baf A1) for 1h prior to lysis, lysed and immunoblotted for the indicated proteins (n=2 biologically independent experiments). **f**, Representative fluorescence micrographs from wild-type cells co-transfected with mCherry-Rab5Q79L (magenta) and non-targeting (NT) control siRNA or siRNAs that deplete FAN. Cells were immunostained for endogenous LC3 (green)(n=2 biologically experiments). Scale bar=10μm. **g**, Lysates from cells in Panel f were immunoblotted with antibodies against FAN and GAPDH as a loading control (n=2 biologically independent experiments). **h**, Scatter plot of the proportion of mCherry-Rab5Q79L endosomes overlapping with LC3 in immuno-stained cells in Panel f (mean ±s.e.m.; n=22 biologically independent samples). Statistical significance calculated by unpaired two-tailed t-test. **i**, Whole cell lysate from HEK293Ts analysed in Fig. 7j that were co-expressing non-targeting (NT) shRNA or shRNA that depletes endogenous FAN along with FLAG-tagged wild-type FAN (WT) or mutant FAN (F199A) were immunoblotted for the indicated proteins (n=2 biologically independent experiments). **j**, Proposed model for LC3-dependent EV loading and secretion (LDELS) in comparison to classical autophagy. Data and unprocessed blots available in Source Data Extended Data Fig. 7.

Publishing Agreement

It is the policy of the University to encourage open access and broad distribution of all theses, dissertations, and manuscripts. The Graduate Division will facilitate the distribution of UCSF theses, dissertations, and manuscripts to the UCSF Library for open access and distribution. UCSF will make such theses, dissertations, and manuscripts accessible to the public and will take reasonable steps to preserve these works in perpetuity.

I hereby grant the non-exclusive, perpetual right to The Regents of the University of California to reproduce, publicly display, distribute, preserve, and publish copies of my thesis, dissertation, or manuscript in any form or media, now existing or later derived, including access online for teaching, research, and public service purposes.

DocuSigned by:
Tina Solnik
2C52343C7C3046F...
Author Signature

6/7/2020
Date